

DISSERTATION PROPOSAL:
FREQUENCY SELECTIVE SURFACES
WITH MULTIPLE PERIODIC ELEMENTS

by

JEFFREY A. REED, B.A., M.B.A., M.S.

Presented to the Faculty of
The University of Texas at Dallas

in Partial Fulfillment

of the Requirements

for the Degree of

DOCTOR OF PHILOSOPHY IN PHYSICS

THE UNIVERSITY OF TEXAS AT DALLAS

April 1997

TABLE OF CONTENTS

1. General Introduction.....	1
2. Introduction to Frequency Selective Surfaces (FSS).....	3
Description of FSSs.....	3
Applications for FSSs.....	8
Past Research on FSS Modeling.....	9
Overview of Research on FSS Modeling.....	10
Justification of this Research.....	14
3. Survey of Preliminary Results.....	16
Introduction.....	16
Comparison of Model to Measured Data.....	16
Effect of Varying Periodicity on FSS Resonance Characteristics.....	24
Multiple Apertures per Periodic Cell.....	32
Outline of Remaining Research.....	35
Appendix A: Derivation of the FSS Matrix Equation.....	43
Appendix B: Extending Chen's Method to Multiple Apertures/Patches per Periodic Cell...	49
Bibliography.....	55
Copy of Slides for Oral Presentation.....	59

1. General Introduction

An array of periodic metallic patches on a substrate, or a conducting sheet periodically perforated with apertures, constitutes a frequency selective surface (FSS) to electromagnetic waves. Such structures have been well known in antenna theory for over half a century. At microwave wavelengths, such structures were easy to manufacture and employ in antenna design. However, at near-infrared wavelengths, the size of elements in the FSS are on the order of a micrometer, making such structures much more difficult to manufacture. Advances in lithographic techniques over the last decade has allowed construction of periodic structures with element sizes less than one micrometer. Construction of FSS filters for the near-infrared wavelength regime are no longer difficult to manufacture. It should even be possible using today's state of the art techniques to manufacture FSSs that operate in the optical regime.

The theory of phased array antennas provides the starting point for the study of FSSs. Amitay, Galindo and Wu¹ provide a thorough review of this subject. While much of the underlying theory for FSSs is based on the theory of phased array antennas, methods for adapting it specifically to FSS structures are reviewed by Wu². While the underlying theoretical descriptions of FSSs are well established, much work is still needed in the area of theoretical quantitative analysis of these structures.

It is the purpose of this dissertation to provide some of this theoretical quantitative analysis for a certain class of FSS structures. Specifically, work on thin, perfectly conducting, planar FSSs is presented here. Lithographic techniques can produce planar, semiconductor circuit-like structures with a thickness a mere fraction of a wavelength in the infrared wavelength regime. The assumption of a perfect conductor is justified if the metallic deposits are a highly conducting metal like aluminum or gold, both common materials in construction of FSSs for the near-infrared wavelength region.

With the computational advances over the last half of the decade, it is now feasible to conduct a comprehensive numerical analysis on the behavior of FSS spectral characteristics as periodicity and aperture/patch geometries are varied. The modal method of Chen^{3,4,5} is the basis of numerical analysis for the thin, planar, perfectly conducting frequency selective surfaces modeled in this dissertation. For the rectangular and circular shaped apertures studied here, Chen's method

produced spectral response data that compared favorably to measured data from manufactured FSSs.

Stacking several planar frequency selective surfaces together, usually separating each by a dielectric layer, provides an added degree of freedom in designing a filter with a desired spectral response. Such filters typically display several resonances in their spectral responses. Multiple screen FSS structures have been described in past literature⁶⁻¹⁴, including a detailed methodology for analyzing such systems by Vacchione¹⁵. The problem with multiple screen structures is twofold. First they are difficult and costly to construct - several planar FSSs must be manufactured, then stacked in some fashion. Such a procedure increases the cost and complexity over a single planar FSS in proportion to the number of stacked FSSs. Second, numerical analysis of the structures is vastly complicated due to the coupling effects between the stacked FSSs.

A solution to the problem of design and numerical analysis of multiple screen FSS structures for use in the near-infrared wavelength regime is proposed in this dissertation - a single planar frequency selective surface with multiple apertures/patches per periodic cell. In this type of filter, a *group* of apertures/patches constitutes a unit periodic cell. Instead of the individual elements being periodic, the group is periodic. The idea of a periodic group was proposed by Amitay, Galindo, and Wu¹ (p. 307-309) to modify the grating lobe characteristics of an antenna array. Munk and Luebbers¹⁶ also proposed such a system as the limiting case of zero distance between a stack of planar FSSs.

A planar FSS with multiple periodic elements avoids the cost and complexity of manufacturing several planar FSSs necessary in the stacked design. An added benefit of the multiple periodic element planar design is that it allows for simple rectangular elements to be arranged in a group so as to produce less-polarization dependent filter designs. Numerical analysis of such filter designs is accomplished in this dissertation by modifying the modal method employed by Chen^{3,4,5} to handle a group of periodic apertures/patches.

Solving the inverse problem for FSS structures, that is specifying the FSS structure given the transmission spectral profile, has not been accomplished (nor may it even be possible). A solution to the inverse problem would completely solve FSS filter design problems. While such a complete solution may not be attainable, a general methodology for designing a FSS structure that produces a desired spectral response would go a long way to meeting FSS design needs. It is the goal of the research in this dissertation to add one more key element to such a design methodol-

ogy. Further work in numerically modeling FSS structures, coupled with continuing advancement in computational abilities, should allow for such a design methodology to emerge in the near future.

2. Introduction to Frequency Selective Surfaces (FSS)

2.1 Description of FSSs

As previously stated, a conducting sheet periodically perforated with apertures, or an array of periodic metallic patches, constitutes a frequency selective surface (FSS) to electromagnetic waves. In the literature two generic geometries are typically discussed. The first geometry, commonly referred to as an inductive FSS, performs similarly to a high-pass filter. The second case, or capacitive FSS, is similar to a low-pass filter. If the periodic elements within an FSS possess resonance characteristics, the inductive FSS will exhibit total transmission at wavelengths near the resonant wavelength, while the capacitive FSS will exhibit total reflection.

Capacitive and inductive FSSs derive their name from circuit theory. Figure 1 shows a typical capacitive and inductive FSS constructed out of periodic rectangular patches and apertures respectively. Also included in the figure are their respective equivalent circuit models, along with the corresponding transmission profiles. The rectangular metallic patches in the capacitive FSS act similar to a capacitive circuit. Similarly, the rectangular apertures in the inductive FSS behave like an inductive circuit. Miller¹⁷ provides a thorough discussion of circuit theory techniques in relation to FSSs.

Assuming that the rectangular patches and apertures in figure 1 have identical dimensions and periodicity, the two filters are compliments of one another. If the metallic structure of the filters is assumed to be perfectly conducting, then the application of Babinet's Principle will dictate that the reflection profile of the capacitive FSS will be identical to that of the transmission profile of the inductive FSS. Equivalently, $T_{\text{capacitive}}$ will equal the quantity $(1 - T_{\text{inductive}})$, where T is transmittance. Note that the application of Babinet's Principle for FSS structures requires no substrates to be present, and that the electric field be of "complimentary polarization" as depicted in figure 1.

The FSS periodic surface may be planar, or it may have a profile in the third dimension. Such three dimensional periodic gratings are commonly referred to as Surface Relief Gratings. This dissertation deals exclusively with planar FSSs. Typical lithographic techniques such as the one described in figure 2 will produce a planar metallic filter surface deposited on a substrate. A

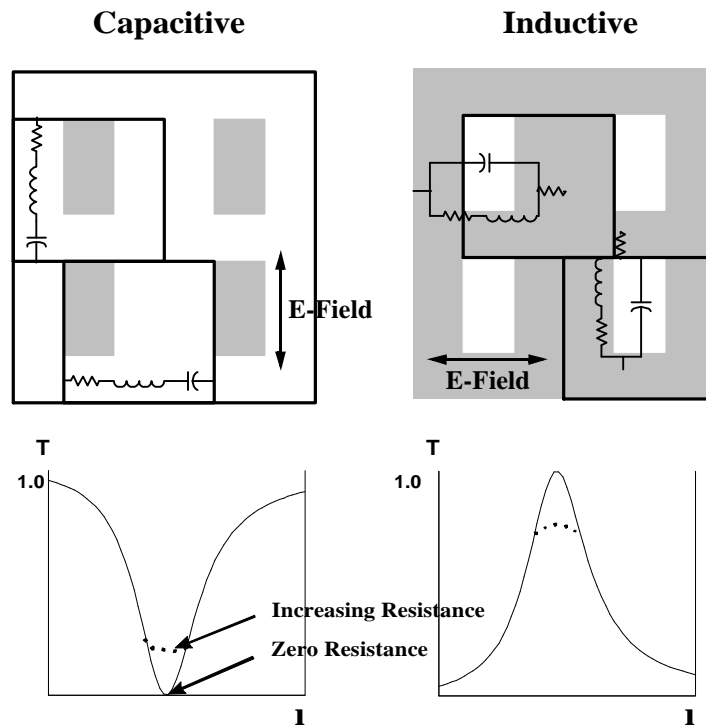


Figure 1 - Capacitive and inductive FSSs with corresponding equivalent circuits and their transmission profiles. Note that only 4 of the periodic elements per filter are shown in the drawing. Typical FSSs for the near infrared region will have hundreds of thousands of periodic elements.

capacitive type filter will consist of metallic patches deposited on a planar substrate. For the inductive type filter, a metallic sheet, usually deposited on a substrate, is perforated with apertures.

The thickness of the FSS relative to the wavelength for which it will be utilized determines whether the FSS is classified as “thick” or “thin”. If the physical thickness of the FSS is a fraction of the smallest wavelength in the wavelength regime for which it will be used, then the FSS can be modeled as a thin filter. For thin filters, it may be possible to model them as the limiting case of “infinitely thin”. Such a model assumes the incident and transmission regions to be in contact with one another at the filter plane, with the filter boundary conditions then imposed at this filter plane. In the thick filter model, the incident region boundary is matched to the incident side of the filter (top of the filter), while the transmission region boundary is matched to the trans-

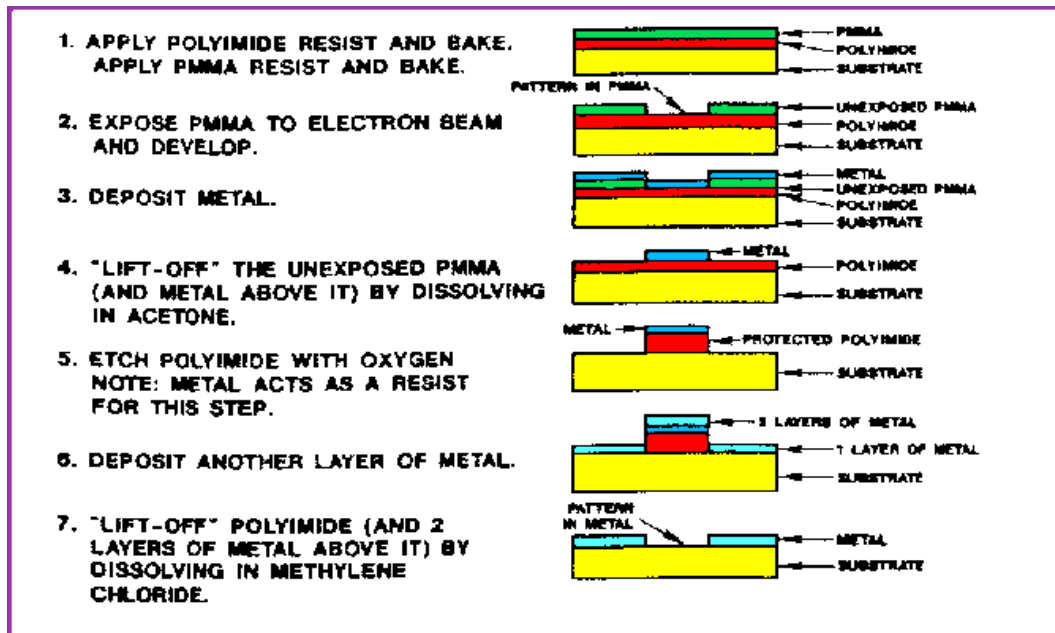


Figure 2 - Typical lithographic process for creating a planar FSS on a substrate. Numerous lithographic techniques exist.

mission side of the filter (bottom of the filter). This model has two distinct boundary regions that must be matched, as opposed to the single region in the thin model.

Since most lithographic techniques producing planar FSS structures are on the order of several tenths of a micrometer thick, these FSS may be considered thin when used in the near infrared wavelength region. For this reason, it was decided to use an infinitely thin model for this research.

Conductivity of the material used in the FSS constitutes the final consideration when modeling a FSS. Assuming a perfectly conducting surface, one can simplify the modeling process, especially for the thin filter model. Several techniques, such as the work of Chen^{3,4,5}, combine the limiting cases of a perfectly conducting material with the infinitely thin model assumption, to help ease the computational requirements of the problem. Since most lithographic techniques for construction of FSSs in the infrared region utilize metals such as aluminum or gold, which are highly conductive in this wavelength regime, a model assuming a perfectly conducting material should

provide a reasonable approximation to the actual filter.

For the reasons stated in this section, it was decided to model FSSs for this research as a perfectly conducting, infinitely thin, planar structure. While this model doesn't account for all possible types of FSSs, such a model should adequately account for a large percentage of FSS constructed for use in the near infrared wavelength region.

The periodic elements in a FSS are most commonly arranged in a rectangular array as shown in figure 3. However, the more general geometric arrangement is a triangular array, also shown in figure 3. Note that the periodicity in the triangular array exists along the x -axis, and the skewed y' -axis. If the skew angle $\alpha=90^\circ$, then the triangular array becomes a rectangular array. The geometric labeling shown in Figure 3 will be used throughout this dissertation.

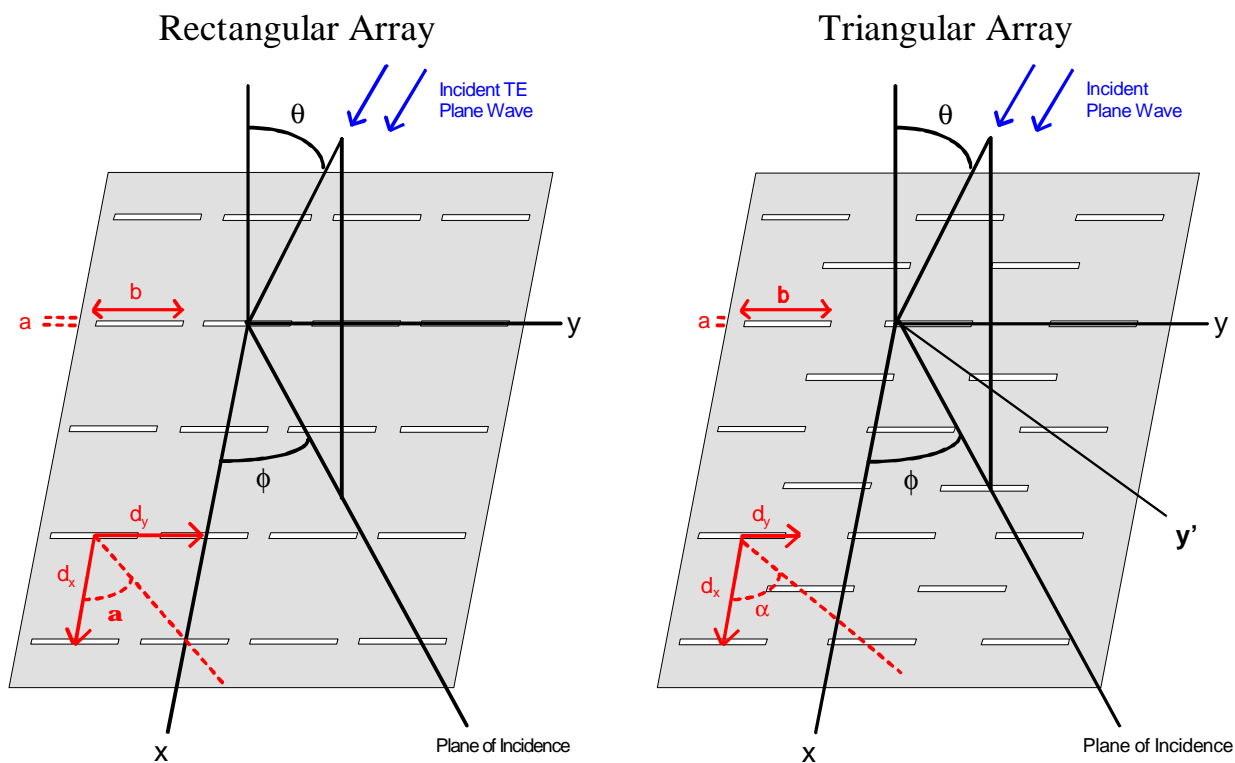


Figure 3 - A rectangular array and the more general triangular array of apertures (or patches) that form a FSS. Note that when the skew angle $\alpha=90^\circ$, the triangular array becomes a rectangular array.

It should be pointed out that the incident field is considered to be a plane wave. The angle of incidence and polarization is not restricted in the FSS model used in this research. Polarization states are typically divided into the orthogonal TE (electric field perpendicular to plane of incidence) and TM (magnetic field perpendicular to plane of incidence) states.

Certain key concepts will be referenced throughout this dissertation. *Periodicity* of the FSS has been described in relation to figure 3. Since the apertures/patches of the FSS are arranged in a periodic fashion, it is possible to describe the field at the filter plane in terms of only one unit periodic cell. *Floquet's theorem* states that if a linear differential equation has periodic coefficients and periodic boundary conditions, then the stable solutions will generally be a periodic function times an exponentially decreasing function.¹⁸ Through the application of this theorem, the field in any other periodic cell will be related to the reference cell in terms of an exponential function. The *diffraction edge* (or diffraction edge wavelength) is the wavelength which separates the wavelengths at which only the *specular order* (or zeroth order) and *higher diffractive orders* propagate in the far field region. At wavelengths greater than the diffraction edge, only the specular order propagates in the far field region.

At a wavelength slightly shorter than when another higher diffractive order begins to propagate, *Wood's anomalies*^{19,20,21} may occur. These are wavelength regions of anomalous spectral response where rapid variations in the transmission/reflection profiles of the FSS (and diffraction gratings in general) occur. In a typical triangular array, the location of the diffraction edge is related to the distance of the *nearest neighbor*. The nearest neighbor distance in this case is the physical distance between the center of two periodic elements measured along the skewed y' axis.

2.2 Applications for FSSs

In the near infrared wavelength region, frequency selective surfaces are primarily used in filtering applications. Some applications include bandpass filters, polarizers, and beam splitters. As previously stated, if the periodic elements within a FSS possess resonance characteristics, the inductive FSS will exhibit total transmission at wavelengths near the resonant wavelength, while the capacitive FSS will exhibit total reflection. This feature allows an FSS with the proper elements to perform like a narrow bandpass filter. Similarly, a complimentary design can be created to selectively absorb narrow bandpass regions. Specific applications of these types of FSS filters

include narrowband astronomy filters, and filters for spacecraft instrumentation.

If the periodic elements within a FSS possess a resonance characteristic that is polarization dependent, such a feature may be exploited to produce a polarizer. If this polarization dependence is utilized so that one polarization is totally reflected, while the orthogonal polarization is totally transmitted, the FSS may then be employed as a beam splitter. Using FSSs allows construction of polarizers and beam splitters for wavelengths where traditional materials make construction of such devices impractical.

2.3 Past Research on FSS Modeling

As mentioned in the introduction, phased array antenna theory^{1,22} provides the theoretical foundation for FSSs. Work specifically related to FSSs is numerous and diverse, and can be categorized in several ways. For simplicity, past research on FSSs will be categorized based on the technique used to analyze the filter.

The method for analyzing frequency selective surfaces can be broken down into several categories - circuit theory techniques, modal expansion techniques and iterative techniques. The circuit theory approach utilizes the quasi-static approximation to derive the equivalent circuit model for the FSS. Ulrich²³ provided an example of this approach for thin metallic mesh grids and their complementary structures. In the modal expansion technique, Floquet modes in space (diffracted orders) are matched with the aperture modes (or current modes) to form an integral equation. This integral equation is solved by a technique such as the method of moments²⁴ or the conjugate gradient technique²⁵. Iterative methods²⁶ can avoid large matrix storage requirements by utilizing iteration to avoid explicitly computing the matrices. In the spectral iterative technique, the current on the surface of the conducting region is the quantity being iterated. The merits of the various techniques are discussed by Wu².

According to Wu, modal expansion techniques comprise the largest class of the FSS analysis methods. They also have a history of predicting the spectral response of FSSs to a high degree of accuracy. Chen³ proposed a modal expansion technique based on the method of moments to analyze a thin, perfectly conducting screen perforated by apertures. This method may also be extended to circular apertures by using circular waveguide modes for the expansion functions, as described by Chen⁵. Capacitive filters (metal patches as opposed to apertures) can be

analyzed by applying a similar procedure, as described by Chen⁴, Montgomery²⁷, and Dawes, et al²⁸.

Stacking multiple FSSs together, usually with each separated by a dielectric layer, has been also been studied⁶⁻¹⁵. Munk and Luebbers¹⁶ presented the limiting case of two stacked FSSs (consisting of dipole-like patches) with different periodicities, separated by zero distance, as well as commenting on the dual resonance nature of such structures. This structure is, in essence, a single planar FSS with two periodic patterns superimposed. One final hybrid FSS structure was described by Orta, Savi, and Tascone²⁹, where crossed patches were deposited inside of circular apertures. Such a structure would be a capacitive FSS superimposed on an inductive FSS.

2.4 Overview of Research on FSS Modeling

FSS constructed for the near infrared wavelength region will be physically thin, on the order of a fraction of a micrometer. Such structures will require a substrate for support. It is often common practice to protect the filter by sandwiching it between a substrate and superstrate. Thus, the model for the FSS must take into account these substrates/superstrates. Figure 4 describes the substrate model used in throughout this research.

The FSS filter surface may be sandwiched between two thin slabs constructed of different dielectric materials. The semi-infinite space on the incident side of the “dielectric sandwich”, and the corresponding semi-infinite space on the transmission side, can also be considered as a dielectric material if need be. These semi-infinite “substrates” can be used to model “thick” dielectrics. A dielectric is considered thick when the reflections off of the back surface of the dielectric are incoherent with respect to diffraction from the FSS surface (on the front surface of the dielectric). For such cases, it is a simple matter to add the effect of a back surface to the semi-infinite dielectric by equating the situation to the reflection/transmission at a plane dielectric interface.

As pointed out in the previous section, the method of Chen^{3,4,5} was chosen to numerically model the FSS geometry presented in figure 4. A review of the mathematical model used by Chen, plus some slight modifications to adapt it to the dielectric substrate model in figure 4 is presented in Appendix A.

To sum up the procedure briefly, Chen’s method is a modal method. The incident plane wave field is decomposed into a linear combination of zeroth order TE and TM Floquet modes.

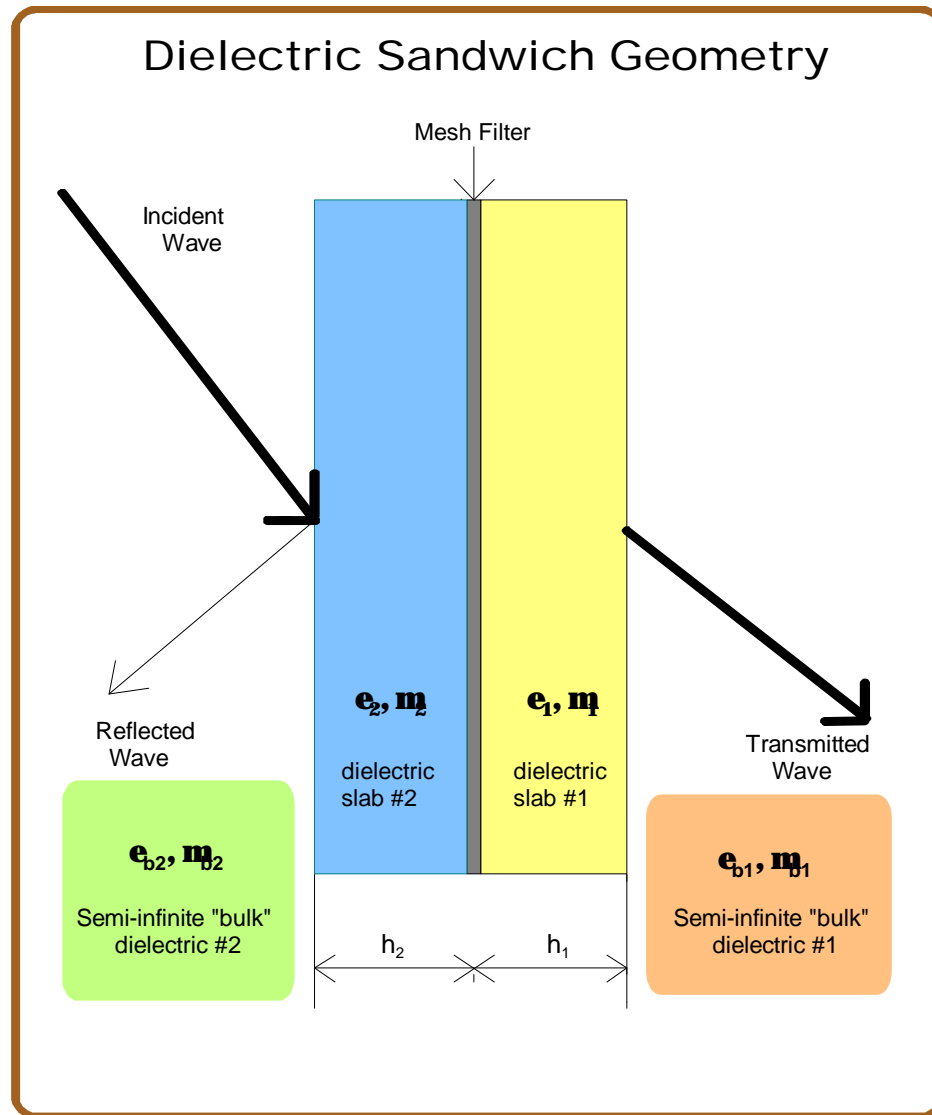


Figure 4 - Substrate model used for this research. A thin dielectric substrate and/or superstrate is included directly in the model. A “thick” substrate may be modeled as a semi-infinite dielectric.

The unknown reflected and transmitted fields are each expanded into an infinite series of Floquet modes with unknown coefficients. Since the filter itself is considered as the limiting case of being infinitely thin, the expansions of the three field components are matched at this plane. The integral representation of the reflection and transmission coefficients are substituted for these

unknown reflection and transmission coefficients, resulting in an integral equation. In order to impose the boundary conditions at the filter plane, the field in the FSS apertures (or on the patches) is expanded in another set of orthonormal basis functions that span the space of the aperture (or patch). This field expansion is then substituted into the integral equation. Using Galerkin's moment method, the integral equation is transformed into a matrix equation, and solved for using matrix inversion. At this point, the transmission and reflection coefficients can be solved for.

As will be shown in the next chapter, Chen's method works very well in predicting the spectral response for infinitely thin, planar, perfectly conducting FSSs with periodic aperture/patch elements. To speed up convergence and therefore computational time, the basis functions used in the expansion of the field inside the FSS apertures (or on the patches) are the waveguide modal functions (or their dual functions in the case of patches). Thus Chen's method is limited to cases where the modal functions of the apertures/patches can be specified. For the research presented here, this includes rectangular and circular shaped apertures/patches.

A natural extension to Chen's method is having multiple apertures/patches in a *group* so that the *group* is periodic (as opposed to the individual elements). Figure 5 shows such an example. Consider such a FSS in the inductive case (multiple apertures per periodic cell). Since the filter is modeled as a perfect conductor, the transverse field at the plane of the filter is within the apertures only. For an "unit cell" of N apertures, the transverse field contribution at the plane of the filter is

$$\vec{E}_t = \sum_{i=1}^N \vec{E}_t^{(i)} \quad (1)$$

where the superscript i denotes the i th aperture within the group. This value of the field can then be substituted back into the integral equation to extend Chen's method to the case of multiple apertures per periodic unit cell. A more complete description of this procedure is presented in Appendix B.

The same idea can be applied to a FSS in the capacitive case (multiple patches per periodic cell). For a mesh with patches, the sum of the induced currents on each patch within the "unit cell" is substituted into the appropriate integral equation. This produces the corresponding integral equation for the capacitive case.

There are several benefits to constructing these multiple aperture/patch per periodic unit

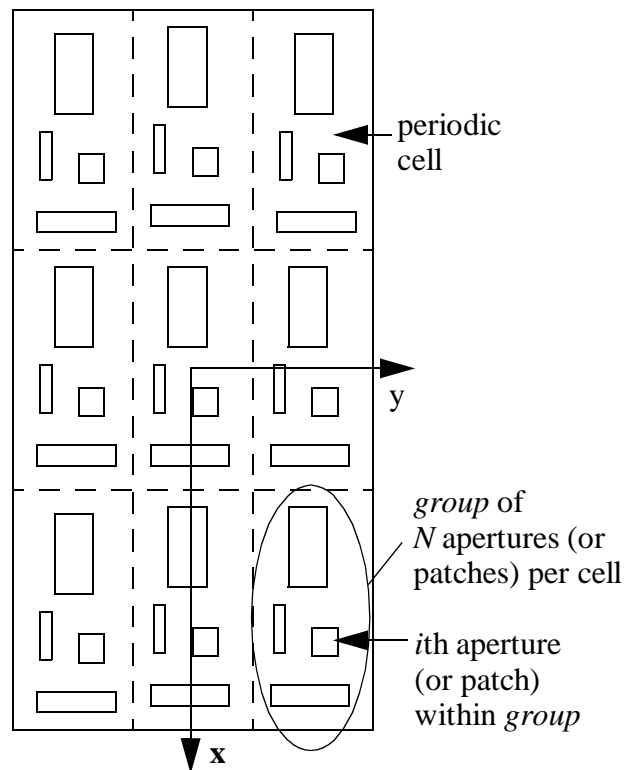


Figure 5 - Typical geometric configuration for a FSS with multiple apertures (or patches) within a periodic cell.

cell FSSs. They are easier to construct than multiple screen FSS structures. Unlike a stacked FSS, this approach has only one filter surface to construct. Since there are multiple arrays of periodic elements superimposed, it is possible to construct FSSs with dual resonance bandpass transmission profiles. It will also be shown in a later chapter that it is possible to create transmission profiles with resonance structures that possess a narrower bandpass than possible with simple periodic structures. The final benefit of such structures is the possibility to create less polarization dependent geometric configurations with simple elements. Instead of using more complex periodic elements like crosses, one can get similar polarization effects using several rectangular elements in a periodic group. By rotating half of the rectangular elements within a periodic group by 90° , and arranging all of the elements in a symmetric fashion within the periodic group, the structure will exhibit similar polarization characteristics to a cross.

This concludes the extent of the current research for this dissertation. However, there are several extensions possible for future research possibilities. While most of the work in this dissertation considers the periodic group within a multiple aperture/patch per periodic unit cell FSS to contain two elements, it should prove no problem to extend this procedure to include more than two elements per periodic group. Also the “superimposed arrays” in the multiple aperture/patch per periodic cell FSS need not have the same period. Another extension would be to consider the FSS material to be a non-perfect conductor. While a method other than Chen’s would have to be employed, it is important to be able to handle surfaces that have some loss. While only planar FSS were considered here, non-planar, three dimensional periodic structures can be constructed. Also, the work presented here considered FSSs illuminated with only a plane wave. Another extension of this research could include studying the effect of varying the illumination coherence.

2.5 Justification of this Research

While extensive research has been conducted on FSSs, no extensive analysis on relationship between periodicity, periodic element geometry, and the spectral profile exists. This extensive knowledge base is necessary in order to construct a FSS design methodology. Currently, a filter designer uses the available general knowledge on FSSs as a starting point in the filter design. Then a computer model simulation is run to see if the spectral output is as expected. Next, tweaking of the design parameters occur, followed by a revised computer modeling run. This iterative process continues until the desired spectral output is achieved. At this point a filter is manufactured, and its spectral output measured. If the computer model was accurate, hopefully the actual spectral output of the FSS will resemble the desired output.

Unfortunately this method is time consuming. Computer runs do not produce “instantaneous results”, and often the “parameter tweaking” does not produce the change that was anticipated. If the relationship between periodicity, periodic element geometry, and the spectral profile is understood, it should be possible to design a FSS, test it once with a computer model, then manufacture it. The next best solution would be development of a computer modeling routine that could produce the spectral output of the FSS in “real time”.

When considering the more specific problem of multiple apertures/patches per periodic cell, there has been only a few references to this technique in past literature, as described in a pre-

vious section. These references were in relation to antenna theory, or as a theoretical consideration as the limiting case of stacking FSSs. There are few examples of FSSs with multiple apertures/patches per periodic unit cell that have been manufactured and measured. In any event, there has been little if no research done on creating multiple resonance effects using these types of FSS.

Finally, the examination of the effects of Wood's anomalies on the spectral profiles of FSSs is incomplete in the literature. Research on these anomalies was described in another section. However, it was found while conducting the research for this dissertation, that Wood's anomalies are not prominent (or even present at all) in some FSS transmission spectra. It will be shown in a following chapter that certain FSSs with multiple aperture/patches per periodic unit cell do not exhibit Wood's anomalies anywhere near the diffraction edge. This behavior needs to be understood because these types of FSS, which can exhibit multiple resonance features, frequently have the diffraction edge at a wavelength that is of interest in the filter design. Unexpected Wood's anomalies suddenly appearing in the spectral output of the completed filter would not be desirable.

3. Survey of Preliminary Results

3.1 Introduction

In this chapter, some preliminary research results are presented. The first section will compare calculated spectral responses from the computer model with measured FSS data. This should establish the validity of the computer model. In the first case a capacitive FSS consisting of rectangular aluminum patches in a rectangular array on a ZnS substrate is examined. The next case compares the calculated and measured data for rectangular aluminum patches in a triangular array on a ZnSe substrate. The final case compares the results for rectangular patches on a CaF substrate. This final case is an example of multiple patches per periodic cell, where a group of four rectangular patches constitute a periodic cell.

The second section presents an excerpt from a report on research supported by Texas Instruments, Inc. on the effects of varying periodicity and aperture dimensions for an inductive FSS consisting of rectangular shaped apertures (no substrate). Understanding the effects of periodicity and aperture shape is an important preliminary step in understanding the effects of having multiple aperture/patches per periodic cell. Since this was an attempt to understand the dynamics of periodicity and aperture shape, the idealized case of no substrate present was studied. The next step in this particular study would be examination of the effects of adding a substrate to the problem.

The final section of these preliminary results is an excerpt from a recently submitted journal paper on multiple apertures per periodic cell, coauthored with Dale M. Byrne. This excerpt presents several variations on the case of two rectangular apertures per periodic cell. This was also an idealized case of no substrate present.

3.2 Comparison of Model to Measured Data

Measured spectral data from three different FSSs is compared to the results predicted from the computer model used in this research. This comparison should help to validate the computer model used. It is hoped that further comparisons between predicted and measured results can be carried out in the future.

3.2.1 Comparison to Data from Schimert

Figure 6 shows the geometry of a frequency selective surface constructed by Schimert, Koch, and Chan³⁰. The FSS consisted of rectangular aluminum patches arranged in a rectangular array on a thick ZnS ($n=2.2$) substrate. The measured zeroth order transmittance data for a normally incident plane wave is reproduced in figure 7 along with the results calculated from the computer model. Since the back surface reflection of the substrate had been subtracted from the measured data, the calculation assumed a semi-infinite substrate of $n=2.2$.

Agreement of the resonance location is quite good, along with the general shape of the transmittance profile. The fall-off of the transmittance at longer wavelengths can be attributed to absorption in the ZnS substrate. Unfortunately, the computer model does not account for absorption losses in the substrate. The diffraction edge, located at $\lambda_d = 6.6 \mu\text{m}$, is evident in both the measured data and calculated transmittance spectra.

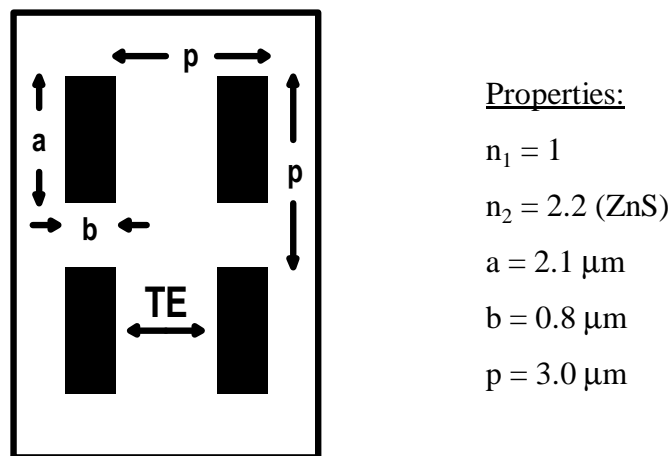


Figure 6 - Geometry used in FSS constructed by Schimert, Koch, and Chan. The filter consisted of rectangular aluminum patches in a rectangular array on a thick ZeS substrate. The indices of refraction n_1 and n_2 refer to the incident side and transmission side respectively.

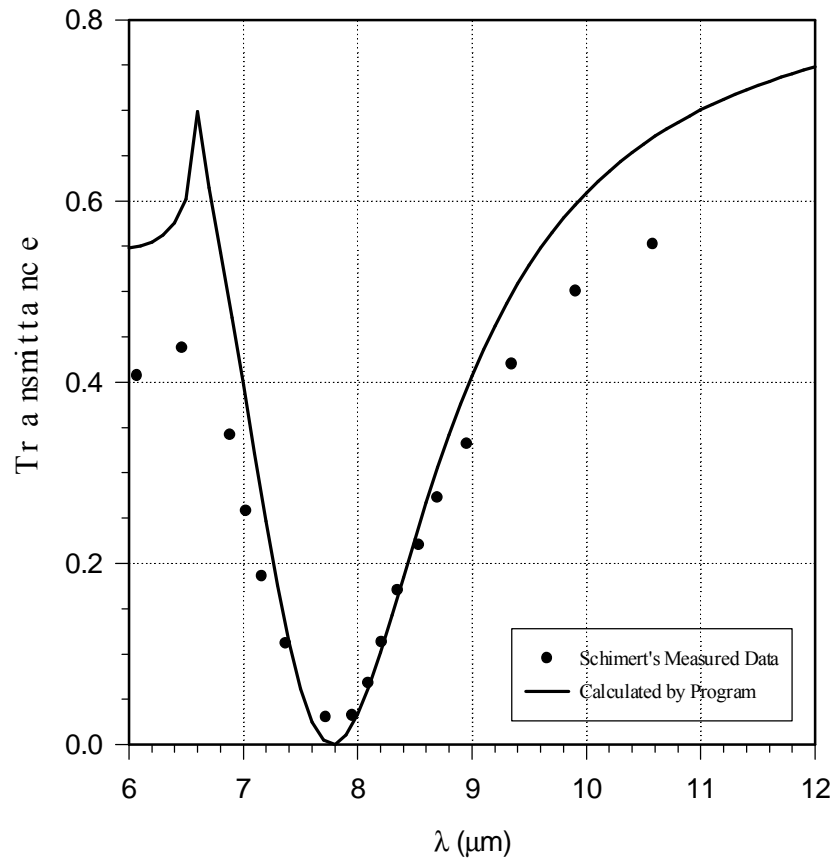


Figure 7 - Comparison of measured zeroth order transmittance data from FSS described in Figure 6 with that calculated using the computer model using the Chen formulation. The fall-off in transmittance at long wavelengths is due to absorption in the substrate.

3.2.2 Comparison to Data from Byrne

Figure 8 shows the geometry of a frequency selective surface constructed by Byrne³¹. The FSS consisted of rectangular aluminum patches arranged in a triangular array on a thick ZnSe ($n=2.4$) substrate. The measured zeroth order transmittance data for a normally incident plane wave is reproduced in figure 9 along with the results calculated from the computer model. Unlike in the previous example, the back surface reflection of the substrate had not been subtracted from the measured data. Since the calculation assumed a semi-infinite substrate of $n=2.4$, a back surface reflection correction was added to the values calculated from the computer model.

Because the substrate is “thick” compared to the wavelength (2 mm thick), essentially the reflections off of the back surface of the dielectric are incoherent with respect to diffraction from the FSS surface. Thus it is possible to approximate this correction as the problem of transmission

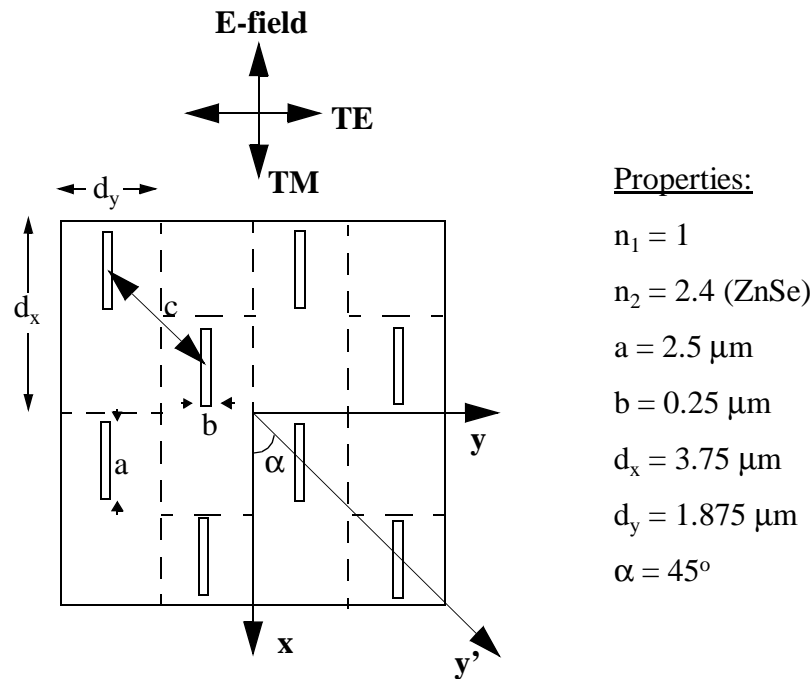


Figure 8 - Geometry used in FSS constructed by Byrne. The filter consisted of rectangular aluminum patches in a triangular array on a thick ZeSe substrate. The indices of refraction n_1 and n_2 refer to the incident side and transmission side respectively.

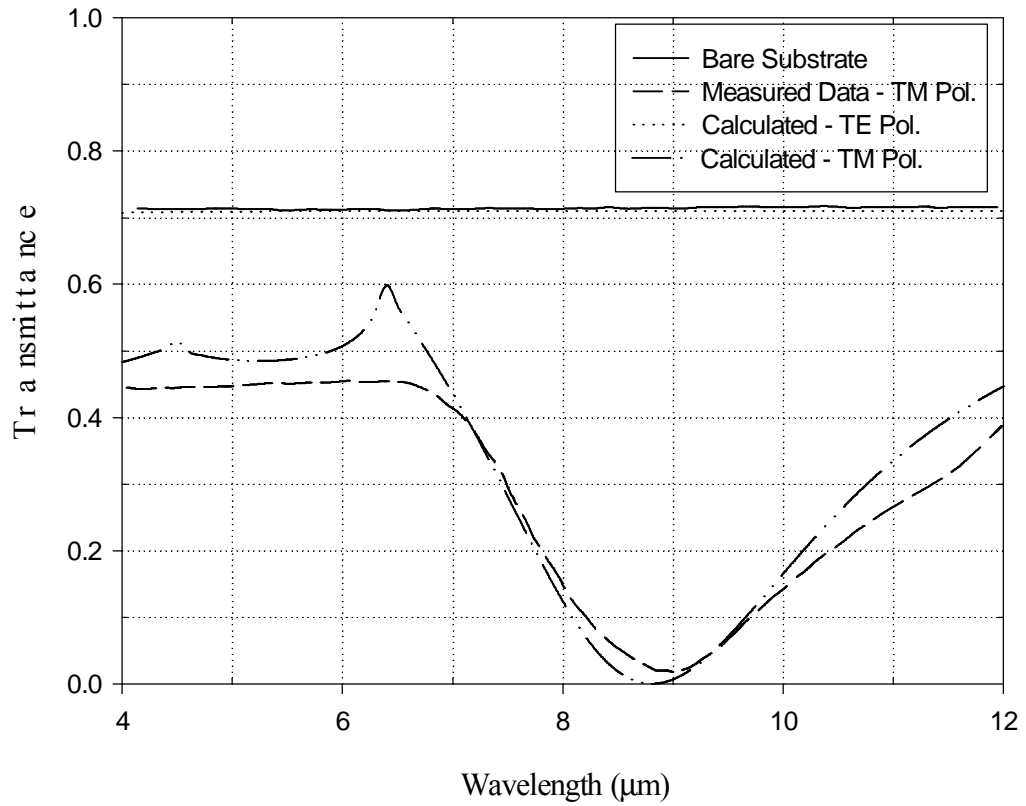


Figure 9 - Comparison of measured zeroth order transmittance data from FSS described in Figure 8 with that calculated using the computer model using the Chen formulation. The calculated data (which assumed a semi-infinite substrate) had the effect of the reflection at the back surface of the thick (2mm) ZnSe substrate added, so that it may be compared to the actual measured data.

through a plane dielectric interface. In this case, the transmission, corrected to include a back substrate surface, is given by

$$T_{total} = \frac{T_1 T_2 e^{-\tau d}}{1 - R_1 R_2 e^{-2\tau d}} \quad (2)$$

where T_1 and R_1 are the transmission and reflection of the FSS into a semi-infinite substrate, T_2 and R_2 are the transmission and reflection of the back dielectric substrate surface, d is the substrate thickness, and τ is the substrate absorption coefficient. T_1 and R_1 are values outputted by the computer program for the FSS on a semi-infinite substrate, while T_2 and R_2 are the values for transmission and reflection at normal incidence for a plane interface between the ZnSe dielectric and air. The value for τ is derived from the measurement of the bare substrate ($\tau d = 7.5 \times 10^{-5}$ for the substrate used in this example). The transmission value corrected using the above equation is the value plotted in figure 9.

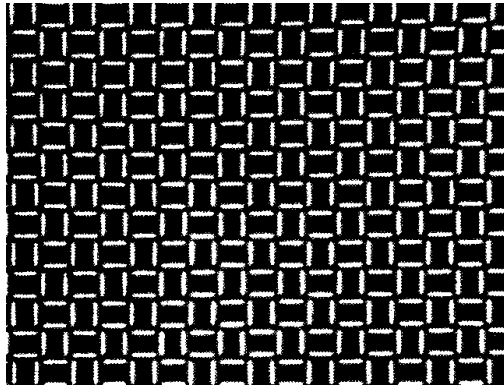
As in the Schimert example, the computer model predicts the location of the resonance and overall transmission spectra shape fairly well. For the TE polarization (E-field perpendicular to the long dimension of the rectangular patch), the FSS is nearly invisible to the incident wave, so total transmission through the filter surface should occur. The resulting transmission profile should be very similar to that of a bare substrate, which it is. For the orthogonal TM polarization (E-field parallel to the long dimension of the rectangular patch), the slight deviation between measured and calculated values may be accounted for in the slight variability in the width of the rectangular patches on the FSS. Actual measurements of the rectangular patch dimensions on the FSS show that the widths of the patches vary slightly from the value $b = 0.25 \mu\text{m}$.

3.2.3 A Second Comparison to Data from Byrne

Figure 10 shows the geometry of a second frequency selective surface constructed by Byrne³¹. The FSS consisted of rectangular aluminum patches on a thick CaF ($n=1.4$) substrate. The rectangular patches are arranged such that a group of four constitute an unit cell, with the unit cells in a triangular array pattern. With this configuration, the nearest neighbor concept applies to the periodic unit cell, not the individual rectangular patch element. The nearest neighbor distance, located along the skew axis, is $4\sqrt{2} \mu\text{m}$. This value multiplied by the substrate index of 1.4 puts the diffraction edge at $7.9 \mu\text{m}$.

The measured transmittance data for a normally incident plane wave is reproduced in fig-

Optical Microscope Photograph



Properties:

$n_1 = 1$ $n_2 = 1.4$ (CaF)
 triangular array, $\alpha = 45^\circ$
 $d_x = 8.0 \mu\text{m}$ $d_y = 4.0 \mu\text{m}$
 $a_1 = a_2 = 3.19 \mu\text{m}$ $b_1 = b_2 = 0.6 \mu\text{m}$
 $a_3 = a_4 = 0.6 \mu\text{m}$ $b_3 = b_4 = 3.19 \mu\text{m}$
 elements spaced $3.0 \mu\text{m}$ apart within cell

Unit Cell Geometry

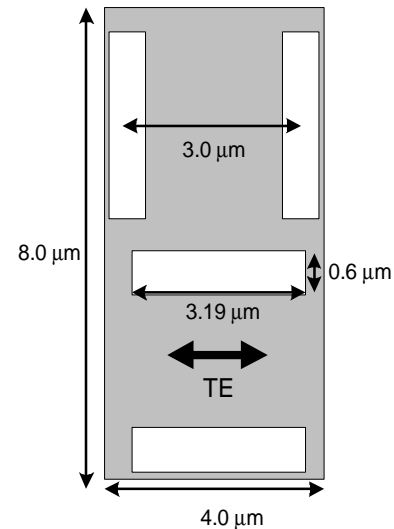


Figure 10 - Geometry used in a second FSS constructed by Byrne. The filter consisted of rectangular aluminum patches on a thick (2mm) CaF substrate. The rectangular patches are arranged such that a group of four constitute an unit cell, with the unit cells in a triangular array pattern. The indices of refraction n_1 and n_2 refer to the incident side and transmission side respectively.

ure 11 along with the results calculated from the computer model. As with the previous example from Byrne, the back surface reflection of the substrate had not been subtracted from the measured data. The calculation again assumed a semi-infinite substrate, except this time $n=1.4$. A back surface reflection correction was added to the values calculated from the computer model using the correction given in equation (2). From figure 11 it is clear that the absorption of the bare substrate is not constant over the wavelengths examined. Therefore, the value for the substrate

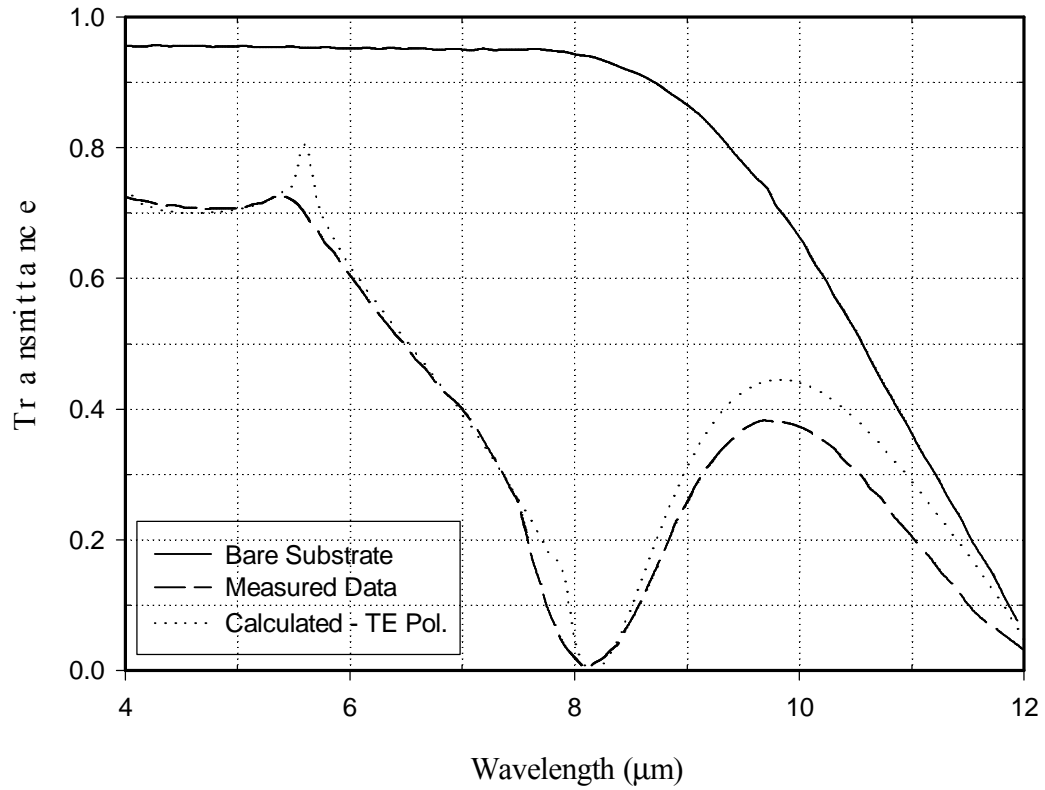


Figure 11 - Comparison of measured transmittance data from FSS described in Figure 10 with that calculated using the computer model using the Chen formulation. The calculated data was corrected for the reflection at the back surface of the thick (2mm) CaF substrate so that it may be compared to the actual measured data. Also the absorption of the substrate was accounted for in the correction.

absorption constant τ must be found for each calculated value from the computer model using the measured bare substrate data.

As in the previous examples, the computer model predicts the location of the resonance and overall transmission spectra shape fairly well. Due to the symmetry of the FSS geometry, there is no difference in the spectral profiles for the incident TE and TM polarizations. The deviation at the diffraction edge at $\lambda_d = 7.9 \mu\text{m}$ is most likely due to the resolution of the measured values and calculation values. Since the first diffracted order is beginning to propagate in the substrate, rapid variations, or Wood's anomalies, are likely to occur at a wavelength just short of the diffraction edge. The same is true for the wavelength corresponding to the nearest neighbor distance of $4\sqrt{2} \mu\text{m}$, where the first reflected diffractive order is beginning to propagate.

Finally, the deviation between the measured and calculated values for wavelengths greater than the resonance wavelength of $8.2 \mu\text{m}$ is due to the strong substrate absorption. The correction for absorption in equation (2) is of first order, assuming only the propagating specular diffractive order is affected by absorption. However, the coupling between the evanescent modes in the substrate is also affected by absorption. This effect is not accounted for in the calculation, so when absorption in the substrate becomes large, the absorption correction deviates from the measured value. The computer program can account for substrate absorption, but the absorption value must be constant over the wavelengths in the calculation. Unfortunately, the substrate absorption is not constant over the wavelengths of interest in this example.

3.3 Effect of Varying Periodicity on FSS Resonance Characteristics

The following is an excerpt from a report on research supported by Texas Instruments, Inc. on the effects of varying periodicity and aperture dimensions for an inductive FSS consisting of rectangular shaped apertures (no substrate). The figures have been renumbered to conform with this text.

3.3.1 Equal Periods in x and y directions

Initial investigations considered a rectangular array of rectangular apertures with a period of $d_x = d_y = 6.0 \mu\text{m}$. The investigation considered the simplest case of a free standing mesh (no dielectric substrate), with a normally incident plane wave. Figure 12 details the geometry of the FSS used in this investigation. Polarization of the wave when the electric field vector points per-

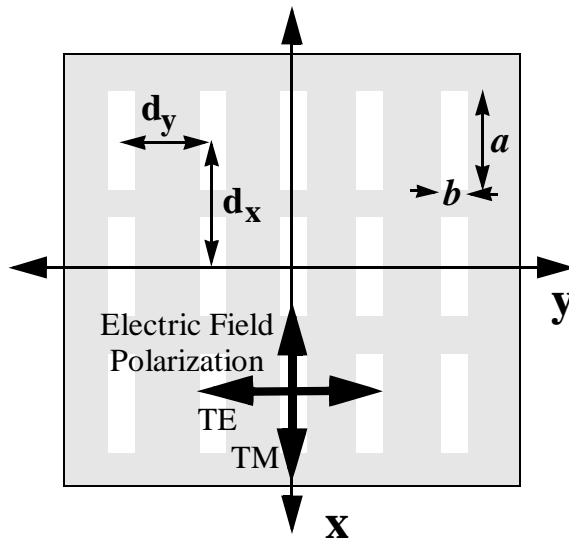


Figure 12 - Geometry of free-standing rectangular array of rectangular apertures used in analysis of FSS transmission profiles. The analysis considers a normally incident plane wave with either TE or TM polarization.

pendicular to the long dimension of the rectangular apertures is designated as TE, while the designation TM refers to the case when the electric field vector is parallel to the long dimension of the apertures. The length of the apertures, labeled a , remained constant at $5.0\mu\text{m}$, while the width, b , varied ($0.25\mu\text{m}$, $0.5\mu\text{m}$, $1.0\mu\text{m}$, $2.0\mu\text{m}$, $3.0\mu\text{m}$, $4.0\mu\text{m}$, $5.0\mu\text{m}$). Consequently, the aspect ratios ($a:b$) of the apertures varied from 20:1 (near slits) to 1:1 (squares).

The top graph in figure 13 plots the transmissivity T versus wavelength, λ_0 , for this set of aspect ratios. From the plot in figure 13, several conclusions become apparent. For $b = 0.25\mu\text{m}$ (near slits), the transmission profile exhibits a resonant shape with the peak transmissivity occurring at a “resonant” wavelength, λ_r , of $10.4\mu\text{m}$. As the aspect ratio decreases (the slits become wider), λ_r decreases, while the bandwidth, as indicated by the full-width at half maximum (FWHM) increases. When the aperture width, b , becomes greater than or equal to $4.0\mu\text{m}$ (apertures are approaching squares), the line shape becomes highly asymmetrical. Examination of figure 13 reveals the location of the diffraction edge, λ_d , at the nearest neighbor distance of $6.0\mu\text{m}$

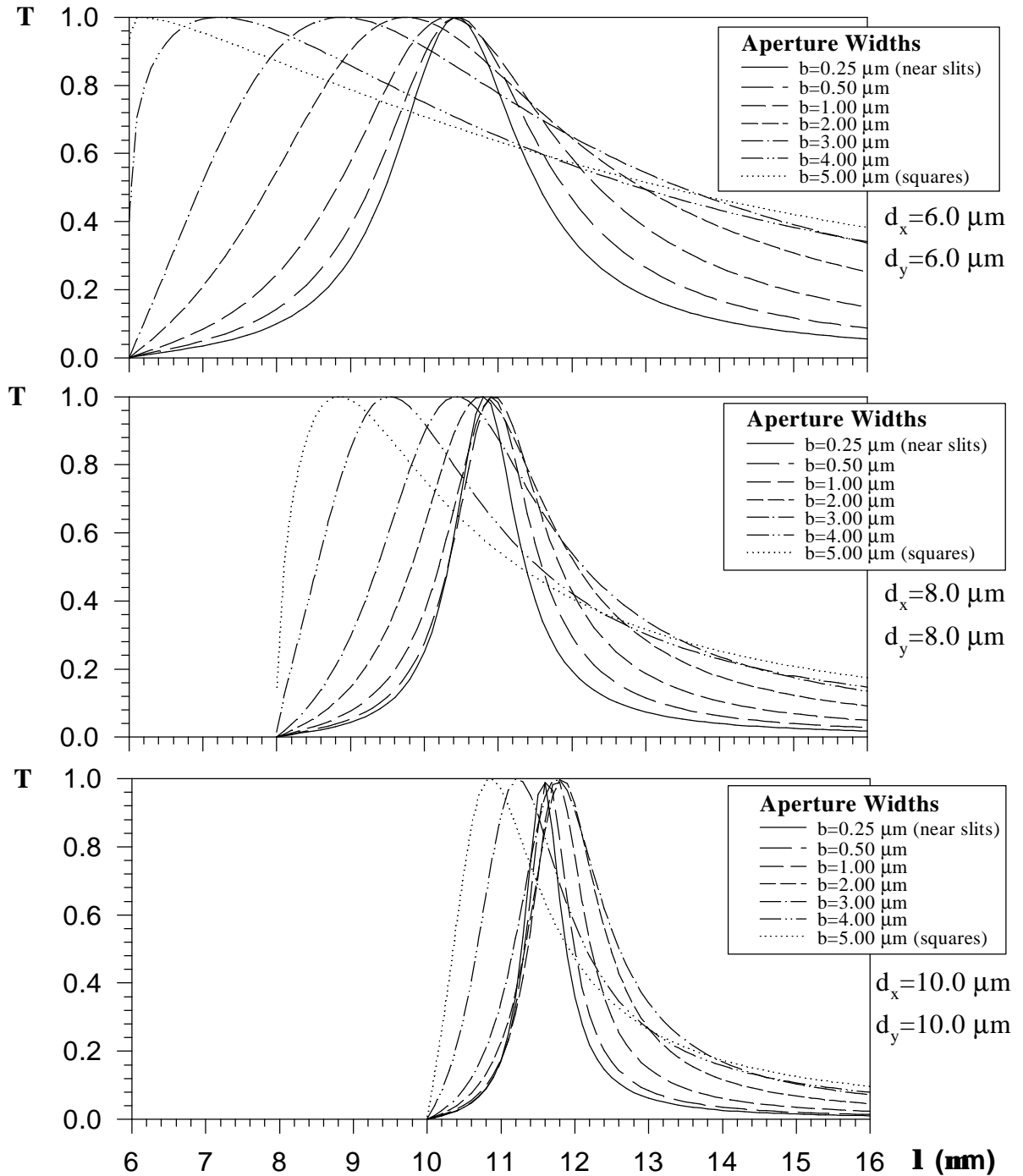


Figure 13 - Transmission profiles for FSSs consisting of a free-standing rectangular array of rectangular apertures of varying width and a constant length ($5.0 \mu\text{m}$). Periodicity of the array is systematically varied equally in the x and y directions ($d_x = d_y$). Polarization is TE.

for this particular FSS geometry; hence, for wavelengths less than λ_d higher order modes begin to propagate. As is apparent from the graph the diffraction edge appears to “anchor” the profile, and hence, as the aspect ratio decreases, λ_r begins to approach λ_d , and the classic resonant transmission profile becomes compressed on the short wavelength side of resonance.

Transmission profiles were also generated, using the same aperture geometries as discussed in the previous example, but with x and y periods ($d_x = d_y$) of $7.0\mu\text{m}$, $8.0\mu\text{m}$, $9.0\mu\text{m}$, and $10.0\mu\text{m}$. The center graph and the lower graph in figure 13 shows the results for periods of $8.0\mu\text{m}$ and $10.0\mu\text{m}$, respectively. As in the first case, the profiles were plotted only for wavelengths that exceeded λ_d .

From the three sets of curves in figure 13 several trends stand out. For a given aspect ratio, the bandwidth decreases as the period ($d_x = d_y$) increases. In other words, increasing only the period yields sharper resonance peaks. As the period increases and the resonance peaks become sharper, the distortion from the diffraction edge on the short wavelength side of the resonance peak also lessens. For the $10.0\mu\text{m}$ period (the bottom plots), significantly less distortion is present, maintaining a general resonant characteristic even for the square apertures.

As is also apparent from figure 13, the location of the peak transmissivity is affected dramatically by both the period and the aspect ratio. First, for a given aspect ratio, λ_r increases as the period ($d_x = d_y$) increases. For example, looking at the case of near slits, with $b = 0.25\mu\text{m}$, for periods of $6.0\mu\text{m}$, $8.0\mu\text{m}$, and $10.0\mu\text{m}$, (the solid lines in each of the three plots), λ_r shifts from near $10.4\mu\text{m}$, to $10.8\mu\text{m}$, to $11.5\mu\text{m}$. Second, the variation in resonance wavelength as a function of aspect ratio is less if the period is increased. In the top set of plots ($d_x = d_y = 6.0\mu\text{m}$), λ_r differs by almost $4.5\mu\text{m}$ between the square apertures and the near slits, but less than $2\mu\text{m}$ for the bottom set of plots ($d_x = d_y = 10.0\mu\text{m}$). Finally, λ_r decreases monotonically as the aspect ratio decreases (moving from near slits to square apertures) for a period of $6.0\mu\text{m}$. However, for the other periods examined, λ_r initially increases as the aspect ratio decreases, before beginning to decrease.

The main conclusions derived from figure 13 can be summarized as follows:

(1) The resonance character of the transmission profile is sharpened with increasing period, and

(2) the dependence of the resonance wavelength, λ_r , on variations in aspect ratio is reduced with increasing period.

From these conclusions the hypothesis is made that as the period continues to increase, the trans-

mission profile from all different aspect ratios will approach a very narrow transmission spike, located at a wavelength just slightly longer than λ_d .

The fact that the resonance wavelength is closer to the diffraction edge for larger periods is verified by re-examining the data already shown in figure 13. Figure 14 shows plots of λ_r/λ_d vs. d ($=d_x=d_y$) for each of the aperture widths considered previously. For the five narrowest apertures, the ratio monotonically decreases as the period is increased. Although the maximum period considered is $10\mu\text{m}$, it is clearly evident that the differences in λ_r/λ_d for each aperture width become less, with each ratio appearing to decrease toward one. For the widest two apertures, the spectral resonance characteristic is no longer present, and hence, the assignment of a “resonance wavelength” is questionable.

Up to this point, we have discussed the optical response of a free standing slot array mesh to only the TE polarization. Each mesh geometry is accompanied by a unique optical response for the TM polarization also. Figure 15 shows the transmissivities for incident TM polarization for

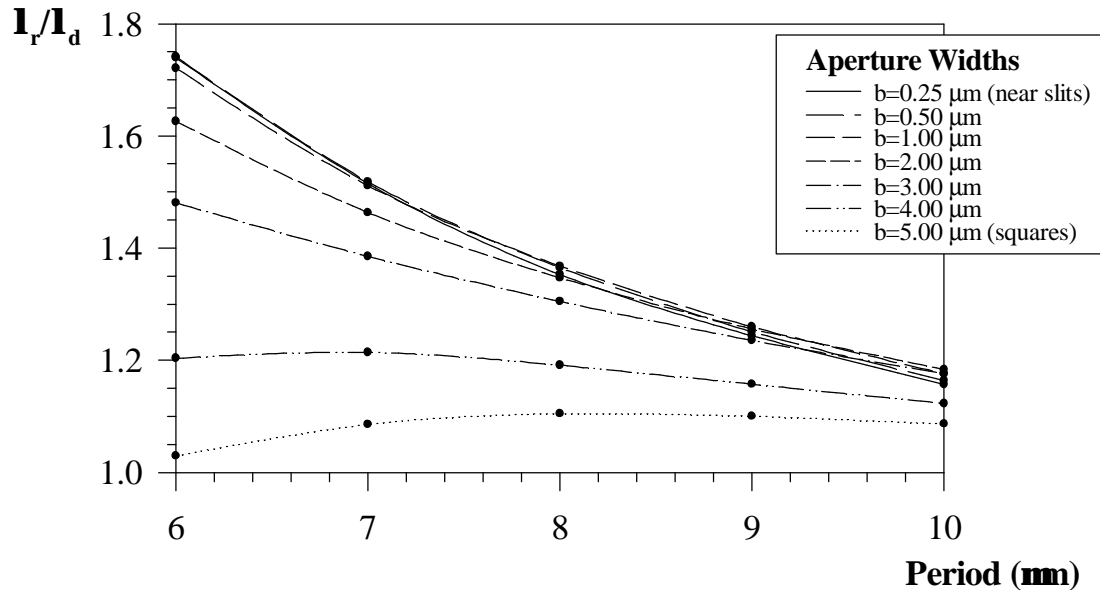


Figure 14 - Ratio of λ_r to λ_d as a function of period for the data presented in Figure 4. Aperture widths vary from $0.25\mu\text{m}$ (near slits) to $5.0\mu\text{m}$ (squares).

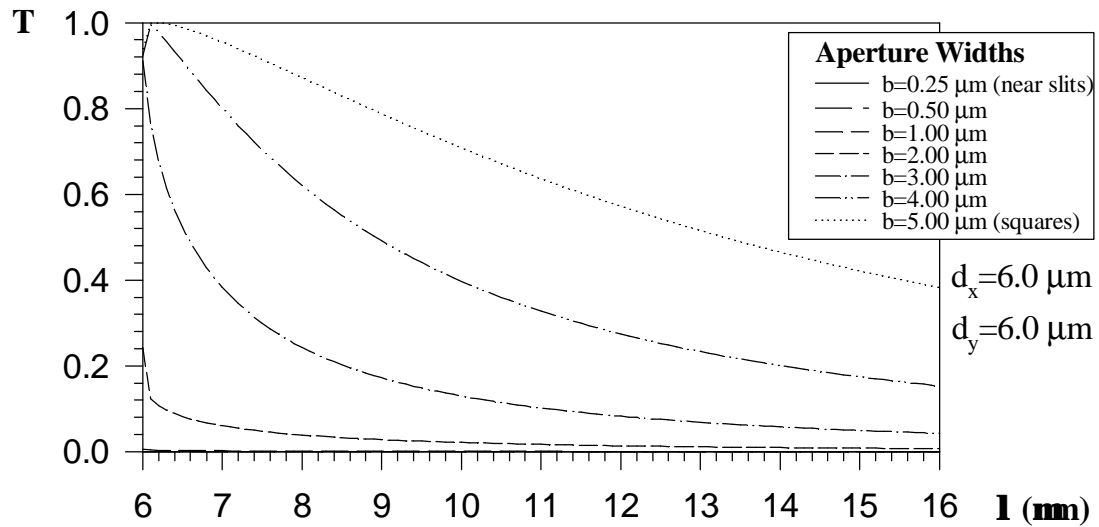


Figure 15 -Transmission profiles for FSSs consisting of a free-standing rectangular array of rectangular apertures of varying width and a constant length ($5.0\mu\text{m}$). Periodicity of the array is systematically varied equally in the x and y directions ($d_x = d_y$). Polarization is TM.

the same mesh geometries as those considered in figure 13. Upon comparison of figures 13 and 15 it is apparent that the transmissivities are the same when the apertures are square, a result that is expected based on symmetry. However the transmissivities for TE and TM polarizations differ dramatically for all other aperture shapes. For the TM polarization, there is no resonance character at all to the spectral response; instead the transmissivity monotonically decreases with wavelength for all wavelengths that are slightly greater than the diffraction edge.

One also observes that the transmissivity decreases at all wavelengths with decreasing slot width. Inspection of the legend in figure 15 indicates that there are seven plots on the graph, with only four appearing distinctly. These four correspond to the four widest apertures, specifically those whose widths are $5.0\mu\text{m}$, $4.0\mu\text{m}$, $3.0\mu\text{m}$, and $2.0\mu\text{m}$. Those apertures whose widths are $1.0\mu\text{m}$ or less have transmissivities that are negligibly small. To a TM polarized incident wave, these aperture arrays are essentially invisible! This can be explained by considering first the limiting case of a zero width aperture array. In this case the aperture plane is a uniform, perfectly con-

ducting surface. The incident electric field produces current flow on the metal surface that is uniform everywhere and in the direction of the incident field. When very narrow slots are “cut” in the metal such that their long dimension coincides with the incident electric field direction, a *slight* modification to the current path is created. This modification to the current flow is enhanced with increasing slot width. For the very narrowest of slots, the change in current path is sufficiently small so as to be indistinguishable from an otherwise uniformly conducting metallic surface. For the wider slots, the current is forced to circulate around the apertures in more pronounced manner, thus creating an array of magnetic dipole moments at each slot location. The association of a magnetic phenomenon with this type of array is the basis for referring to it as an “inductive” array.

3.3.2 Unequal Periods in x and y directions

We now discuss the results of varying the period in one direction only. In the first part of this study, the period in the x direction was held constant at $6.0\mu\text{m}$ while the period in the y direction was varied from $6.0\mu\text{m}$ to $10.0\mu\text{m}$. In the second part, the period in the y direction was held constant at $6.0\mu\text{m}$ while the period in the x direction was varied from $6.0\mu\text{m}$ to $10.0\mu\text{m}$. The same aperture length (a constant $5.0\mu\text{m}$ in the y direction) and width combinations described previously were used in this study.

Figure 16 shows the transmissivity profiles for various aperture aspect ratios if the period in the y direction is varied. The top graph is the same as that of figure 13 for the case of apertures separated by an equal $6.0\mu\text{m}$ period in both the x and y directions. The center and lower graphs show the profiles for $8.0\mu\text{m}$ and $10.0\mu\text{m}$ periods, respectively.

Comparing figure 16 to figure 13, we observe several trends resulting from changing the period in the y direction (d_y) only. As in the case of changing the period equally in both directions (figure 13), the bandwidth decreases for a given aspect ratio as d_y increases. For example, compare the case when $b = 0.25\mu\text{m}$, and $d_y = 6.0\mu\text{m}$, $8.0\mu\text{m}$, and $10.0\mu\text{m}$ (the solid lines in each of the plots in figure 16). Clearly, the bandwidth decreases as d_y increases. The same holds true for any other aspect ratio. However, the bandwidth does not decrease as much when only d_y increases compared to increasing both d_x and d_y . (Compare the middle set of plots in figure 13 to the middle set in figure 16. Then examine the two bottom sets of plots.) Similar to the case of increasing the period in both d_x and d_y , λ_r shifts to a longer wavelength for a given aspect ratio as d_y increases.

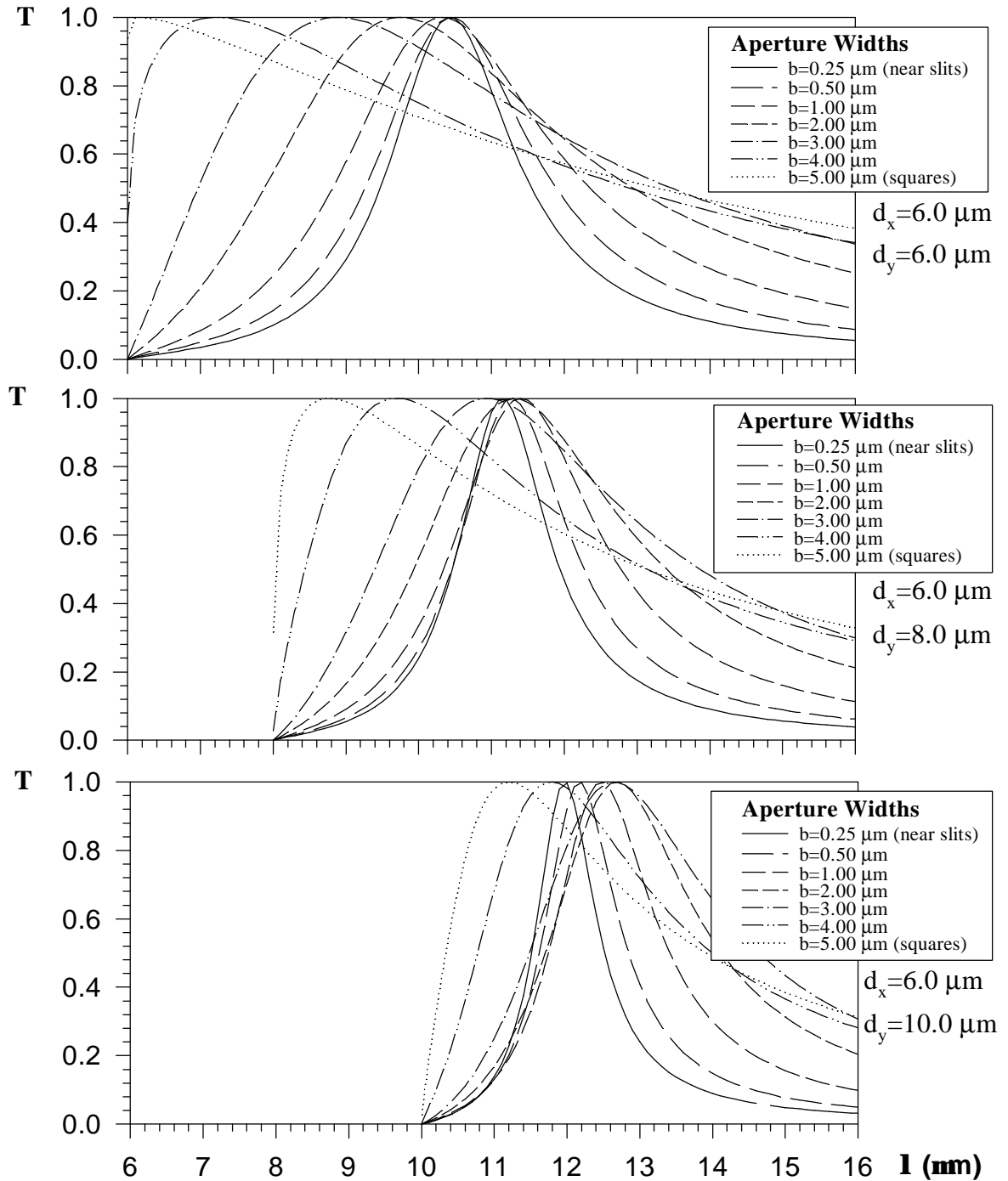


Figure 16 - TE transmission profiles for FSSs consisting of a free-standing rectangular array of rectangular apertures of varying width and a constant length ($5.0 \mu\text{m}$). Periodicity of the array is systematically varied only in the y direction (d_y), while $d_x = 6.0 \mu\text{m}$ is held constant.

Also, as the aspect ratio decreases (going from near slits to square apertures), λ_r initially increases, then decreases. The exception, as noted previously, is the case when $d_x = d_y = 6.0\mu\text{m}$, when λ_r always decreases as the aspect ratio decreases. Finally, the last observation, from figure 16, concerns how λ_r shifts when the aspect ratio changes for a particular period. When only d_y changes, the range of λ_r is greater than when both d_x and d_y change equally. (Compare the bottom set of plots in figure 13 to the bottom set in figure 16.) In the bottom set of plots in figure 16, λ_r varies more than $1.5\mu\text{m}$ while in the bottom set in figure 13, it varies less than $1.0\mu\text{m}$.

Figure 17 demonstrates the effect of changing the period in the x direction (d_x) only and also provides several interesting observations. A first observation is that the bandwidth for a given aspect ratio decreases as d_x is increased in a manner similar to the cases shown in figure 13. A second observation that concerns the shift in resonance wavelength is significantly different from that observed when both d_x and d_y are increased equally (figure 13) or when only d_y is increased (figure 16). Specifically, the shift in λ_r is significantly less if only the period in the x direction is varied. In fact, for $b = 0.25\mu\text{m}$, increasing the period in the x direction has little effect on the resonance wavelength, which remains nearly fixed at $10.4\mu\text{m}$. However, since the diffraction edge ($\lambda_d = d_x$ in this case) increases, the resulting curves acquire a “chopped off” appearance at the shorter wavelengths. This combined effect prevents the occurrence of a resonance peak for many of the aperture widths.

Two conclusions can be drawn from the observations in figures 16 and 17. First, increasing either d_x or d_y has the effect of decreasing the bandwidth for a particular aspect ratio. Second, varying d_y has significantly more effect on λ_r than varying d_x for the TE polarization and array geometry described in figure 12.

Investigations, such as these, that systematically vary the aspect ratio of rectangular apertures, and the periodicity of the apertures within the array, provide insight as to the manner in which the transmission profile is affected by changes in array geometry. The next step, which is not considered in this report, is to find a quantitative relationship between aperture dimensions, periodicity, and the transmission profile of a FSS.

3.4 Multiple Apertures per Periodic Cell

This section is an excerpt from a recently submitted journal paper, “Frequency Selective

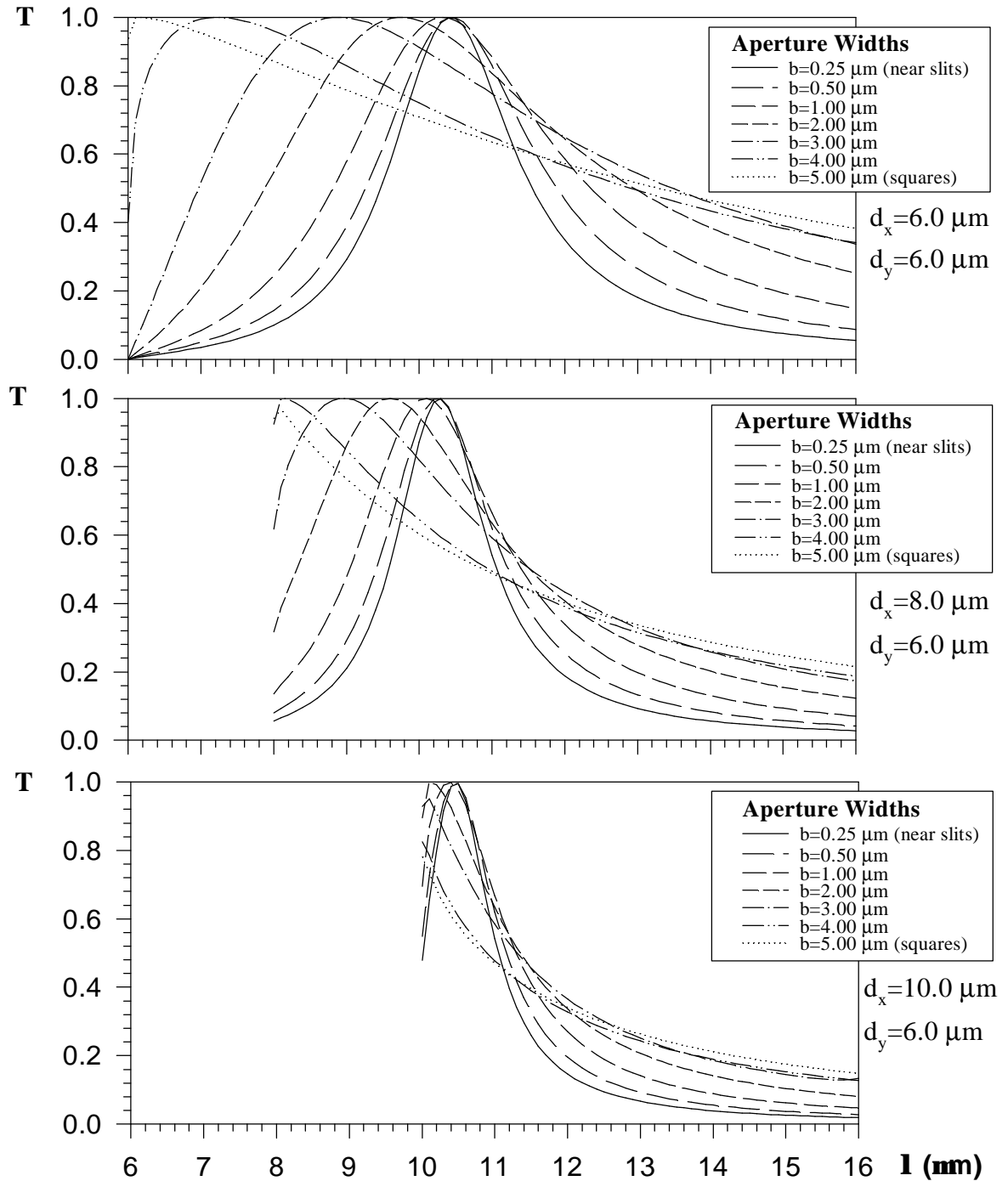


Figure 17 - TE transmission profiles for FSSs consisting of a free-standing rectangular array of rectangular apertures of varying width and a constant length ($5.0 \mu\text{m}$). Periodicity of the array is systematically varied only in the x direction (d_x), while $d_y = 6.0 \mu\text{m}$ is held constant.

Surfaces with Multiple Apertures within a Periodic Cell”, coauthored with Dale M. Byrne. This section includes the main results from that paper. The figures have been renumbered to conform with this text.

3.4.1 Baseline Comparison Case

Our basic goal was to model the spectral and polarization characteristics of frequency selective surfaces consisting of groups of non-similar apertures arranged in a periodic fashion. Narrow rectangular apertures were chosen as a starting point, since these have been shown to exhibit relatively narrow bandpass characteristics that are polarization dependent. The baseline filter geometry used for all comparisons is shown in figure 18. This filter consisted of an infinitely thin, perfectly conducting surface, perforated by $5.0 \times 0.5 \mu\text{m}$ rectangular apertures. The apertures were arranged periodically with a spacing of $6.0 \mu\text{m}$ in both the x and y direction. For a rectangular array, the element spacing is often referred to as the “diffraction edge” since all diffracted orders are evanescent except for the zero or specular order for wavelengths larger than this value. A normally incident plane wave was considered impinging upon the surface and the resulting transmission profile was calculated. In this paper TE polarization refers to the case where the

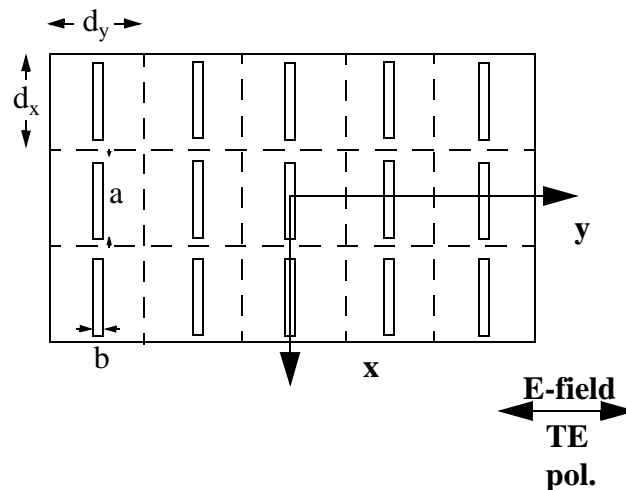


Figure 18 - FSS geometry used as the baseline configuration. In this example $d_x = d_y = 6.0 \mu\text{m}$, $a = 5.0 \mu\text{m}$, and $b = 0.5 \mu\text{m}$.

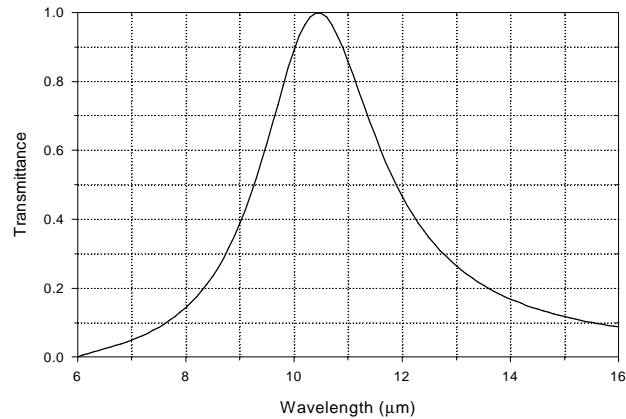


Figure 19 - Zeroth order transmission spectral profile for the baseline configuration of figure 18.

electric field is perpendicular to the long dimension of the aperture. As shown in figure 19, the baseline example produces a bandpass transmission profile. This profile is typical for the case of TE polarization and illustrates the concept that for wavelengths larger than the element spacing, the spectral characteristic is determined to a large extent by the aperture shape. The slot aperture has been shown to produce a transmission bandpass, with the wavelength of peak transmission approximately equal to 2.1 times the slot length³² (when the filter is in air).

3.4.2 Varying Aperture Length in Alternating Columns

Our first modification to the baseline geometry shown in figure 19 consisted of rectangular apertures in which the longer dimension differed for slots in alternate columns. The rationale for this geometry is that since an array of identical slots produces a transmission profile that is dependent on the slot length, combining two arrays of differing slot lengths might produce a transmission profile with a dual bandpass feature. Figure 20 shows this filter layout. In all of our numerical computations, the aperture dimensions $a_1=5.0 \mu\text{m}$, and $b_1=b_2=0.5 \mu\text{m}$ remained constant. We considered aperture lengths for the shorter apertures in the range between $a_2=4.0 \mu\text{m}$,

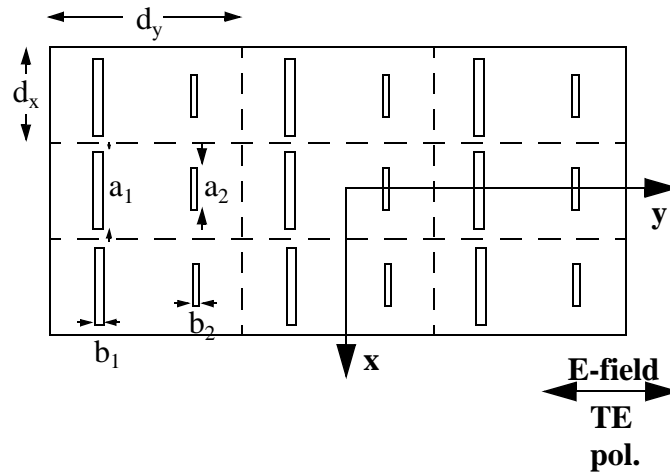


Figure 20 - Geometry used for FSS consisting of a rectangular array of two different apertures per periodic cell (columns of long slots alternate with columns of short slots). The short slot apertures ranged in length from $a_2 = 4.0 \mu\text{m}$ to $a_2 = 5.0 \mu\text{m}$ ($b_2 = 0.5 \mu\text{m}$). The long slot apertures were constant at $a_1 = 5.0 \mu\text{m}$ and $b_1 = 0.5 \mu\text{m}$ while the periodicity was $d_x = 6.0 \mu\text{m}$ and $d_y = 12.0 \mu\text{m}$.

and $a_2 = 5.0 \mu\text{m}$ in $0.25 \mu\text{m}$ increments. Note that when $a_2 = 5.0 \mu\text{m}$, the geometry is identical to the original baseline geometry. Although individual apertures were still separated by $6.0 \mu\text{m}$, the group periodicity in the y -direction, d_y , became $12.0 \mu\text{m}$ and each periodic cell now consisted of two apertures instead of one as in the baseline case. Again we considered a normally incident plane wave with TE polarization.

The resulting transmission profiles are presented in figure 21. The resulting profiles differ dramatically from our baseline profile (the solid line in figure 21). Instead of a single resonance peak, the new profiles exhibit a dual resonance, consisting of a broad peak with a bandwidth (full width at half maximum) on the order of $2 \mu\text{m}$, and a narrow peak with a bandwidth on the order of $0.2 \mu\text{m}$. The broad resonance bandwidth increases from $2.2 \mu\text{m}$ to $3.0 \mu\text{m}$ as a_2 increases from 4.0 to $5.0 \mu\text{m}$. Also, as a_2 increases from 4.0 to $5.0 \mu\text{m}$, the wavelength of maximum transmission of the broad resonance increases from about $9.3 \mu\text{m}$ to $10.4 \mu\text{m}$ while its maximum transmittance value increases from 0.63 to 1.0 . Since the periodicity in the y -direction is $12.0 \mu\text{m}$, orders other

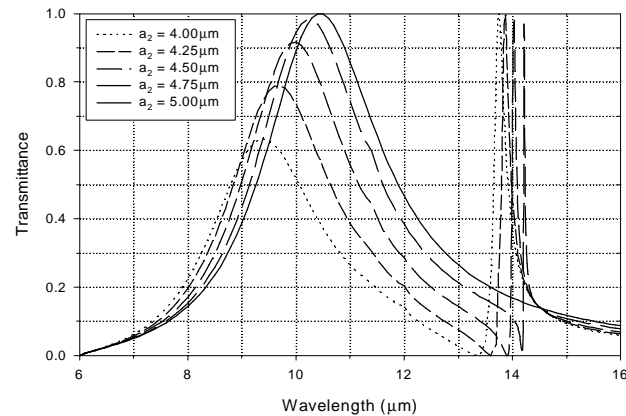


Figure 21 - Zeroth order transmission spectral profile for the baseline configuration of figure 20.

than the specular order are propagating in the far field for wavelengths less than $12.0 \mu\text{m}$. We note that since all of the broad resonance peaks occur at wavelengths *less* than $12.0 \mu\text{m}$, the resonant peaks would not be expected to approach a maximum value of 1.0 because some energy propagates in diffracted orders other than the specular order. The lone exception is for $a_2=5.0 \mu\text{m}$, which reverts to our baseline geometry, with a periodicity of $6.0 \mu\text{m}$ in the y -direction. Only the specular order is propagating in the far field for the wavelengths greater than $6.0 \mu\text{m}$ for this configuration. Consequently, the resonance peak is expected to reach a maximum value of 1.0 for this case.

It should be noted that all of the narrow resonance peaks occur at wavelengths greater than $12.0 \mu\text{m}$, where only the specular order is propagating in the far field. In this spectral region, all of the narrow peaks should approach a maximum value of 1.0, which indeed they do. An interesting feature is the decreasing bandwidth that results as a_2 increases from 4.0 to $5.0 \mu\text{m}$. At $a_2=4.0 \mu\text{m}$ the bandwidth is $0.25 \mu\text{m}$, while at $a_2=4.75 \mu\text{m}$, it has decreased to less than $0.03 \mu\text{m}$. Of course, for $a_2=5.0 \mu\text{m}$, our baseline geometry, no narrow peak is present at all. The implication is that as a_2 approaches a_1 for this type of filter geometry, the resulting resonance bandpass increasingly narrows. In addition, the wavelength of maximum transmission shifts monotonically toward

longer wavelengths as a_2 increases. The specific manner in which the bandwidth and spectral location of both resonances vary will be discussed in a subsequent paper. In any case, this feature may prove valuable in the design of a very narrow bandpass filter.

3.4.3 Varying Aperture Length in Alternating Rows

A second modification of the baseline geometry consisted of varying the aperture length in alternating rows as shown in figure 22. Again $a_1 = 5.0 \mu\text{m}$, and $b_1=b_2= 0.5 \mu\text{m}$ was constant throughout all computations, while a_2 was varied as in the previous example from $4.0 \mu\text{m}$ to $5.0 \mu\text{m}$. The periodicity in the y -direction, d_y , is $6.0 \mu\text{m}$, but the cell or group periodicity in the x -direction, d_x , has increased to $12.0 \mu\text{m}$. Again, a periodic cell consists of two apertures. Figure 23

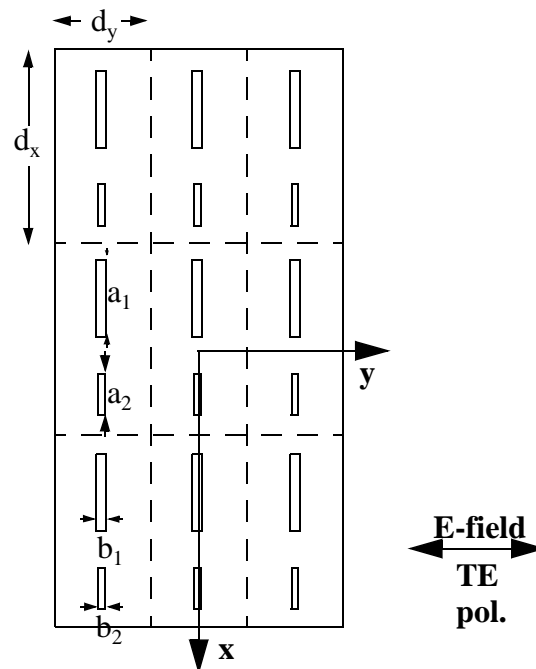


Figure 22 - Geometry used for FSS consisting of a rectangular array of two different apertures per periodic cell (rows of long slots alternate with rows of short slots). The short slot apertures ranged in length from $a_2 = 4.0 \mu\text{m}$ to $a_2 = 5.0 \mu\text{m}$ ($b_2 = 0.5 \mu\text{m}$). The long slot apertures were constant at $a_1 = 5.0 \mu\text{m}$ and $b_1 = 0.5 \mu\text{m}$ while the periodicity was $d_x = 12.0 \mu\text{m}$ and $d_y = 6.0 \mu\text{m}$.

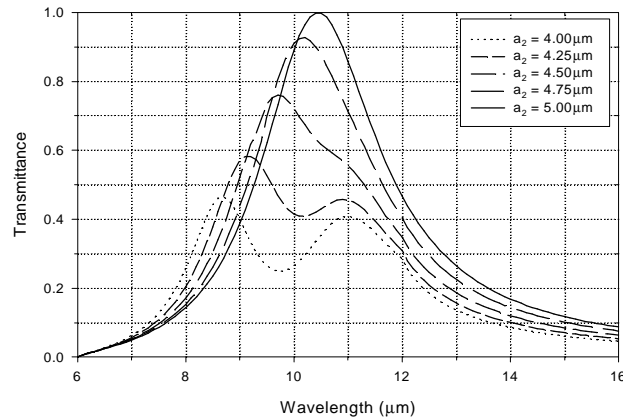


Figure 23 - Zeroth order transmission spectral profile for the baseline configuration of figure 22.

shows the transmission profiles resulting from a normally incident plane wave with TE polarization.

The spectral profiles for this filter geometry are quite different from the baseline geometry and are very different from those in the previously discussed case. No *pronounced* dual resonance peaks are observed. In fact, no resonance peaks occur at all for wavelengths greater than $12.0 \mu\text{m}$ (the wavelength region where only the specular order is propagating in the far field). Several of the profiles have minor dips in the wavelength range from $6.0 \mu\text{m}$ to $12.0 \mu\text{m}$, but overall, there are no dramatic resonant type characteristics that might be exploited in a bandpass filter design. On the other hand, one could consider the bandwidth of the passband to be widened. Further study needs to occur to determine if there are ways to smoothen the “within-band” transmissivity and/or sharpen the fall-off.

3.4.4 Varying Aperture Length in Alternating Rows and Columns

We next investigated the effect of varying the aperture length in alternating rows and alternating columns to create the mesh geometry shown in figure 24. This particular geometry requires the periodic group to have two member apertures arranged in a triangular array. In this arrangement the periodicity is $12.0 \mu\text{m}$ along the x axis and $6.0 \mu\text{m}$ along the y axis. However, the period-

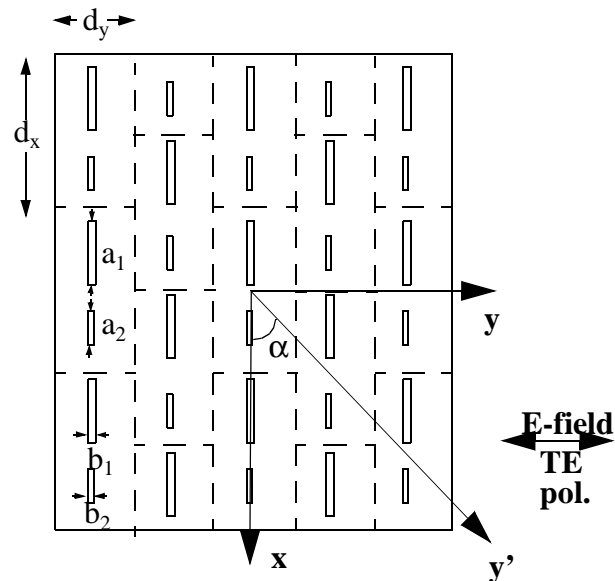


Figure 24 - Geometry used for FSS consisting of a triangular array of two different apertures per periodic cell (long slots alternate with short slots). The short slot apertures ranged in length from $a_2 = 0.5 \mu\text{m}$ to $a_2 = 5.0 \mu\text{m}$ ($b_2 = 0.5 \mu\text{m}$). The long slot apertures were constant at $a_1 = 5.0 \mu\text{m}$ and $b_1 = 0.5 \mu\text{m}$ while the periodicity was $d_x = 12.0 \mu\text{m}$, $d_y = 6.0 \mu\text{m}$, and $\alpha = 45^\circ$.

icity of $6\sqrt{2} \mu\text{m}$ along the skewed axis y' defines the diffraction edge λ_d . The normally incident plane wave is again assumed to be TE polarized. As with the previous two examples, the long slot is held constant with dimensions $a_1 = 5.0 \mu\text{m}$, $b_1 = 0.5 \mu\text{m}$. The short slot has $b_2 = 0.5 \mu\text{m}$, also held constant, while a_2 is incremented from 0.5 to 5.0 μm . Note that when $a_2 = 5.0 \mu\text{m}$ all slots are identical, and the array is the baseline configuration depicted in figure 18. For clarity, the spectral profiles are separated into two figures. The spectral profiles shown in figure 25 result from the mesh geometries in which the short slot dimensions lie between $a_2 = 0.5 \mu\text{m}$ and $a_2 = 3.5 \mu\text{m}$, while the spectral profiles shown in figure 26 result from geometries in which the short slot dimensions between $a_2 = 3.75 \mu\text{m}$ and $a_2 = 5.0 \mu\text{m}$.

The profiles in figure 25 show a single resonance peak located near 10.9 μm for all of the cases of a_2 between 0.5 μm and 3.50 μm . In addition each curve exhibits a transmission peak at a wavelength just short of the diffraction edge wavelength of $\lambda_d = 6\sqrt{2} \mu\text{m}$. This resonance peak

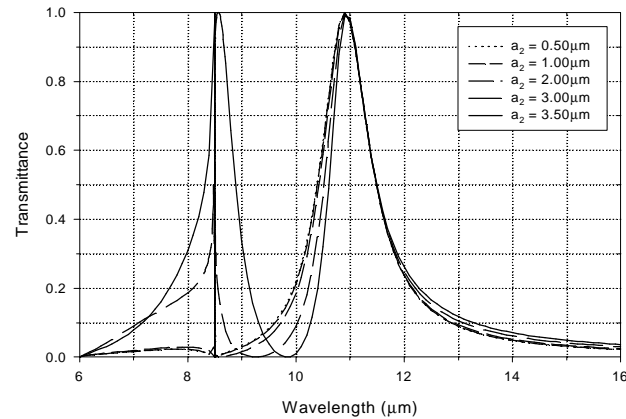


Figure 25 - Zeroth order transmission spectral profiles for figure 24 with the short slot apertures ranging in length from $a_2 = 0.5 \mu\text{m}$ to $a_2 = 3.5 \mu\text{m}$ ($b_2 = 0.5 \mu\text{m}$). The long slot apertures were constant at $a_1 = 5.0 \mu\text{m}$ and $b_1 = 0.5 \mu\text{m}$.

is the familiar Wood's anomaly reported frequently in the literature.^{19,20,21,33,34,35,36,37} Although not clearly depicted in figure 25, rapid variations (as a function of wavelength) due to Wood's anomalies do occur for the case of $a_2 = 3.50 \mu\text{m}$ when inspected in finer detail for wavelengths near $6\sqrt{2} \mu\text{m}$.

All of the spectral profiles in figure 26 exhibit a dual resonance nature. As a_2 is varied from $3.75 \mu\text{m}$ to $4.50 \mu\text{m}$ the shorter wavelength resonant peak shifts from $8.8 \mu\text{m}$ to $10.1 \mu\text{m}$, while the second resonant peak shifts very slightly between $11.0 \mu\text{m}$ and $11.1 \mu\text{m}$. It should also be noted that no classical Wood's anomalies are observed for these cases of a_2 between $3.75 \mu\text{m}$ and $5.00 \mu\text{m}$.

3.5 Outline of Remaining Research

This final section will detail the remaining work necessary to complete this dissertation. Several more computer runs with various aperture/patch geometries are necessary to better understand the dynamics of varying periodicity and aperture/patch dimensions, especially with the

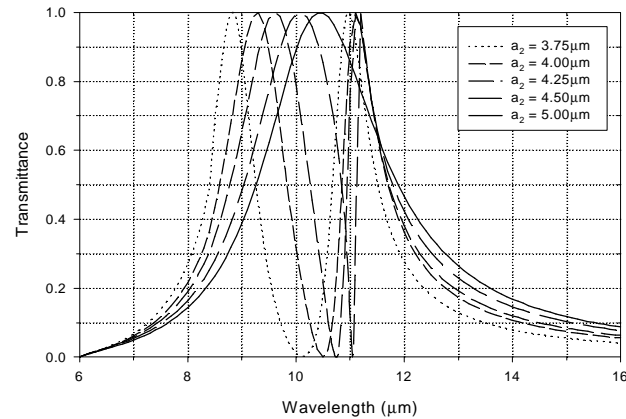


Figure 26 - Zeroth order transmission spectral profiles for figure 24 with the short slot apertures ranging in length from $a_2 = 3.75 \mu\text{m}$ to $a_2 = 5.0 \mu\text{m}$ ($b_2 = 0.5 \mu\text{m}$). The long slot apertures were constant at $a_1 = 5.0 \mu\text{m}$ and $b_1 = 0.5 \mu\text{m}$. The dual resonance nature of the FSS is clearly evident in this figure.

addition of dielectric substrates. While the effects of having two apertures per periodic cell has been investigated, the next step of extending the process to more than two apertures per periodic cell needs to be taken. Also varying aperture dimensions, plus using circular apertures needs to be considered. Finally, the some cases of multiple patches per periodic cell (especially on a substrate) will have to be studied.

Within this investigation of multiple apertures/patches per periodic cell, the effects of Wood's anomalies on the resulting spectral profiles must be better understood. This is especially important since the diffraction edge, and thus Wood's anomalies, often cannot be ignored in the spectral profiles for these types of FSSs. Once these final remaining areas of research are completed, writing the remaining chapters of the dissertation is all that is left to complete.

Appendix A: Derivation of the FSS Matrix Equation

For the general case of a thin, planar, perfectly conducting FSS with its periodic cells arranged in a triangular geometry as shown in figure 27, it will be necessary to modify the derivation of the FSS matrix equation given by Chen^{3,4,5} to apply to the model described in figure 28. To simplify the comparison to Chen's work, the notation in his papers has been retained. The periodicity for the triangular array depicted in figure 27 exists along the skewed set of axes x' and y' .

As Chen pointed out, the electromagnetic fields near the FSS must satisfy the periodicity requirements imposed by Floquet's theorem. Thus the scalar modal potential, assuming an $\exp(j\omega t)$ time dependence, will be

$$\Psi_{pq} = \exp(-j(u_{pq}x + v_{pq}y + \gamma_{pq}z)) \quad (\text{A.1})$$

where

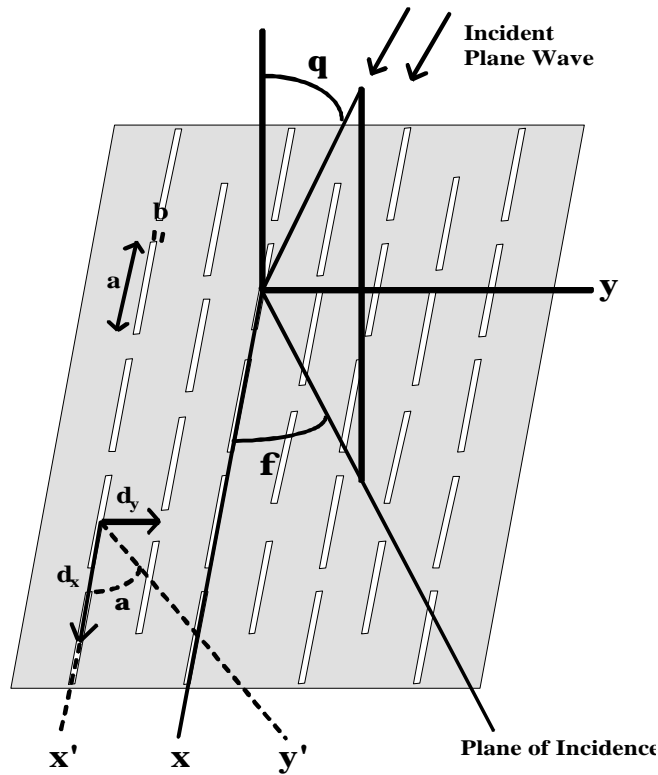


Figure 27 - Geometry for a FSS with a triangular array

$$u_{pq} = k \sin \theta \cos \phi + \frac{2\pi p}{d_x} \quad (\text{A.2})$$

$$v_{pq} = k \sin \theta \sin \phi + \frac{2\pi q}{d_y} - \frac{2\pi p}{d_x \tan \alpha} \quad (\text{A.3})$$

$$\text{for } p, q = 0, \pm 1, \pm 2, \dots, \pm \infty \quad (\text{A.4})$$

$$\gamma_{pq} = \sqrt{k^2 - t_{pq}^2}, \quad \text{for } k^2 > t_{pq}^2 \quad (\text{A.5})$$

$$\gamma_{pq} = -j\sqrt{t_{pq}^2 - k^2}, \quad \text{for } k^2 < t_{pq}^2 \quad (\text{A.6})$$

with

$$t_{pq}^2 = u_{pq}^2 + v_{pq}^2. \quad (\text{A.7})$$

Note in equation (A.3) that if α approaches the limit of 90° , the above equations now correspond to a rectangular array geometry.

From the scalar mode potential, Chen derived the vector orthonormal mode functions for the transverse electric field. Using the convention of transverse electric (TE) and transverse magnetic (TM) polarizations, the vector orthonormal Floquet mode functions in Cartesian coordinates are

$$\vec{\Phi}_{pq}^{TE} = \frac{1}{\sqrt{d_x d_y}} \left(\frac{v_{pq}}{t_{pq}} \hat{x} - \frac{u_{pq}}{t_{pq}} \hat{y} \right) \psi_{pq} \quad (\text{A.8})$$

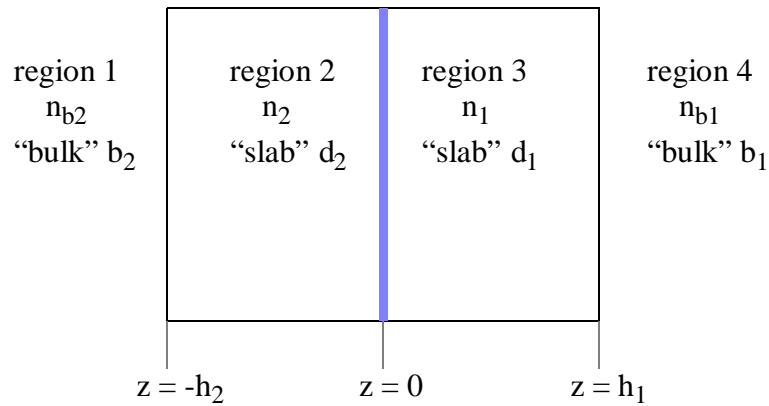


Figure 28 - Substrate model of FSS

$$\vec{\Phi}_{pq}^{TM} = \frac{1}{\sqrt{d_x d_y}} \left(\frac{u_{pq}}{t_{pq}} \hat{x} + \frac{u_{pq}}{t_{pq}} \hat{y} \right) \Psi_{pq}. \quad (\text{A.9})$$

The transverse electric field in any region of space can then be written as a linear combination of the above Floquet modes.

For an electromagnetic wave satisfying the requirements,

$$\left(\frac{\lambda_0}{d_x} \right)^2 + \left(\frac{\lambda_0}{2d_y} \right)^2 \geq (1 + \sin \theta)^2 \quad (\text{A.10})$$

and

$$2 \left(\frac{\lambda_0}{d_x} \right) \left(\frac{\lambda_0}{d_y} \right) \geq (1 + \sin \theta) \quad (\text{A.11})$$

(where λ_0 is the wavelength), only the TE and TM modes with $p=q=0$ propagate in the far field. An incident plane wave may be written as

$$\vec{E}_t^{(inc)} = \sum_{r=1}^2 A_{00r} \vec{\Phi}_{00r}^{(inc)} \quad (\text{A.12})$$

where $r=1$ refers to the TE mode, $r=2$ to the TM mode, and the superscript indicates that the wave number, k , is in the incident side medium. The transmitted field is then written as

$$\vec{E}_t^{(trans)} = \sum_p \sum_q \sum_{r=1}^2 B_{pqr} \vec{\Phi}_{pqr}^{(trans)} \quad (\text{A.13})$$

where B_{pqr} are the unknown transmission coefficients, and the superscript indicates that the wave number, k , is in the transmission side medium. Similarly, the reflected field is given by

$$\vec{E}_t^{(refl)} = \sum_p \sum_q \sum_{r=1}^2 R_{pqr} \vec{\Phi}_{pqr}^{(refl)} \quad (\text{A.14})$$

where R_{pqr} are the unknown reflection coefficients.

Using the modal admittance functions

$$\xi_{pq1}^{(i)} = \left(\frac{\gamma_{pq}^{(i)}}{k_0} \right) Y_0 \quad (\text{A.15})$$

$$\xi_{pr2}^{(i)} = \left(\frac{k_0}{\gamma_{pq}^{(i)}} \right) n_i^2 Y_0, \quad (\text{A.16})$$

(where k_0 is the magnitude of the free space propagation vector, Y_0 the free space admittance, and the superscript indexes the medium), one may also write the transverse magnetic field in terms of the vector Floquet modes:

$$-\hat{z} \times \vec{H}_t^{(inc)} = \sum_{r=1}^2 A_{00r} \xi_{00r}^{(inc)} \bar{\Phi}_{00r}^{(inc)} \quad (\text{A.17})$$

$$-\hat{z} \times \vec{H}_t^{(trans)} = \sum_p \sum_q \sum_{r=1}^2 B_{pqr} \xi_{pqr}^{(trans)} \bar{\Phi}_{pqr}^{(trans)} \quad (\text{A.18})$$

$$-\hat{z} \times \vec{H}_t^{(refl)} = \sum_p \sum_q \sum_{r=1}^2 (-R_{pqr}) \xi_{pqr}^{(refl)} \bar{\Phi}_{pqr}^{(refl)}. \quad (\text{A.19})$$

At this point it becomes necessary to slightly modify Chen's work to describe the model in figure 28. If one considers a FSS sandwiched between two dielectric substrates, the transverse electric field in region 1 is

$$\vec{E}_t^{(b2)} = \vec{E}_t^{(inc)} + \vec{E}_t^{(refl)} \quad (\text{A.20})$$

while the field in region 4 is

$$\vec{E}_t^{(b1)} = \vec{E}_t^{(trans)}. \quad (\text{A.21})$$

A similar procedure may be followed for \vec{H}_t . In region 2, we simply write the field as a linear combination of the vector Floquet modes for a left and a right traveling wave in region 2. The same applies to region 3.

The field at the FSS boundary can be written as

$$\vec{E}_t^{(FSS)} = \sum_m \sum_n \sum_{l=1}^2 F_{mnl} \bar{\Psi}_{mnl} \quad (\text{A.22})$$

over the apertures for an inductive FSS, and

$$-\hat{z} \times \vec{H}_t^{(FSS)} = \sum_m \sum_n \sum_{l=1}^2 F_{mnl} \bar{\Psi}_{mnl} \quad (\text{A.23})$$

over the patches of a capacitive FSS. The coefficients F_{mnl} are the unknowns we wish to solve for, while $\tilde{\Psi}_{mnl}$ are a set of new basis functions. Since the sum of modal functions is infinite, and numerical methods will require approximation by a finite series, it is desirable to choose the basis functions so that the summation achieves rapid convergence. Since the waveguide modal functions of the apertures for an inductive FSS must satisfy the boundary conditions of the problem, and are a complete orthonormal set, their use as basis functions will provide the necessary rapid convergence. Similarly, for a capacitive FSS, one uses the dual of the waveguide modal functions for apertures of equivalent dimensions to the metal patches in the capacitive FSS.

Matching the boundary conditions between the four regions eliminates all unknowns except the coefficients F_{mnl} , and using the orthogonality property of basis functions results in the matrix equation,

$$\sum_r Y_{00r}^{in} A_{00r} C_{00r}^{*MNL} = \sum_m \sum_n \sum_l F_{mnl} \sum_p \sum_q \sum_r Y_{pqr}^{(eff)} C_{pqr}^{mnl} C_{pqr}^{*MNL} \quad (\text{A.24})$$

for an inductive FSS sandwiched between two dielectrics of thickness h_1 and h_2 as shown in figure 2, and

$$\sum_r Y_{00r}^{in} Z_{00r}^{eff} A_{00r} C_{00r}^{*MNL} = \sum_m \sum_n \sum_l F_{mnl} \sum_p \sum_q \sum_r Z_{pqr}^{(eff)} C_{pqr}^{mnl} C_{pqr}^{*MNL} \quad (\text{A.25})$$

for a capacitive FSS, where

$$Y_{pqr}^{in} = \frac{2\xi_{pqr}^{b_2} \xi_{pqr}^{d_2} e^{j\gamma_{pq}^{b_2} h_2}}{[\xi_{pqr}^{d_2} \cos(\gamma_{pq}^{d_2} h_2) + j\xi_{pqr}^{b_2} \sin(\gamma_{pq}^{d_2} h_2)]} \quad (\text{A.26})$$

$$Y_{pqr}^{(eff)} = (Z_{pqr}^{(eff)})^{-1} = (Y_{pqr}^{d_1} + Y_{pqr}^{d_2}) \quad (\text{A.27})$$

$$Y_{pqr}^{d_1} = \xi_{pqr}^{d_1} \frac{(\xi_{pqr}^{b_1} + j\xi_{pqr}^{d_1} \tan(\gamma_{pq}^{d_1} h_1))}{\xi_{pqr}^{d_1} + j\xi_{pqr}^{b_1} \tan(\gamma_{pq}^{d_1} h_1)} \quad (\text{A.28})$$

$$Y_{pqr}^{d_2} = \xi_{pqr}^{d_2} \frac{(\xi_{pqr}^{b_2} + j\xi_{pqr}^{d_2} \tan(\gamma_{pq}^{d_2} h_2))}{\xi_{pqr}^{d_2} + j\xi_{pqr}^{b_2} \tan(\gamma_{pq}^{d_2} h_2)}. \quad (\text{A.29})$$

As described by Chen, the coupling coefficients for an inductive FSS,

$$C_{pqr}^{mnl} = \int \int_{aperture} \vec{\Psi}_{mnl} \cdot \vec{\Phi}_{pqr}^* da, \quad (\text{A.30})$$

are integrated over the area of the aperture, where $\vec{\Psi}_{mnl}$ are the waveguide modal functions for the apertures. Similarly, for a capacitive FSS, the coupling coefficients,

$$C_{pqr}^{mnl} = \int \int_{patch} \vec{\Psi}_{mnl} \cdot \vec{\Phi}_{pqr}^* da \quad (\text{A.31})$$

are integrated over the area of the metal patch, where $\vec{\Psi}_{mnl}$ are the dual of the waveguide modal functions for apertures of equivalent dimensions to the metal patches in the capacitive FSS.

The remaining steps are identical to those described by Chen in his papers. Since the above matrix equations (Equations (A.23) and (A.24)) are of the form

$$[I_{MNL}] = [Y_{MNL}^{mnl}][F_{mnl}], \quad (\text{A.32})$$

matrix inversion yields the unknown coefficients F_{mnl} . These coefficients may be used in equation (A.21) to find the transverse electric field in the apertures for an inductive FSS, or in equation (A.22) to find the transverse magnetic field on the patches of a capacitive FSS. More importantly, the reflection and transmission coefficients, R_{pqr} and B_{pqr} , can be found once these transverse fields are known.

In the far field, only the modes $p=q=0$ propagate, so we really are interested in the coefficients R_{00r} and B_{00r} (where $r=1,2$ are the TE, TM polarizations, respectively). In this paper, we will consider the reflectance and transmittance relative to the incident medium (with index n_{b2}),

$$\mathfrak{R}_{00r} = |R_{00r}|^2 \quad (\text{A.33})$$

and

$$T_{00r} = \frac{n_{b1}}{n_{b2}} \cdot |B_{00r}|^2. \quad (\text{A.34})$$

Appendix B: Extending Chen's Method to Multiple Apertures/ Patches per Periodic Cell

Chen's modal method^{3,4,5} is well suited to rectangular apertures/patches, with the basis functions used to expand the field in each aperture being rectangular waveguide modal functions. All resulting coefficient integrals can then be expressed in closed form, speeding up numerical computation considerably.

Chen's method makes use of the fact that the periodic aperture geometry imposes a periodicity on the scattered wave fields near the filter surface. To model this periodicity the incident, reflected, and transmitted transverse electric fields are expanded in terms of Floquet modes, $\bar{\Phi}$, with unknown reflection and transmission coefficients, R and B included in the formulation. By using modal orthogonality, Chen solved for the unknown coefficients representing the amplitudes of the Floquet modes in terms of an integral relation of the unknown field and each Floquet mode. Substituting the integral relation for the coefficients R and B , Chen obtained an integral equation for the unknown field distribution. Starting with this integral equation, we began our modifications to extend Chen's method to *periodic groups* of apertures based on a similar approach by Amitay, Galindo, and Wu¹.

Our analysis applies to the idealized case of a perfectly conducting, infinitely thin metal filter perforated with identical groups of N apertures as shown in figure 29. Each group constitutes a *periodic cell* within the filter. While each group is identical and arranged in a periodic fashion, each member aperture of the group need not be identical. The field in each aperture is expanded in a set of vector orthonormal functions, $\bar{\Psi}$, satisfying the aperture boundary conditions. The set of $\bar{\Psi}'_s$ are the standard waveguide modes suitable for a waveguide having the cross sectional shape

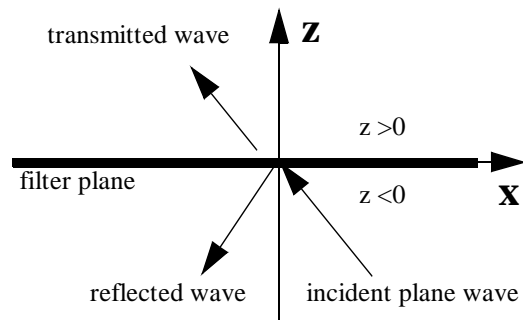
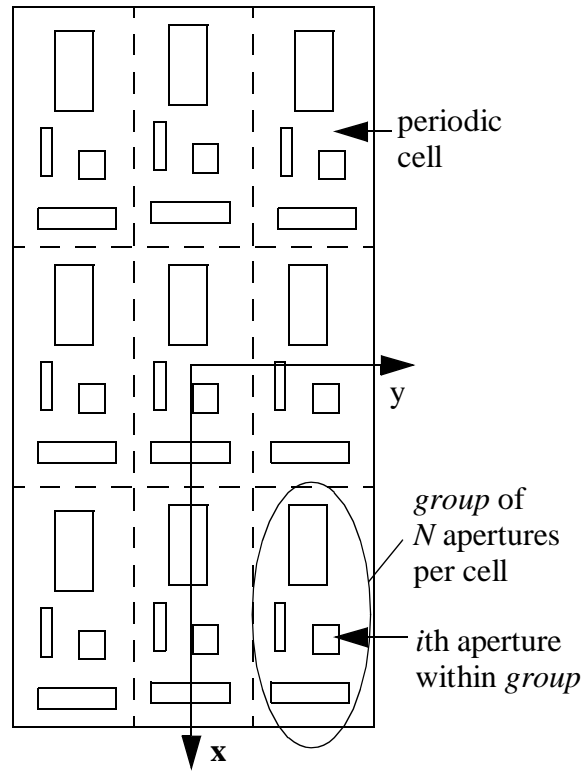


Figure 29 - Typical geometric configuration for a FSS with multiple apertures within a periodic cell.

of the aperture. Using the notation of Chen³, the waveguide expansion of the transverse electric field at the surface of the filter ($z=0$), contributed by the apertures is

$$\bar{E}_t = \sum_{i=1}^N \bar{E}_t^{(i)} = \sum_{i=1}^N \sum_{l=1}^2 \sum_m \sum_n F_{mnl}^{(i)} \bar{\Psi}_{mnl}^{(i)}, \quad (\text{B.1})$$

where the superscript i denotes the i th type of aperture within a group, and the subscripts m, n, l denote the mn -expansion mode for TE polarization ($l=1$), or TM polarization ($l=2$).

For the case of a single aperture per periodic cell ($N=1$), the integral equation (which must be satisfied over the aperture only), as derived by Chen³ (equation 13), is

$$2 \sum_{r=1}^2 A_{00r} \xi_{00r} \bar{\Phi}_{00r} = \sum_p \sum_q \sum_{r=1}^2 (\xi_{pqr} + Y_{pqr}) \bar{\Phi}_{pqr} \int_{\text{aperture}} \bar{E}_t \cdot \bar{\Phi}_{pqr}^* da, \quad (\text{B.2})$$

where A is the incident plane wave expansion coefficient, ξ is the modal admittance, Y is the modal admittance of a dielectric substrate if present ($Y=\xi$ for no substrate), and $\bar{\Phi}_{pqr}$ is the vector pq -Floquet mode for the TE polarization ($r=1$) or TM polarization ($r=2$) in the free space region ($z<0$). It should be noted that the integral in equation (B.2) is over the entire unit cell. However, since $\bar{E}_t = 0$ on the metal surface for a perfect conductor, this integral reduces to the requirement that it must be satisfied only over the aperture region. Thus equation (B.2) is also valid for any periodic group of N apertures since at the filter plane there would only be a field within the apertures and no field on the perfect conductor between the apertures within the group.

The derivation of the matrix expression for the unknown coefficients begins by inserting equation (B.1) into equation (B.2). One then multiplies both sides of equation (B.2) by $\bar{\Psi}_{m'n'l}^*$ and integrates over the i th aperture, to obtain the integral equation for the i th aperture within a periodic group of N apertures

$$2 \sum_{r=1}^2 A_{00r} \xi_{00r} C_{00r}^{(i)m'n'l*} = \sum_p \sum_q \sum_{r=1}^2 G_{pqr} C_{pqr}^{(i)m'n'l*} \left[\sum_{j=1}^N \sum_m \sum_n \sum_{l=1}^2 F_{mnl}^{(j)} C_{pqr}^{(j)m'n'l} \right], \quad (\text{B.3})$$

where

$$G_{pqr} = \xi_{pqr} + Y_{pqr}, \quad (\text{B.4})$$

$$C_{pqr}^{(j)m'n'l} = \int_{jth \text{ - aperture}} \bar{\Psi}_{m'n'l}^j \cdot \bar{\Phi}_{pqr}^* da. \quad (\text{B.5})$$

Equation (B.3) generates N systems of linear algebraic equations,

$$2[I_{m'_i n'_i l'_i}^{(i)}] = \sum_{j=1}^N [Y_{m'_i n'_i l'_i}^{(i,j) m_j n_j l_j}] [F_{m_j n_j l_j}^{(j)}], \quad (\text{B.6})$$

which may be combined into one large system of equations, of the general form

$$2[I] = [Y][F]. \quad (\text{B.7})$$

The matrix elements in the above expression are given by

$$Y_{m'_i n'_i l'_i}^{(i,j) m_j n_j l_j} = \sum_p \sum_q \sum_{r=1}^2 G_{pqr} (C_{pqr}^{(i)m'_i n'_i l'_i})^* C_{pqr}^{(j) m_j n_j l_j} \quad (\text{B.8})$$

$$I_{m'_i n'_i l'_i}^{(i)} = \sum_{r=1}^2 A_{00r} \xi_{00r} (C_{00r}^{(i)m'_i n'_i l'_i})^*. \quad (\text{B.9})$$

The resulting matrix equation (B.7) can then be solved for the unknown coefficients F , which from equation (B.1), yield the transverse electric field at the surface of the mesh.

To extend equations (B.8) and (B.9) to the model described by figure 28 (Appendix A), one needs only to replace the modal admittance functions G_{pqr} and ξ_{00r} in these equations with the corresponding functions $Y_{pqr}^{(eff)}$ and Y_{00r}^{in} in equation (A.24) for the case of an inductive mesh. For a capacitive mesh one would replace G_{pqr} and ξ_{00r} with $Z_{pqr}^{(eff)}$ and $Y_{00r}^{in} Z_{00r}^{(eff)}$ in equation (A.25)

Finally, the reflection coefficients R_{pqr} and the transmission coefficients B_{pqr} can be found from the relationship

$$\delta_{0p} \delta_{0q} A_{pqr} + R_{pqr} = B_{pqr} = \sum_{j=1}^N \left[\sum_{m_j} \sum_{n_j} \sum_{l_j} F_{m_j n_j l_j}^{(j)} C_{pqr}^{(j) m_j n_j l_j} \right] \quad (\text{B.10})$$

where δ is the Kronecker delta.

An advantage to this method is that it seems to avoid the problem of series truncation for sets of multiple periodic equations as described by Mittra³⁸. In theory, the modal expansions for the i th aperture $\bar{\Psi}^{(i)}$ are infinite, but for computational reasons, are truncated at a point that provides relative convergence of the resulting reflection and transmission coefficients. For a single aperture per periodic cell, there is only one series to truncate, but for multiple apertures per periodic cell there is an expansion for each of the apertures within the periodic cell that must be truncated. As a result of this “multiple partitioning”, the coefficients R_{pqr} and B_{pqr} could converge to multiple values depending on the choice of truncation points. To confirm that this problem with multiple partitioning was not occurring, we varied the modal expansions between 6 and 14 terms for each of the apertures within a periodic cell and looked at the resulting R_{pqr} and B_{pqr} . For the cases of apertures being in the form of a narrow slot, the coefficients R_{pqr} and B_{pqr} converged relatively smoothly to one value, with a choice of 10 terms for all modal expansions $\bar{\Psi}^{(i)}$ appearing as optimal for relative convergence/computational time considerations.

This method may also be extended to circular apertures by using circular waveguide modes as the expansion functions in equation (1) as in the $N=1$ case described by Chen⁵. Capacitive filters (metal patches as opposed to apertures) can be analyzed by applying the above procedure as described by Chen⁴, Montgomery²⁷, and Dawes, et al²⁸. A program was written in Fortran for a Sun workstation using the above modifications to Chen’s method to analyze a filter consisting of up to $N=4$ different rectangular apertures per periodic cell. Though this paper deals exclusively with rectangular aperture geometries in free space, the program can also analyze filters

with circular apertures, filters on dielectric substrates and/or superstrates, as well as the equivalent capacitive filters in a variety of configurations.

Bibliography

1. N. Amitay, V. Galindo, and C. P. Wu, *Theory and Analysis of Phased Array Antennas* (Wiley-Interscience, New York, 1972).
2. T. K. Wu, ed., *Frequency Selective Surface and Grid Array* (John Wiley & Sons, New York, 1995).
3. C. C. Chen, "Transmission Through a Conducting Screen Perforated Periodically with Apertures", *IEEE Trans. Microwave Theory Tech.*, **MTT-18**, 627-632 (1970).
4. C. C. Chen, "Scattering by a Two-Dimensional Periodic Array of Conducting Plates", *IEEE Trans. Antennas Propagat.*, **AP-18**, 660-665 (1970).
5. C. C. Chen, "Diffraction of Electromagnetic Waves by a Conducting Screen Perforated Periodically with Circular Holes", *IEEE Trans. Microwave Theory Tech.*, **MTT-19**, 475-481 (1971).
6. B. A. Munk, R. J. Leubers, and R. D. Fulton, "Transmission Through a Two-Layer Array of Loaded Slots", *IEEE Trans. Antennas Propagat.*, **AP-22**, 5804-809 (1974).
7. F. S. Johansson, "Analysis and Design of Double-Layered Frequency Selective Surfaces", *IEE Proc., Pt. H*, **132**, 319-325 (1985).
8. T. Cwik, and R. Mittra, "The Cascade Connection of Planar Periodic Surfaces and Lossy Dielectric Layers to Form an Arbitrary Periodic Screen", *IEEE Trans. Antennas Propagat.*, **AP-35**, 1397-1405 (1987).
9. C. G. Christodoulou, D. P. Kwan, R. Middleveen, and P. F. Wahid, "Scattering from Stacked Gratings and Dielectrics for Various Angles of Wave Incidence", *IEEE Trans. Antennas Propagat.*, **36**, 1435-1442 (1988).
10. R. C. Hall, R. Mittra, and K. M. Mitzner, "Analysis of Multilayered Periodic Structures Using Generalized Scattering Matrix Theory", *IEEE Trans. Antennas Propagat.*, **36**, 511-517 (1988).
11. J. D. Vacchione, C. H. Chan, and R. Mittra, "Cascade Analysis of Power Distribution in a Multilayered Dielectric/Frequency Selective Surface System", *IEEE AP-S International Symposium Digest*, **2**, 1080-1083, (1989).
12. J. D. Vacchione, and R. Mittra, "A Generalized Scattering Matrix Analysis for Cascading FSS of Different Periodicities", *IEEE AP-S International Symposium Digest*, **1**, 92-95, (1990).

13. J. D. Vacchione, and T. K. Wu, "Analysis of a Dual, Non-Similar, Screen FSS Using Simple Cascading Procedures", *IEEE AP-S International Symposium Digest*, 4, 1779-1782, (1992).
14. J. Shaker, and L. Shafai, "Analysis of Multiresonant Frequency Selective Surfaces", *IEEE AP-S International Symposium Digest*, 3, 1948-1951, (1993).
15. J. D. Vacchione, "Techniques for analyzing planar, periodic, frequency selective surface systems", Ph.D. Dissertation, The University of Illinois at Urbana-Champaign (1990).
16. B. A. Munk and R. J. Luebbers, "Reflection Properties of Two-Layered Dipole Arrays", *IEEE Trans. Antennas Propagat.*, **AP-22**, 766-773 (1974).
17. R. O. Miller, "Studies on the Interaction of Waves with Metal Mesh Filters", Master's Thesis, The University of Texas at Dallas (August 1994).
18. D. Zwillinger, *Handbook of Differential Equations* (Academic Press Inc., Boston, 1989), p. 405.
19. R. W. Wood, "On a Remarkable Case of Uneven Light in a Diffraction Grating", *Phil. Mag.*, **4**, 396-402 (1902).
20. Lord Rayleigh, "Note on the Remarkable Case of Diffraction Spectra Described by Prof. Wood", *Phil. Mag.*, **14**, 60-65 (1907).
21. R. W. Wood, "Diffraction Gratings with Controlled Groove Form and Abnormal Distribution of Intensity", *Phil. Mag.*, **23**, 310-317 (1912).
22. N. Amitay and V. Galindo, "The Analysis of Circular Waveguide Phased Arrays", *Bell System Tech. J.*, **47**, 1903-1931 (1968).
23. R. Ulrich, "Far-Infrared Properties of Metallic Mesh and Its Complementary Structure", *Infrared Physics*, **7**, 37-55 (1967).
24. C. C. Chen, "Transmission of Microwave Through Perforated Flat Plates of Finite Thickness", *IEEE Trans. Microwave Theory Tech.*, **MTT-21**, 1-6 (1973).
25. R. Mittra, C. H. Chan, and T. Cwik, "Techniques for Analyzing Frequency Selective Surfaces - A Review", *IEEE Proc.*, **76**, 1593-1615 (1988).
26. J. P. Montgomery and K. R. Davey, "The Solution of Planar Periodic Structures Using Iterative Methods", *Electromagnetics*, **5**, 209-235 (1985).
27. J. P. Montgomery, "Scattering by an Infinite Periodic Array of Thin Conductors on a Dielectric Sheet", *IEEE Trans. Antennas Propagat.*, **AP-23**, 70-75 (1975).
28. D. H. Dawes, R. C. McPhedran, and L. B. Whitbourn, "Thin Capacitive Meshes on a

- Dielectric Boundary: Theory and Experiment”, *Applied Optics*, **28**, 3498-3510 (1989).
29. R. Orta, P. Savi, and R. Tascone, “A New Class of Frequency Selective Surfaces”, *IEEE AP-S International Symposium Digest*, **4**, 1767-1770, (1992).
 30. T. Schimert, M. Koch, and C. Chan, “Analysis of scattering from frequency-selective surfaces in the infrared”, *J. Opt. Soc. Am. A*, **7**, 1545-1553 (1990).
 31. D. M. Byrne, “Diffractive Infrared Filters Fabricated by Electron-beam Lithography”, *Proceedings of SPIE*, **560**, 70-79 (1985).
 32. S. T. Chase and R. D. Joseph, “Resonant Array Bandpass Filters for the Far Infrared”, *Applied Optics*, **22**, 1775-1779 (1983).
 33. R. W. Wood, “Anomalous Diffraction Gratings”, *Phys. Rev.*, **48**, 928-936 (1935).
 34. A. Hessel and A. A. Oliner, “A New Theory of Wood’s Anomalies on Optical Gratings”, *Applied Optics*, **4**, 1275-1296 (1965).
 35. R. J. Leubers and B. A. Munk, “Some Effects of Dielectric Loading on Periodic Slot Arrays”, *IEEE Trans. Antennas Propagat.*, **AP-26**, 536-542 (1978).
 36. C. H. Palmer, and F. W. Phelps, Jr., “Grating Anomalies as a Local Phenomenon”, *J. Opt. Soc. Am.*, **58**, 1184-1188 (1968).
 37. C. H. Palmer, Jr., “Diffraction Grating Anomalies. II. Coarse Gratings”, *J. Opt. Soc. Am.*, **46**, 50-53 (1956).
 38. R. Mittra, “Relative Convergence of the Solution of a Doubly Infinite Set of Equations”, *J. Research (Radio Science)*, Series D, **67D**, 245-254 (1963).



Frequency Selective Surfaces with Multiple Periodic Elements



Dissertation Proposal

Jeffrey A. Reed

Physics Department

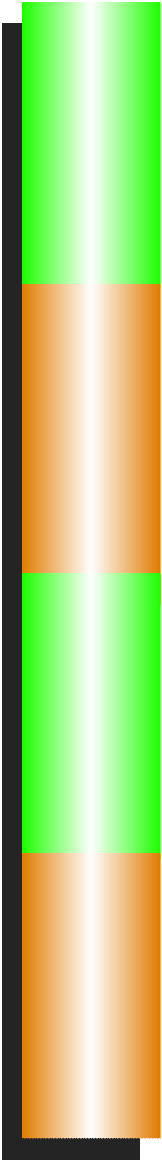
School of Natural Sciences and Mathematics

The University of Texas at Dallas





Contents

- 
- A vertical bar on the left side of the slide, composed of four segments: a red top segment, a blue middle segment, a red segment, and a blue bottom segment. The bar has a black outline and a slight gradient.
- 
- A horizontal row of 18 orange dots, evenly spaced, located above the main list of contents.
- Description of Frequency Selective Surfaces (FSS)
 - Applications for FSSs
 - Past Research on FSSs
 - Overview of Research on FSSs
 - Justification of this Research
 - Survey of Results
 - Comparison of Model to Measured Data
 - Multiple Apertures per Periodic Cell
 - Outline of Remaining Research



Description of Frequency Selective Surfaces (FSS)

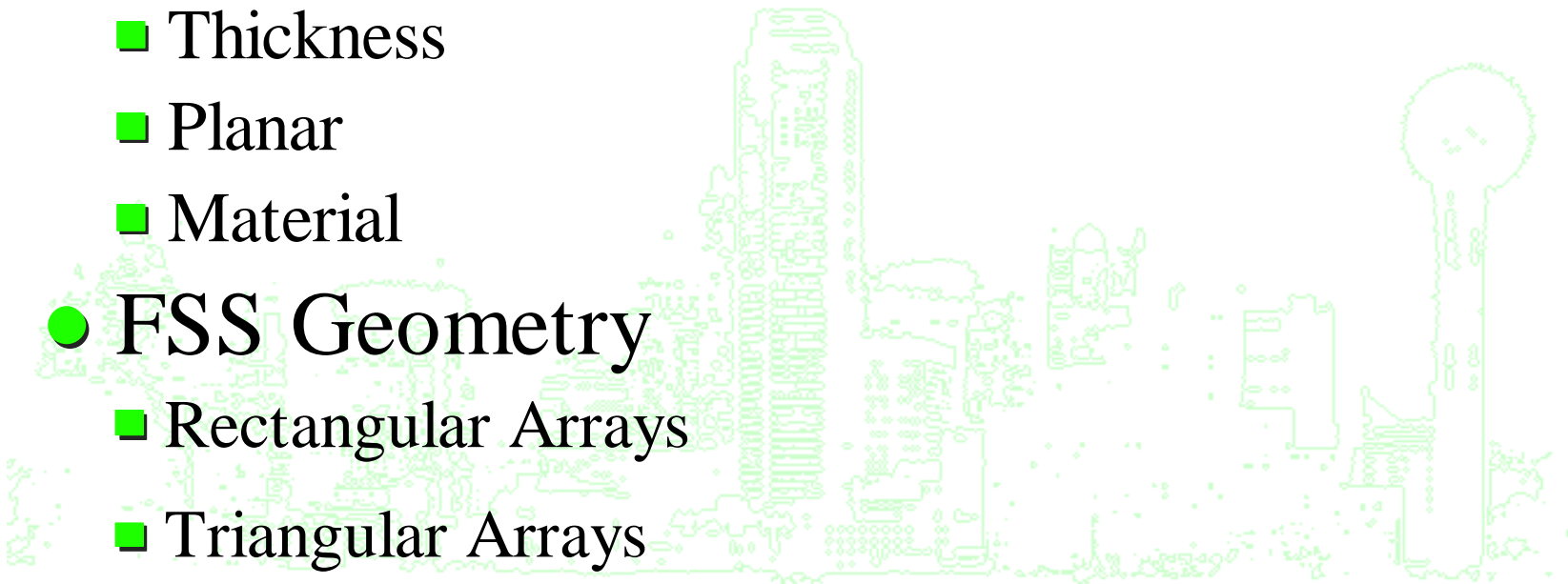
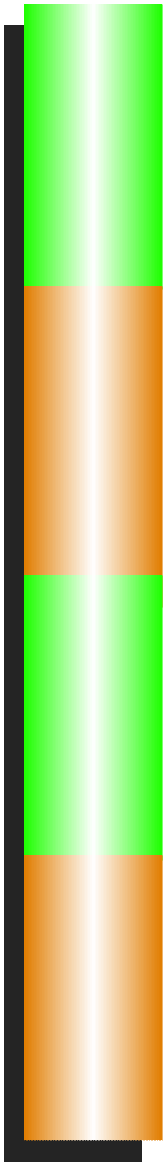
- Physical Description

- Types
- Thickness
- Planar
- Material

- FSS Geometry

- Rectangular Arrays
- Triangular Arrays

- Key Concepts

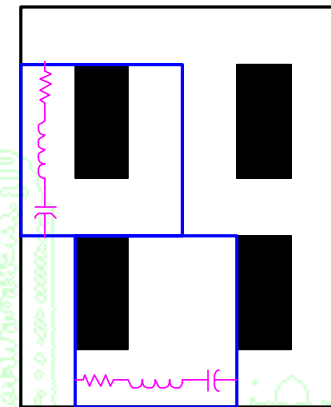


Description of FSSs

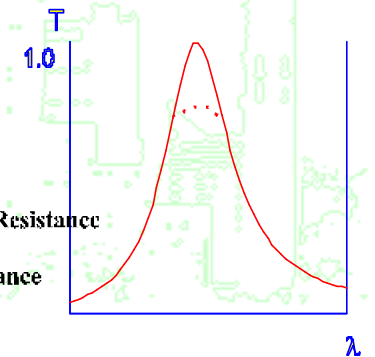
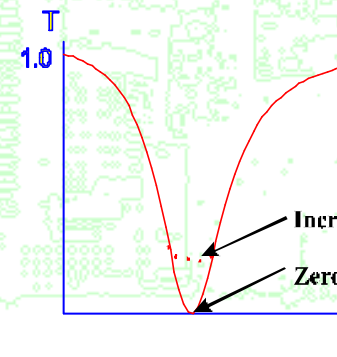
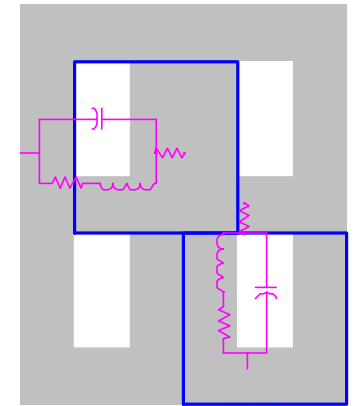
Types of FSSs

- Apertures vs. Patches
 - Capacitive
 - Inductive
 - Resonant Structures
 - Application of Babinet's Principle
- Planar vs. Surface Relief
- Thick vs. Thin
 - Construction Techniques
 - Substrates
- Perfect Conductor vs. Lossy

Capacitive



Inductive

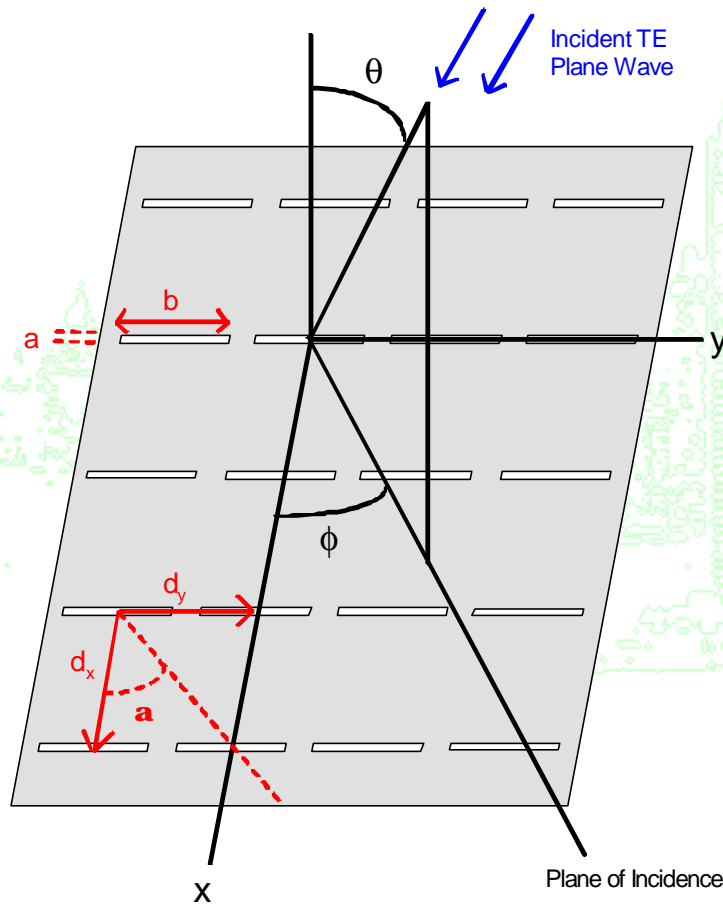


Description of FSSs

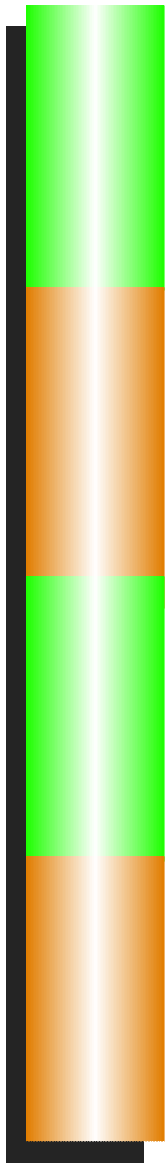
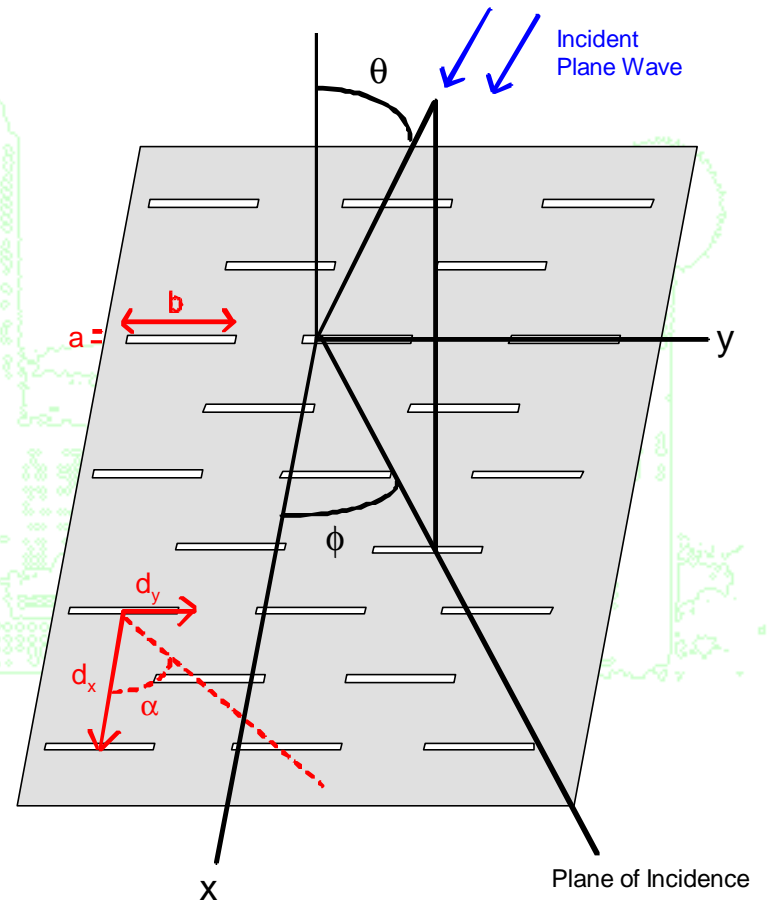
FSS Geometry for Single Aperture/Patch per Periodic Cell



Rectangular Array



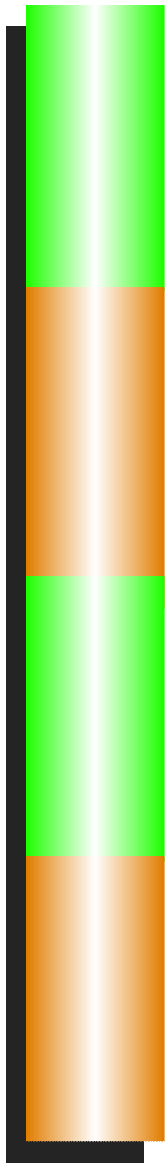
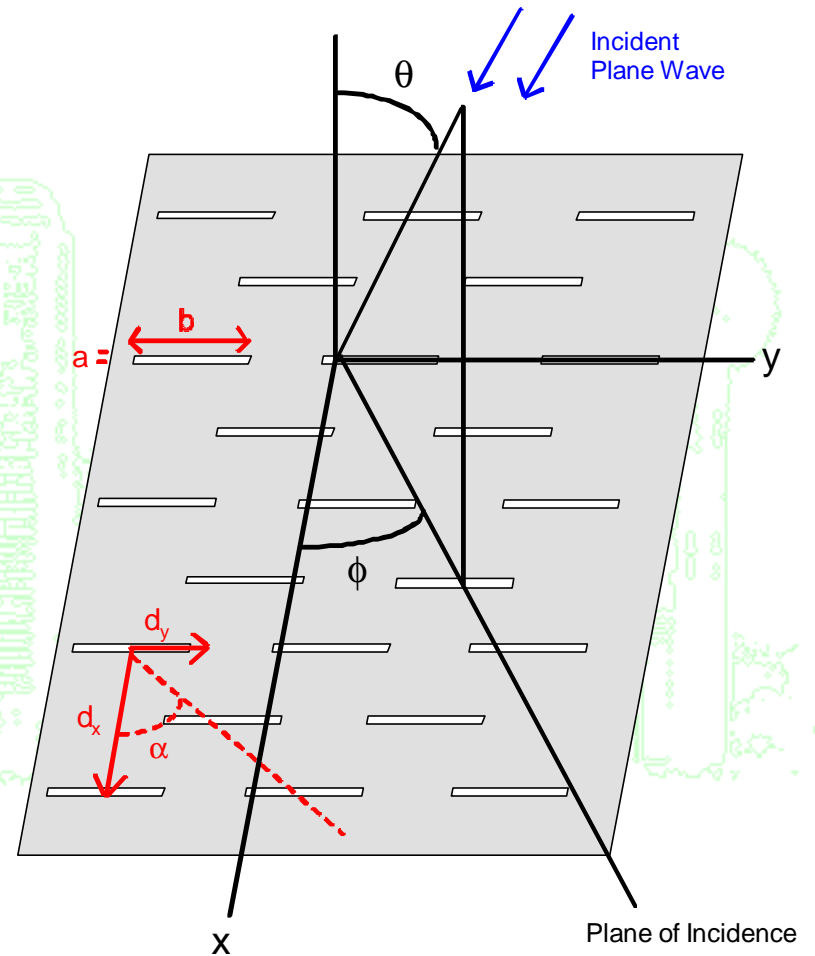
Triangular Array



Description of FSSs

Concepts

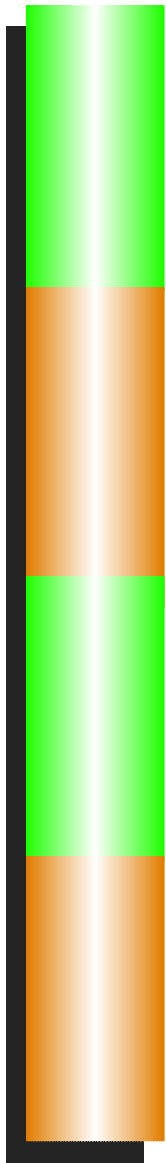
- Periodicity
- Diffraction Edge
- Nearest Neighbor
- Specular (Zeroth) Order Diffraction
- Higher Diffractive Orders and Wood's Anomalies
- Floquet's Theorem





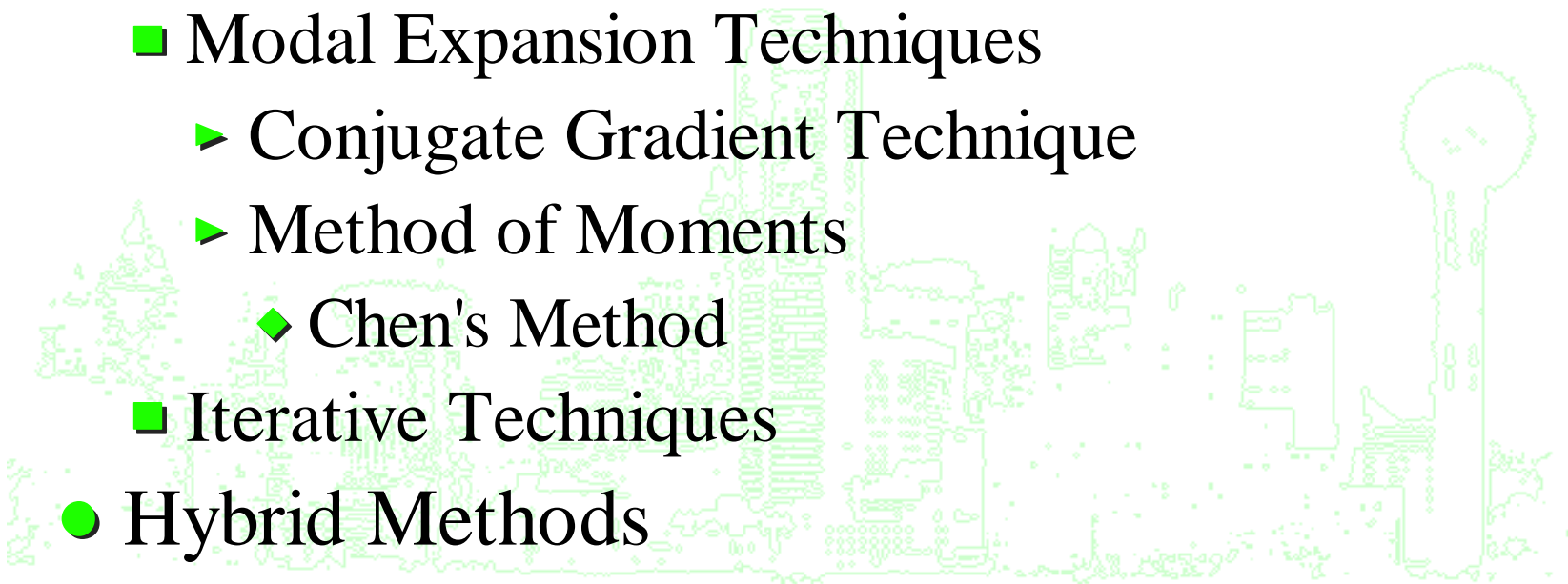
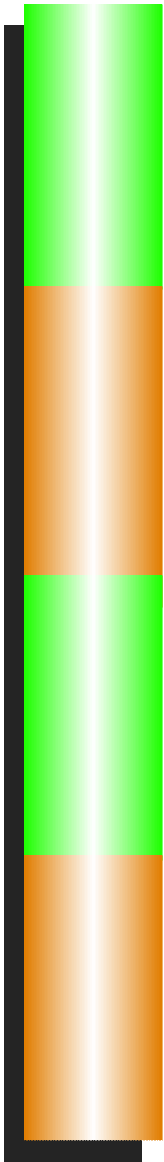
Applications for FSSs

- Polarizers
- Beam Splitters
- Bandpass Filters
- Astronomy Filters
- Filters for Spacecraft Instrumentation



Past Research on FSSs

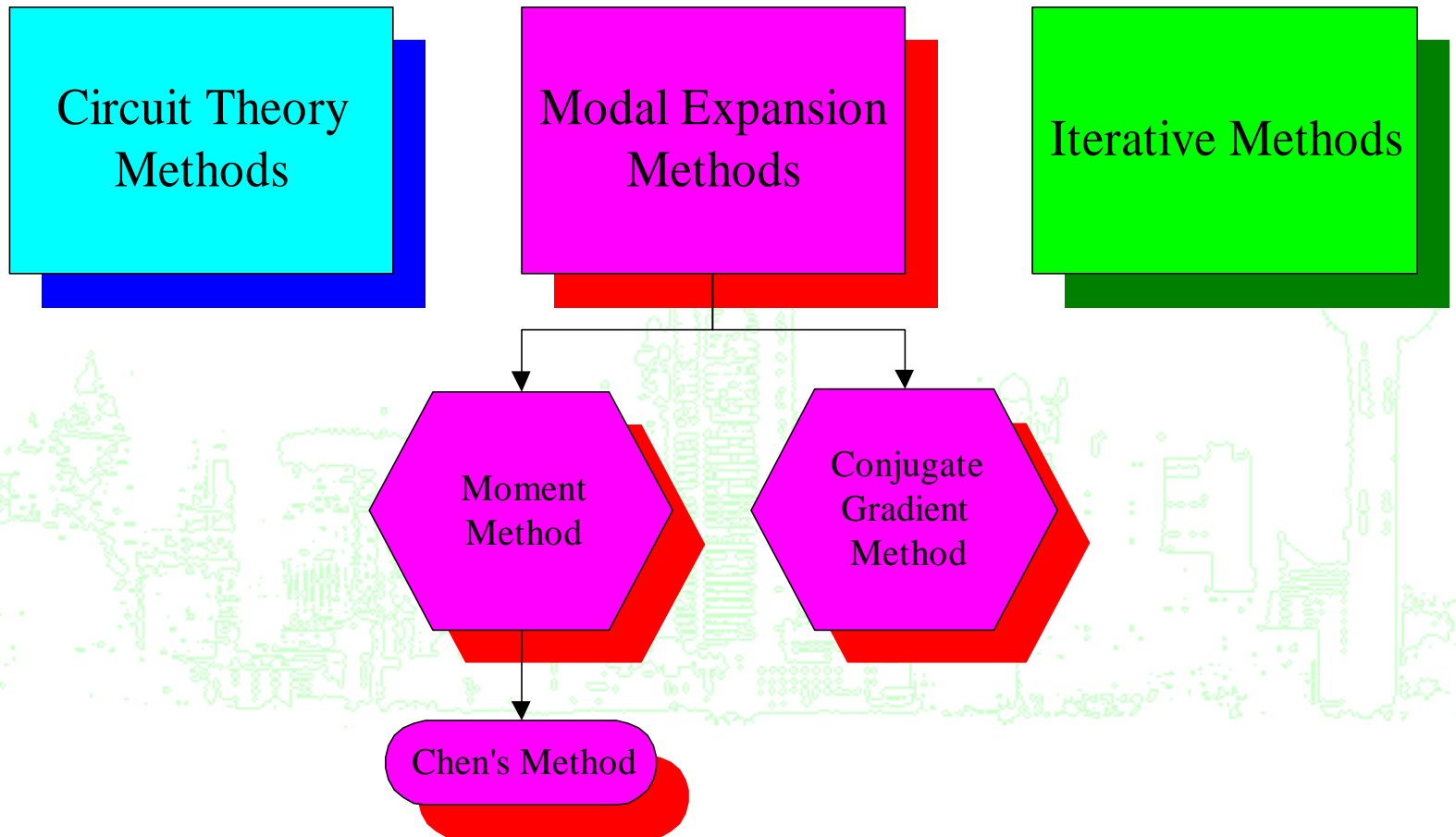
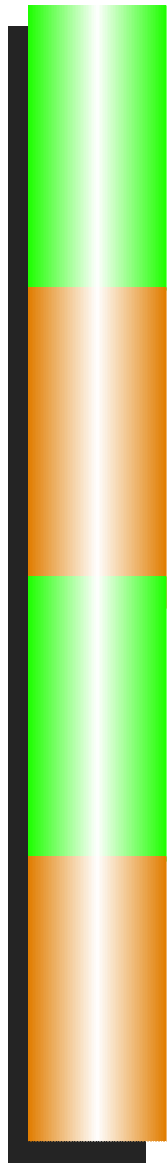
- Methods of Analyzing FSSs
 - Circuit Theory Techniques
 - Modal Expansion Techniques
 - ▶ Conjugate Gradient Technique
 - ▶ Method of Moments
 - ◆ Chen's Method
 - Iterative Techniques
- Hybrid Methods
 - Stacked FSSs
 - Capacitive FSS Superimposed on Inductive FSS





Past Research

Methods of Analyzing FSSs





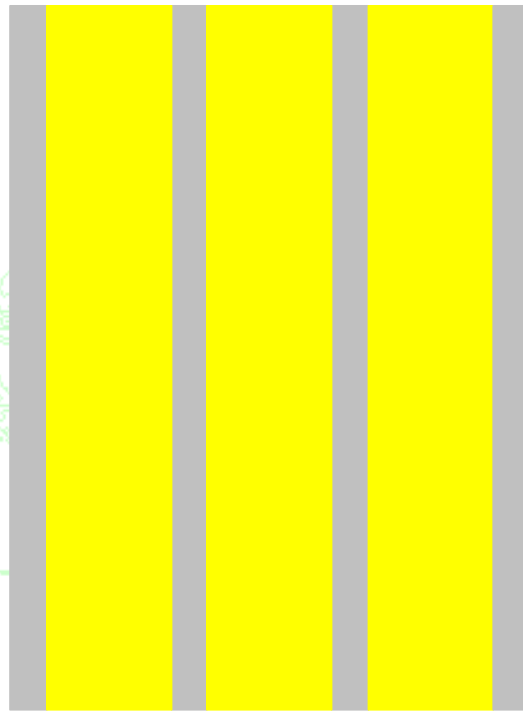
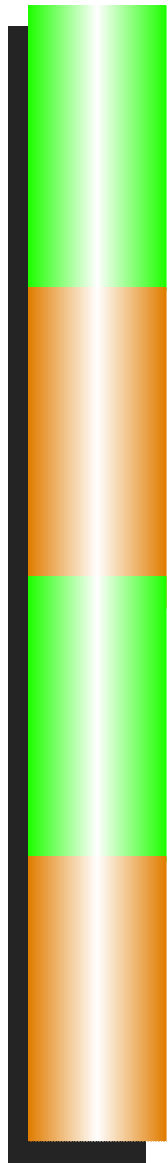
Past Research

Hybrid FSSs



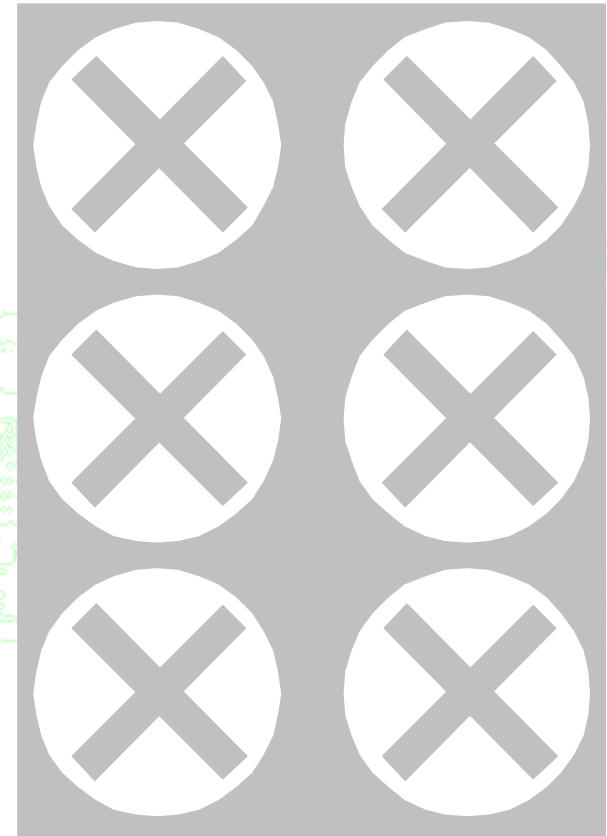
Stacked FSS

Capacitive-Inductive
FSS



↑
FSS

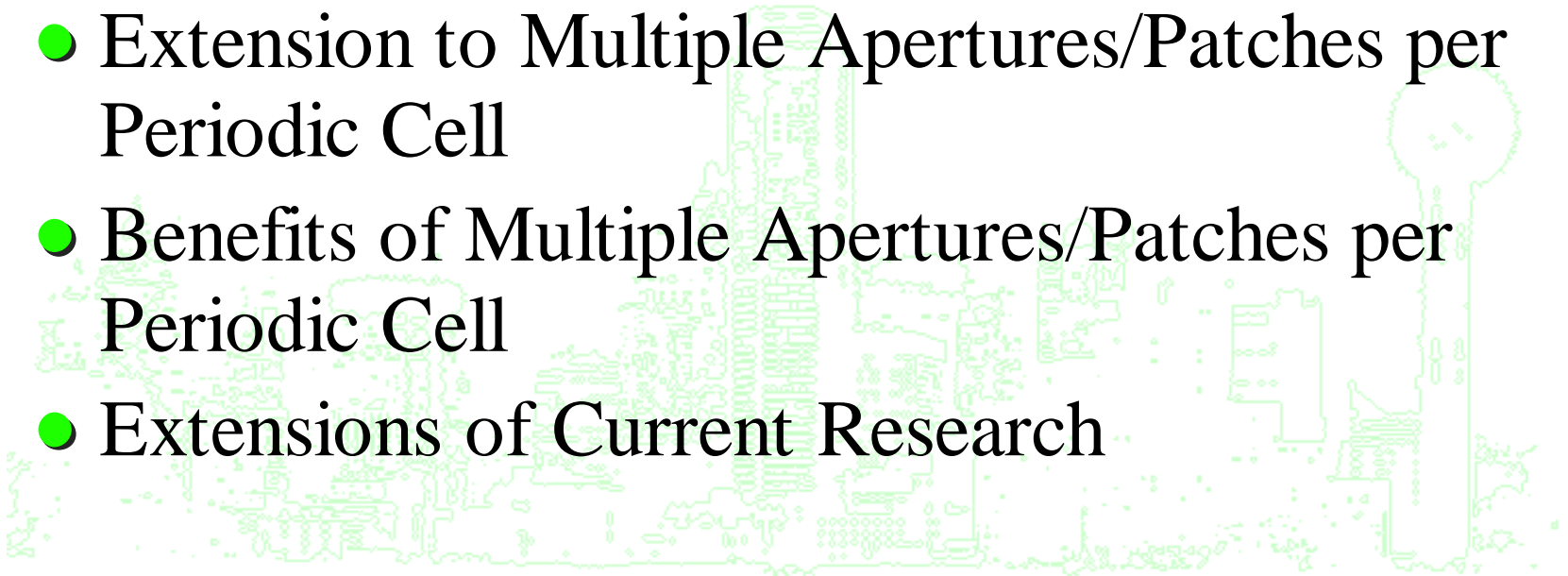
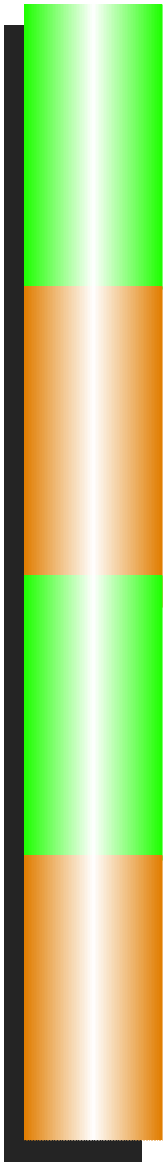
↑
Dielectric





Overview of Research on FSSs

- 
- Modeling Capabilities
 - Modal Method
 - Extension to Multiple Apertures/Patches per Periodic Cell
 - Benefits of Multiple Apertures/Patches per Periodic Cell
 - Extensions of Current Research



Overview of Research

Modeling Capabilities

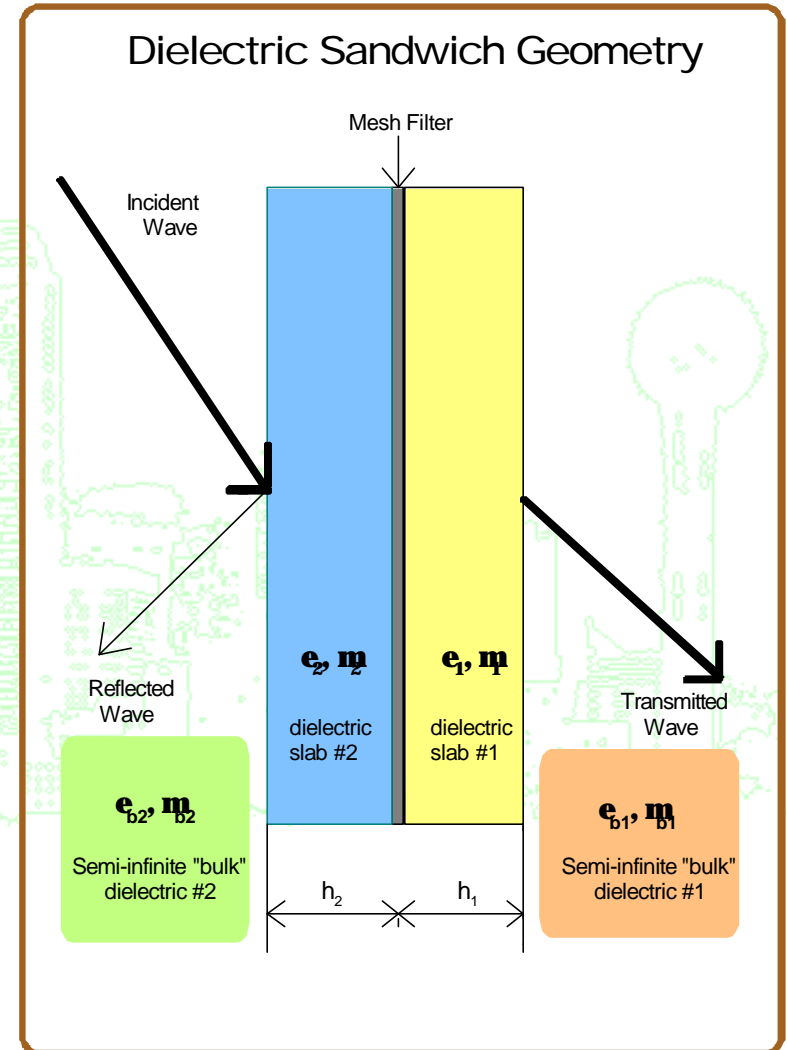
- Substrates provide a physical structure for the sub-micron thick FSS mesh filter
- The theoretical model of the filter must account for properties of substrate
- From transmission line theory the modal admittance looking into the dielectric region is

$$Y_{pqr} = \mathbf{x}_{pqr}^{d_i} \frac{\mathbf{x}_{pqr}^{d_i} + j\mathbf{x}_{pqr}^{d_i} \tan(\mathbf{g}_{pq}^{d_i} h_i)}{\mathbf{x}_{pqr}^{d_i} + j\mathbf{x}_{pqr}^{d_i} \tan(\mathbf{g}_{pq}^{d_i} h_i)}$$

where the pq-th modal admittance in material d_i is given by

$$\mathbf{x}_{pqr}^{d_i} = \left(\frac{\mathbf{g}_{pq}^{d_i}}{k_{d_i}} \right)^{(3-2r)} \sqrt{\frac{\mathbf{e}_i}{\mathbf{m}_i}}$$

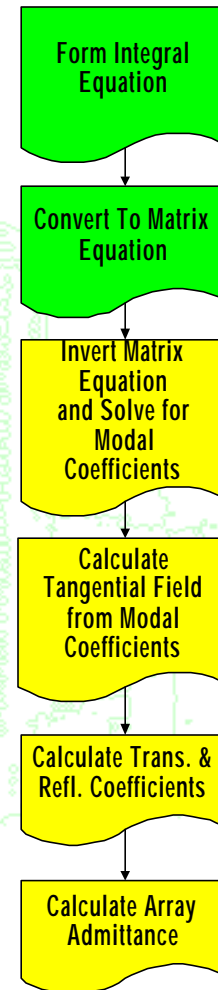
($r=1$ for TE polarization, $r=2$ for TM)



Overview of Research

Modal Method

- Decompose the incident field into zeroth order Floquet modes
- Expand the transmitted & reflected fields as an infinite series of Floquet modes with unknown coefficients
- Match the boundary conditions at the filter
- Substitute the integral representation of the reflection & transmission coefficients into the resulting equation to form an integral equation
- Convert the integral equation into a matrix equation using Galerkin's moment method
- Solve numerically by matrix inversion
- Calculate transmission and reflection coefficients



$$2 \sum_{r=1}^2 A'_{00r} \frac{x_{00r}^{b2} x_{00r}^{d2} \bar{\Phi}_{00r}}{x_{00r}^{d2} \cos(\mathbf{g}_0^{d2} h_2) + j x_{00r}^{b2} \sin(\mathbf{g}_0^{d2} h_2)}$$

$$= \sum_p \sum_q \sum_{r=1}^2 (Y_{pqr}^{d2} + Y_{pqr}^{d1}) \bar{\Phi}_{pqr} \int_{cell} \bar{E}_t \cdot \bar{\Phi}_{pqr}^* da$$

$$[Y_{MNL}] [F_{mnl}] = [I_{mnl}]$$

$$[F_{mnl}] = [Y_{MNL}]^{-1} [I_{mnl}]$$

$$\bar{E}_t = \sum_m \sum_n \sum_{l=1}^2 F_{mnl} \bar{Y}_{mnl}$$

$$R_{pqr} + \mathbf{d}_0 \mathbf{d}_0 A_{pqr} = B_{pqr} = \int_{aperture} \bar{E}_t \cdot \bar{\Phi}_{pqr}^* da$$

$$Y'_r = \left(\frac{1 - R'_{00r}}{1 + R'_{00r}} \right) X_{00r}^{d2}$$

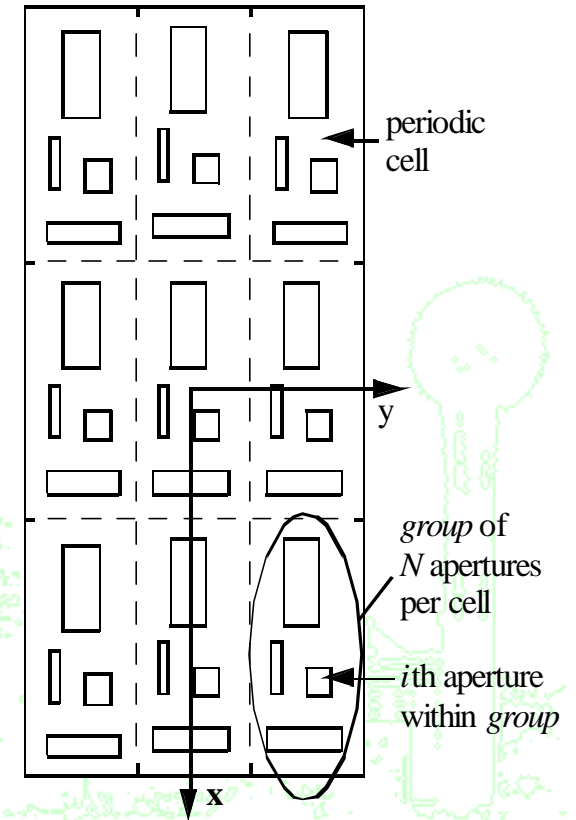
Overview of Research

Extension to Multiple Apertures/Patches per Periodic Cell

- Consider a mesh with apertures.
 - The filter is modeled as a perfect conductor.
 - The transverse field at the plane of the filter is within the apertures only.
 - For an "unit cell" of N apertures, the transverse field contribution at the plane of the filter is:

$$\vec{E}_t = \sum_{i=1}^N \vec{E}_t^{(i)}$$

- This value can then be substituted back into the modal method integral equation.
- For a mesh with patches, the *sum* of the induced currents on each patch within the "unit cell" is substituted into the appropriate integral equation.



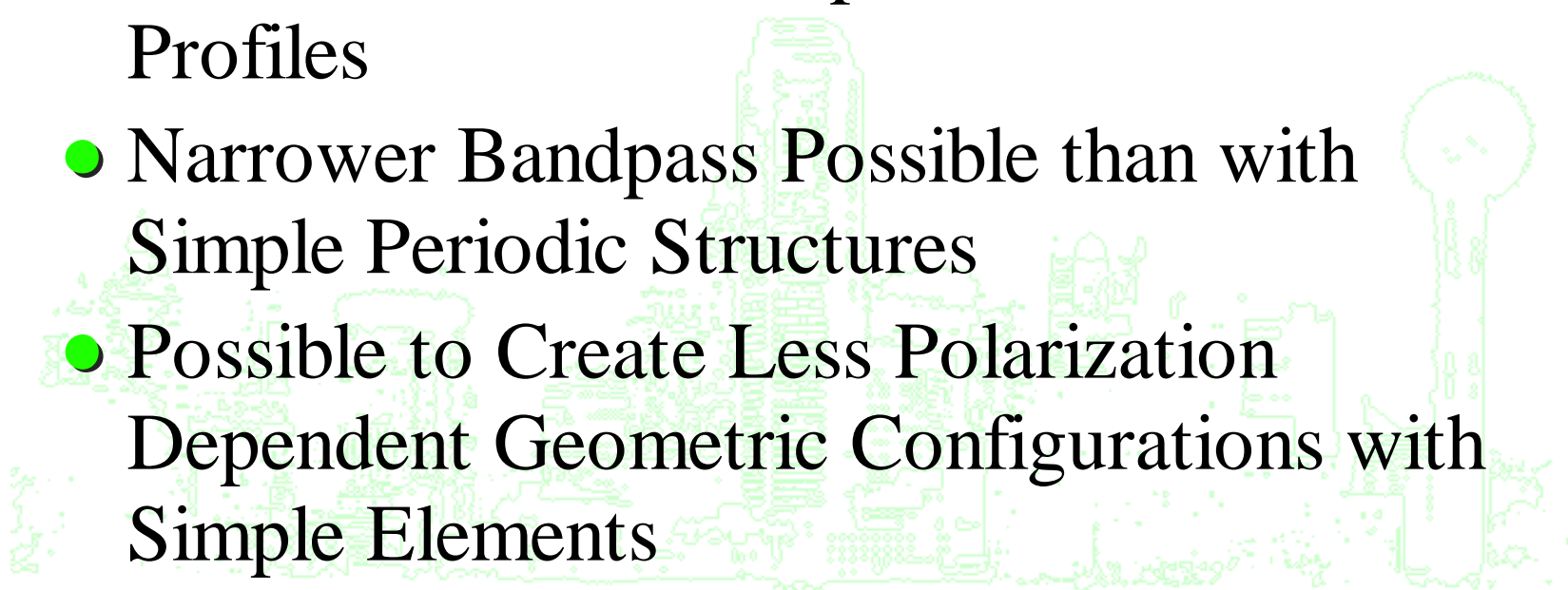
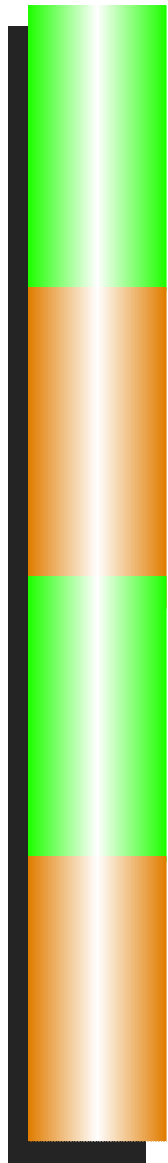


Overview of Research

Benefits of Multiple Apertures/Patches per Periodic Cell



- Easier to Construct than "stacked FSSs"
- Dual Resonance Bandpass Transmission Profiles
- Narrower Bandpass Possible than with Simple Periodic Structures
- Possible to Create Less Polarization Dependent Geometric Configurations with Simple Elements



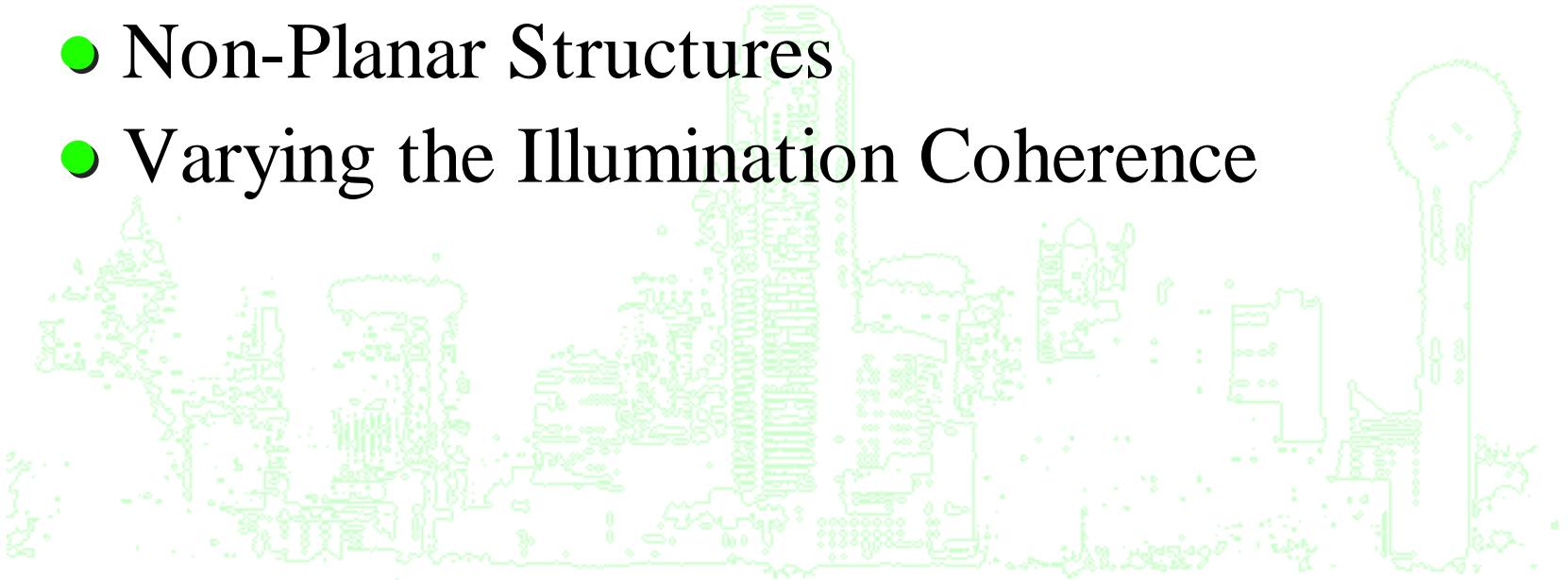
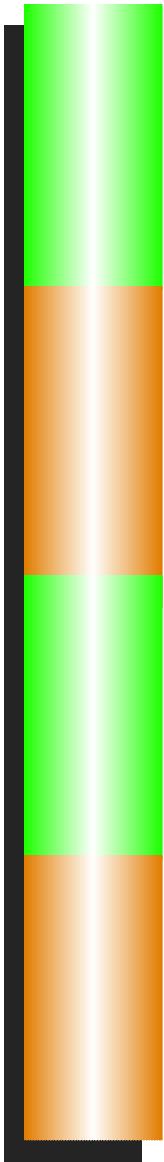


Overview of Research

Extensions of Current Research



- Multiply Periodic Arrays
- Non-Perfect Conductors
- Non-Planar Structures
- Varying the Illumination Coherence



Justification of this Research

- No Extensive Analysis on Relationship Between Periodicity, Periodic Element Geometry, and the Spectral Profile Exists
- Constructing FSSs with the Multiple Aperture/Patch per Periodic Cell Approach Has Not Been Thoroughly Investigated
- Examination of the Effects of Wood's Anomalies on the Spectral Profiles of FSSs is Incomplete

Survey of Results



- Comparing Calculated Results to Measured Data

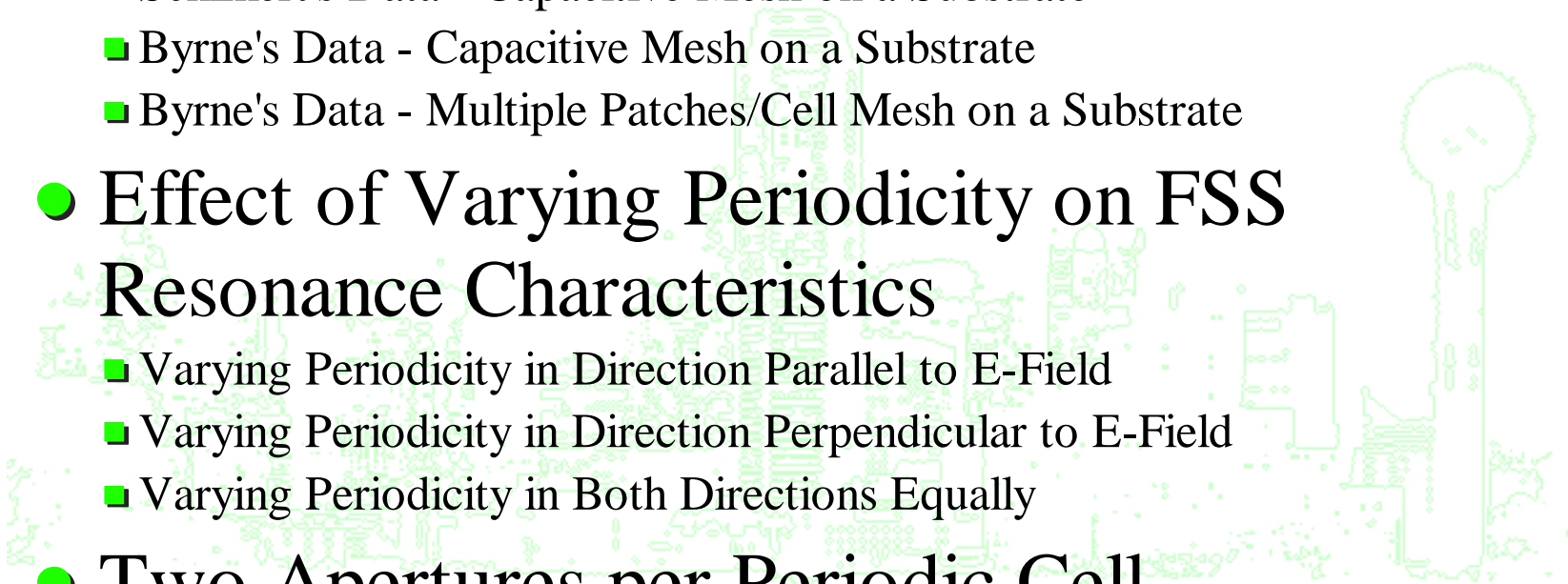
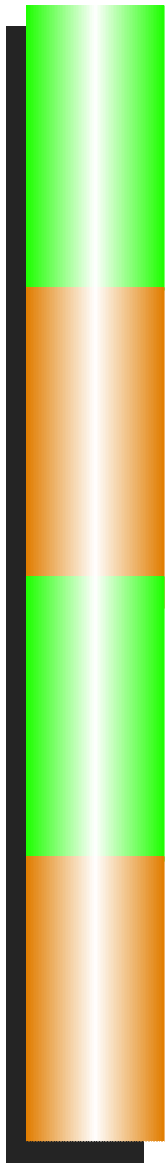
- Schimert's Data - Capacitive Mesh on a Substrate
- Byrne's Data - Capacitive Mesh on a Substrate
- Byrne's Data - Multiple Patches/Cell Mesh on a Substrate

- Effect of Varying Periodicity on FSS Resonance Characteristics

- Varying Periodicity in Direction Parallel to E-Field
- Varying Periodicity in Direction Perpendicular to E-Field
- Varying Periodicity in Both Directions Equally

- Two Apertures per Periodic Cell

- Varying Lengths of Alternating Columns of Apertures
- Varying Lengths of Alternating Rows of Apertures
- Varying Lengths of Alternating Apertures

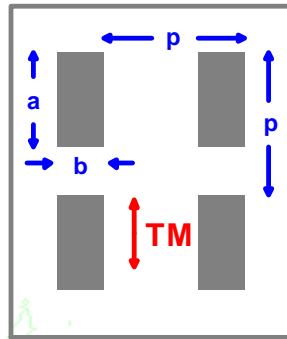




Comparing Calculated Results to Measured Data

Schimert's Data - Capacitive Mesh on a Substrate

Capacitive Mesh:



Properties

$n_1 = 1$, $n_2 = 2.2$ (ZnS)

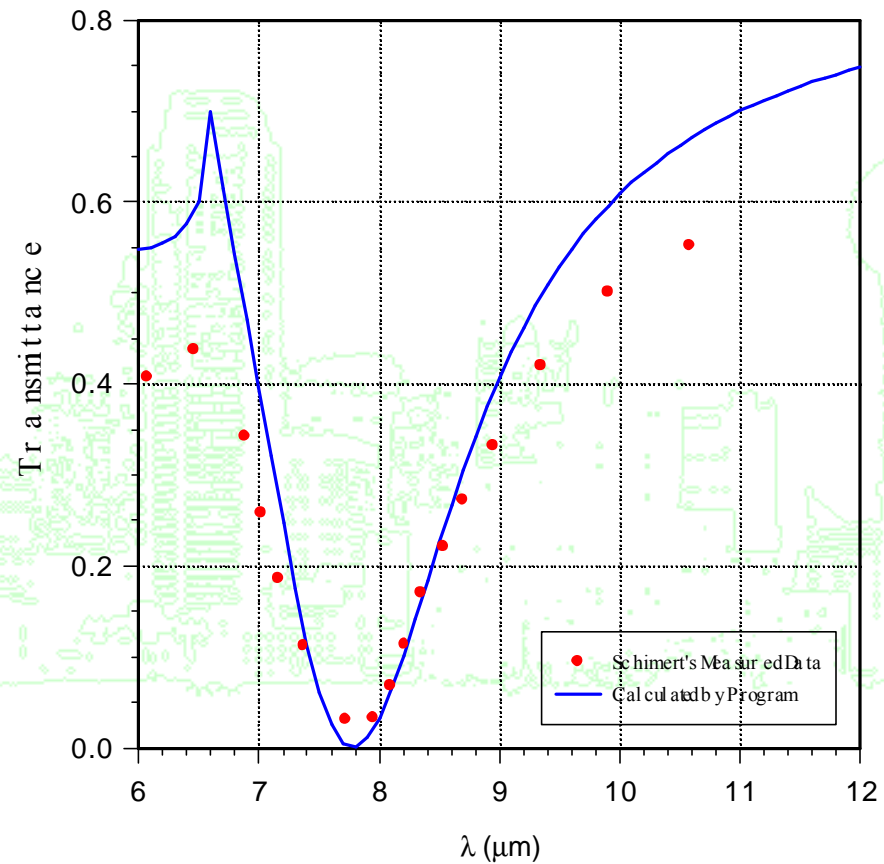
$a = 2.1 \mu\text{m}$

$b = 0.8 \mu\text{m}$

$p = 3.0 \mu\text{m}$

(Schimert, T., Koch, M., and Chan, C, *J. Opt. Soc. Am. A*, **7**, August 1990, 1545-1553)

Schimert's Data

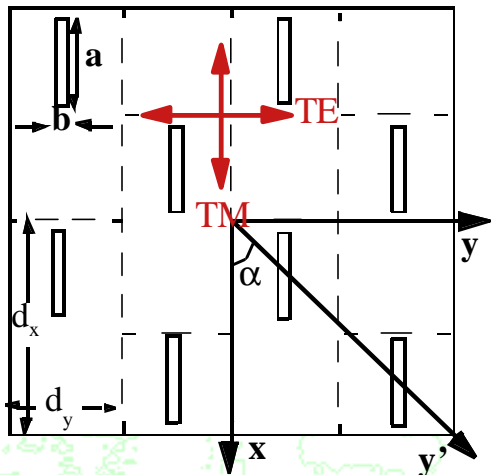




Comparing Calculated Results to Measured Data

Byrne's Data - Capacitive Mesh on a Substrate

Filter Geometry



Properties

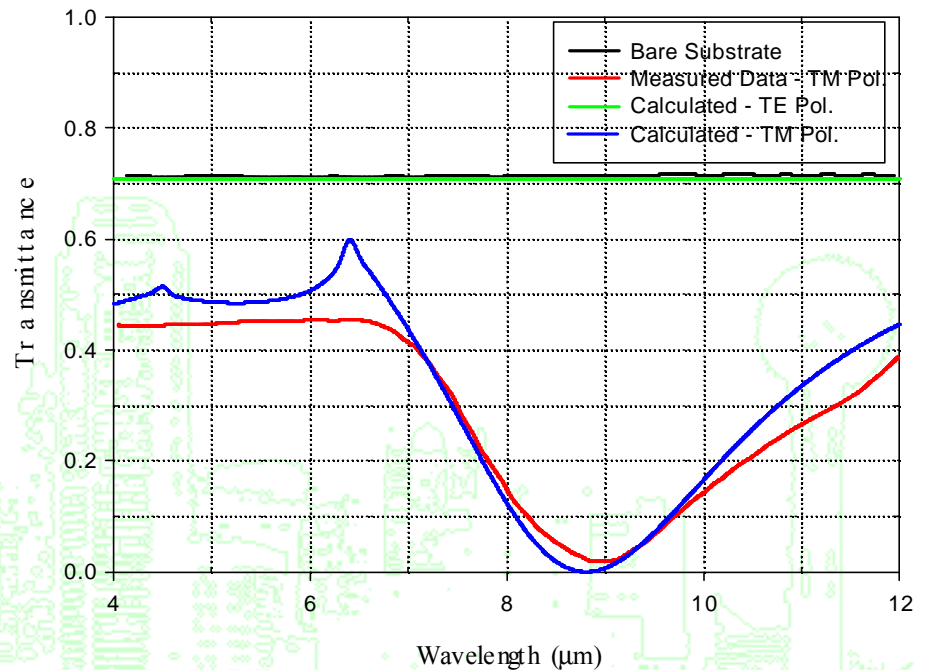
$n_1 = 1$, $n_2 = 2.4$ (ZnSe)

triangular array, $\alpha = 45$ deg.

$d_x = 3.75 \mu\text{m}$ $d_y = 1.875 \mu\text{m}$

$a = 2.5 \mu\text{m}$ $b = 0.25 \mu\text{m}$

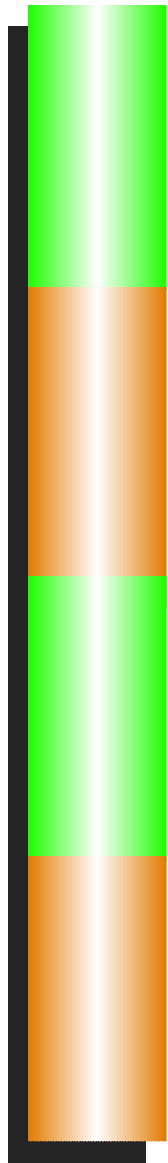
(Byrne, Dale M., *Proceedings of SPIE*, **560**,
August 1985, p. 70-79)



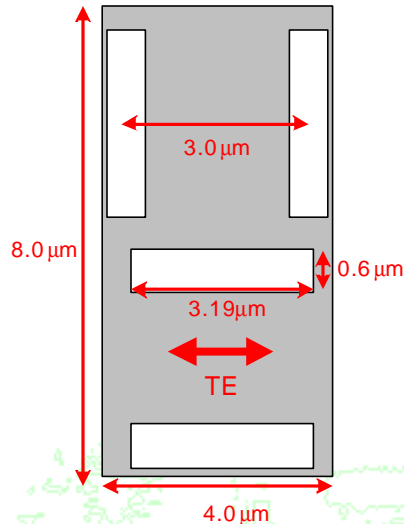


Comparing Calculated Results to Measured Data

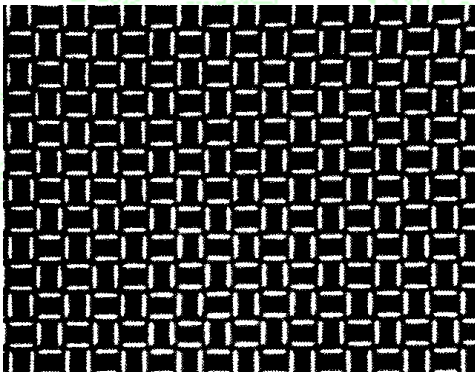
Byrne's Data - Multiple Patches/Cell Mesh on a Substrate



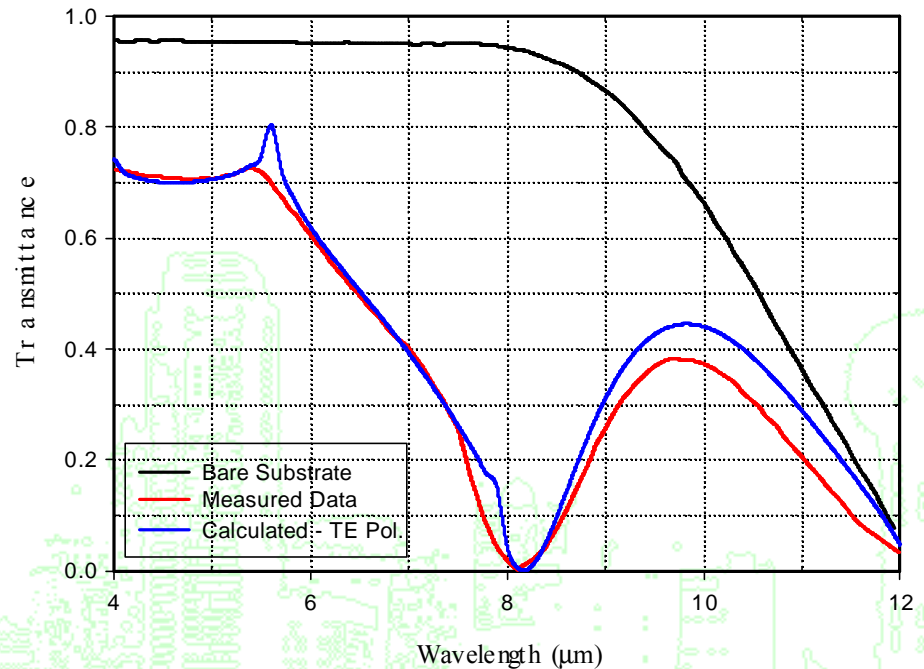
Unit Cell Geometry



Optical Microscope Photograph



(Byrne, Dale M., *Proceedings of SPIE*, 560, August 1985, p. 70-79)



Properties

$n_1 = 1, n_2 = 1.4$ (CaF)

triangular array, $\alpha = 45$ deg.

$d_x = 8.0 \mu\text{m}$ $d_y = 4.0 \mu\text{m}$

$a_1 = a_2 = 3.19 \mu\text{m}$ $b_1 = b_2 = 0.6 \mu\text{m}$

$a_3 = a_4 = 0.6 \mu\text{m}$ $b_3 = b_4 = 3.19 \mu\text{m}$

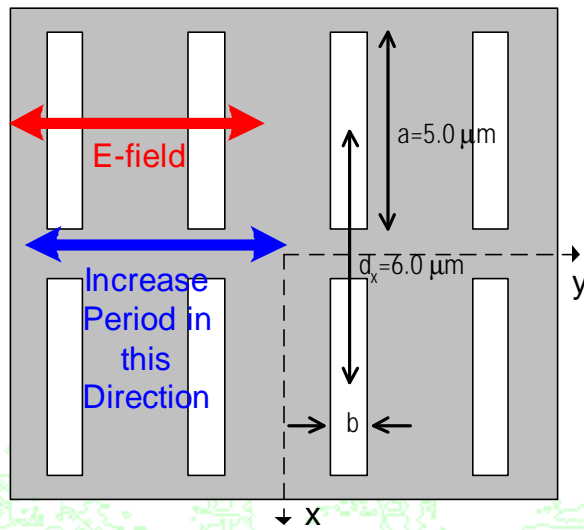
elements spaced $3.0 \mu\text{m}$ apart within cell



Effect of Varying Periodicity on FSS Resonance Characteristics

Varying Periodicity in Direction Parallel to E-Field

Filter Geometry



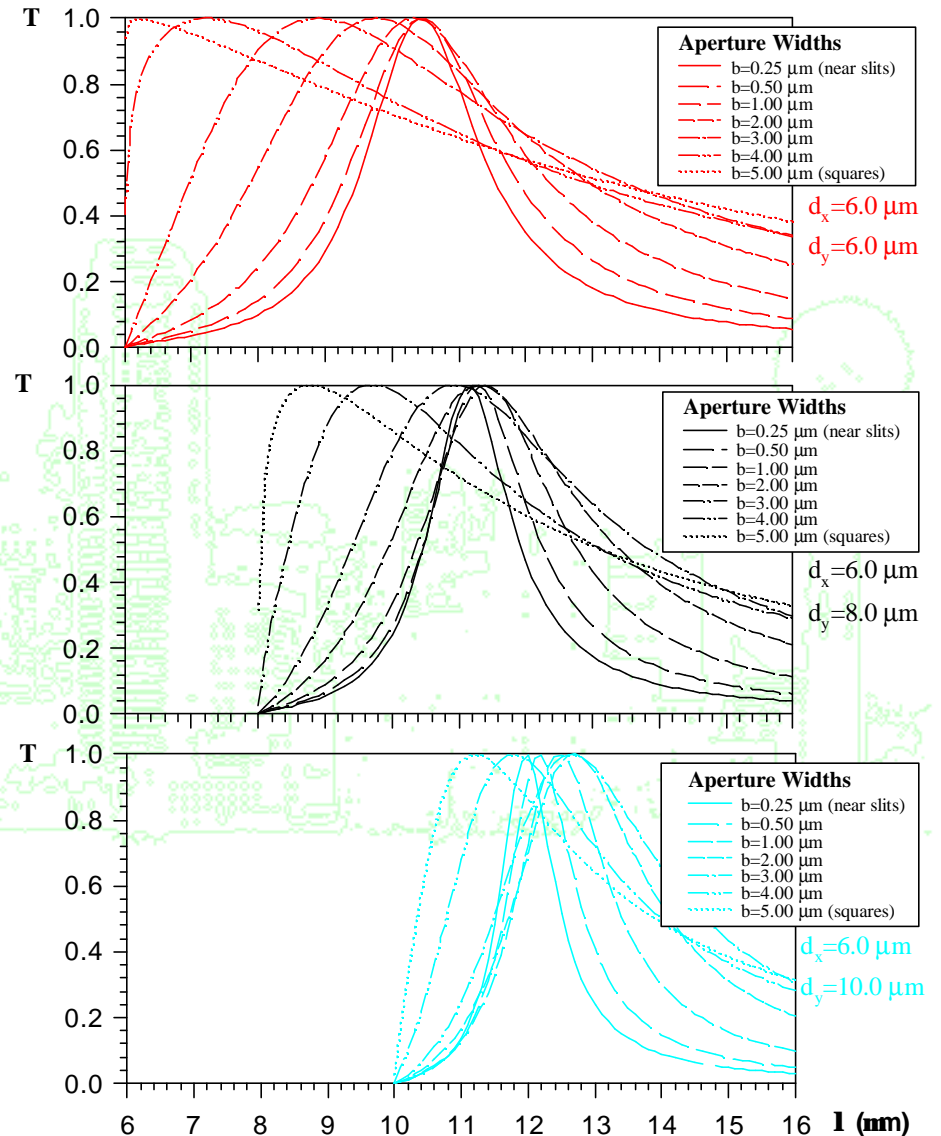
Properties

no substates

rectangular array

$a = 5.0 \mu\text{m}$ $b = \text{variable}$

$d_x = 6.0 \mu\text{m}$ $d_y = \text{variable}$

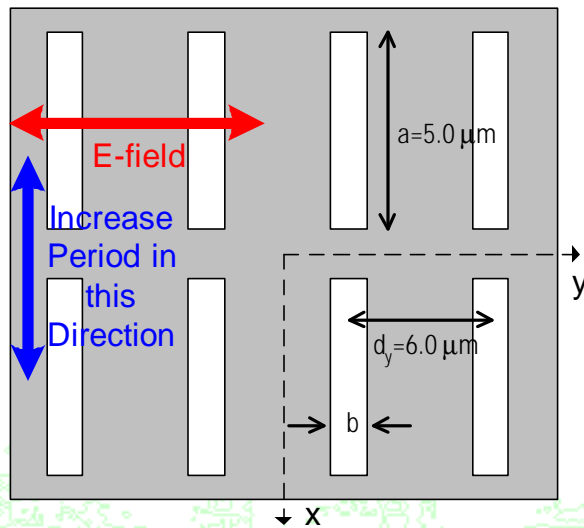




Effect of Varying Periodicity on FSS Resonance Characteristics

Varying Periodicity in Direction Perpendicular to E-Field

Filter Geometry



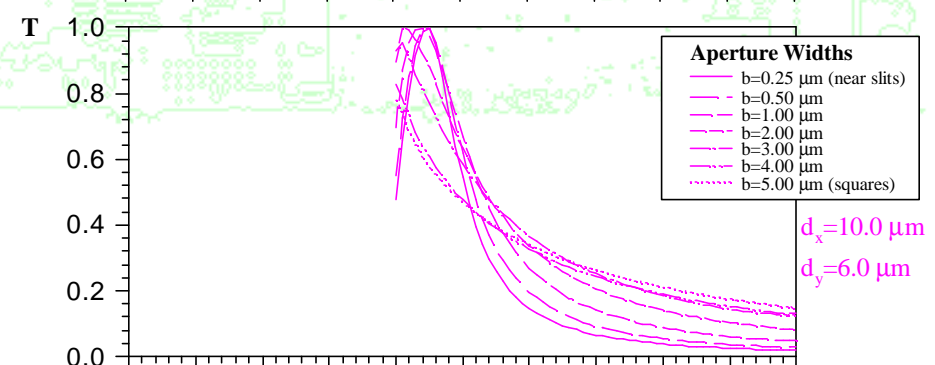
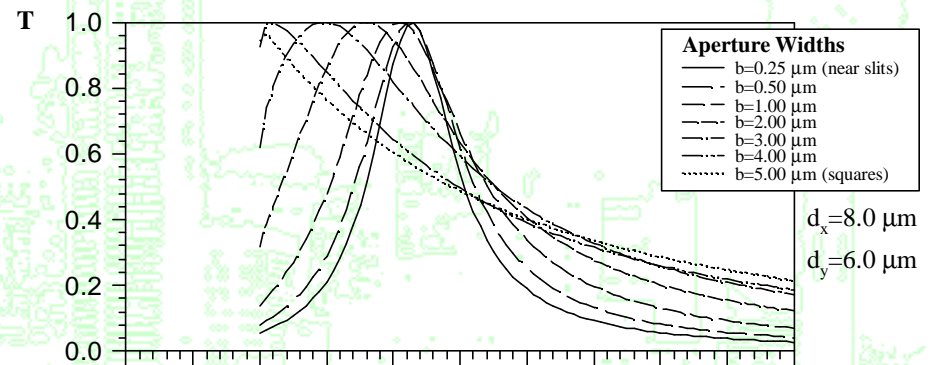
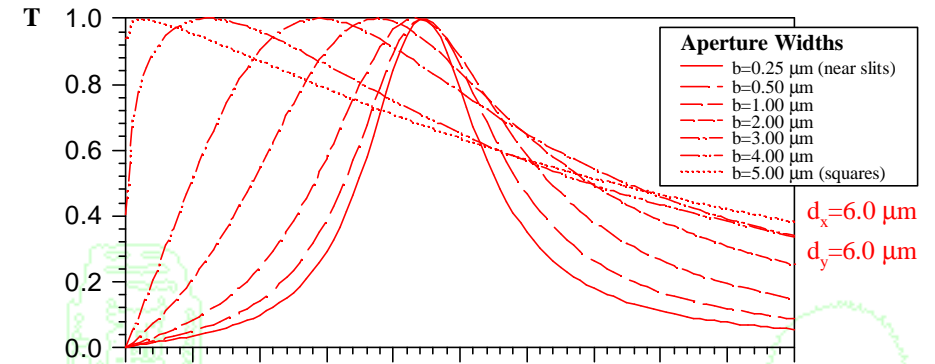
Properties

no substates

rectangular array

$a = 5.0 \mu\text{m}$ $b = \text{variable}$

$d_x = \text{variable}$ $d_y = 6.0 \mu\text{m}$



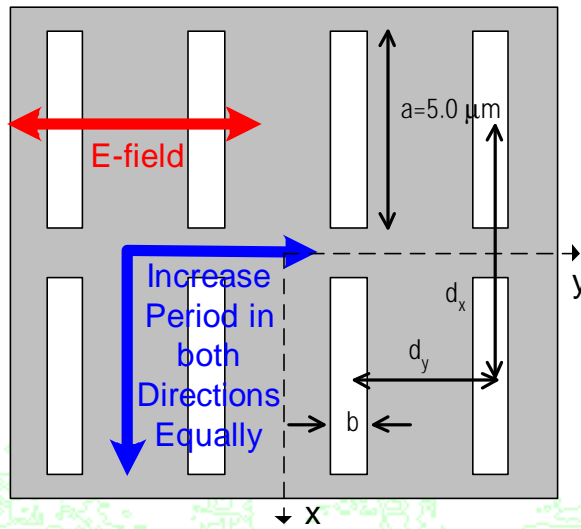
6 7 8 9 10 11 12 13 14 15 16 l (nm)



Effect of Varying Periodicity on FSS Resonance Characteristics

Varying Periodicity in Both Directions Equally

Filter Geometry



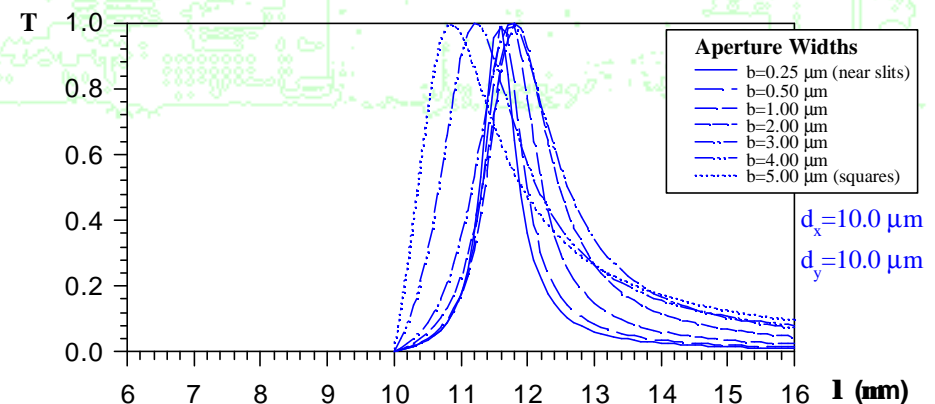
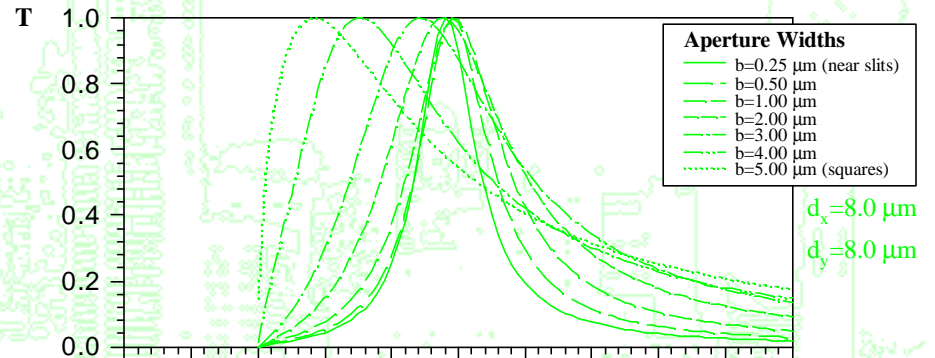
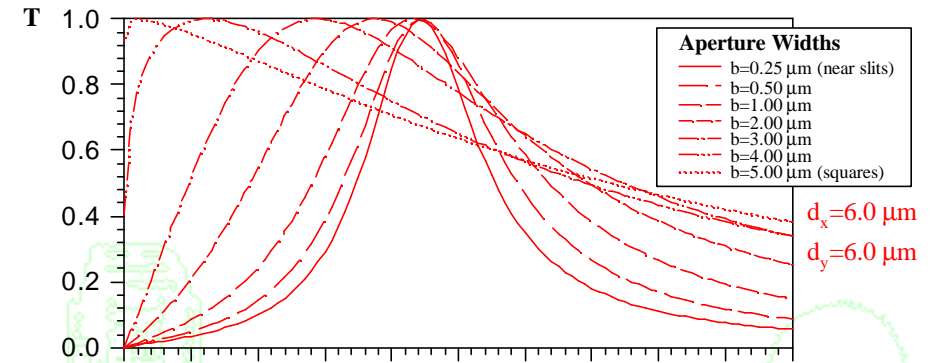
Properties

no substates

rectangular array

$a = 5.0 \mu\text{m}$ $b = \text{variable}$

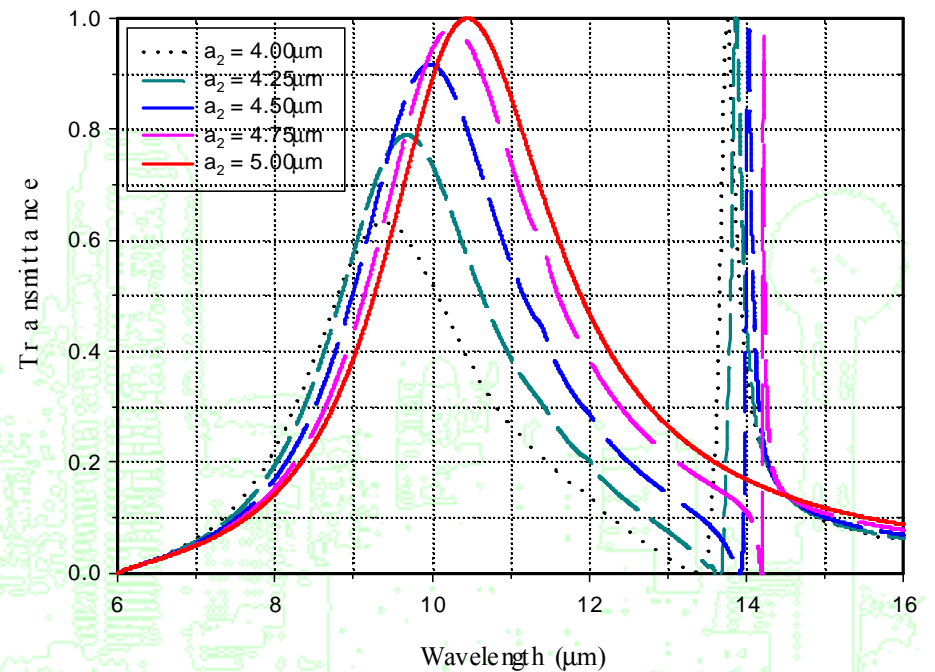
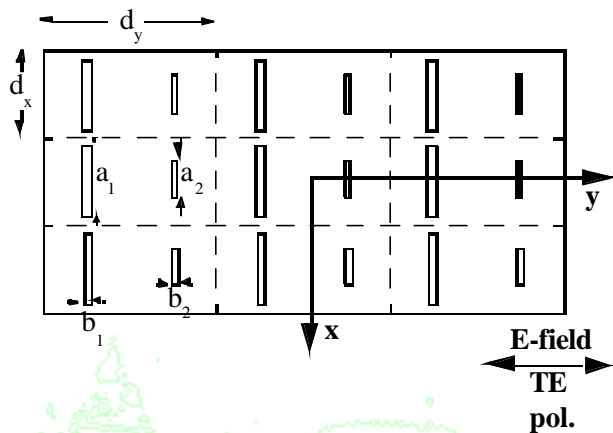
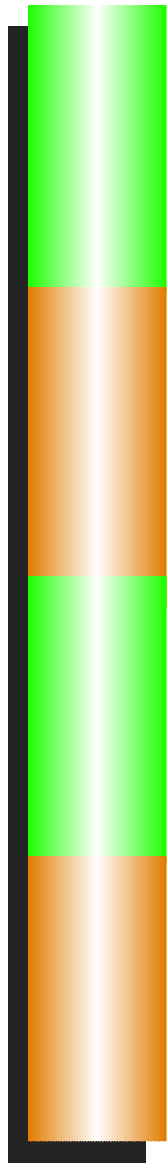
$d_x = d_y = \text{variable}$





Two Apertures per Periodic Cell

Varying Lengths of Alternating Columns of Apertures



Properties

no substrate
rectangular array

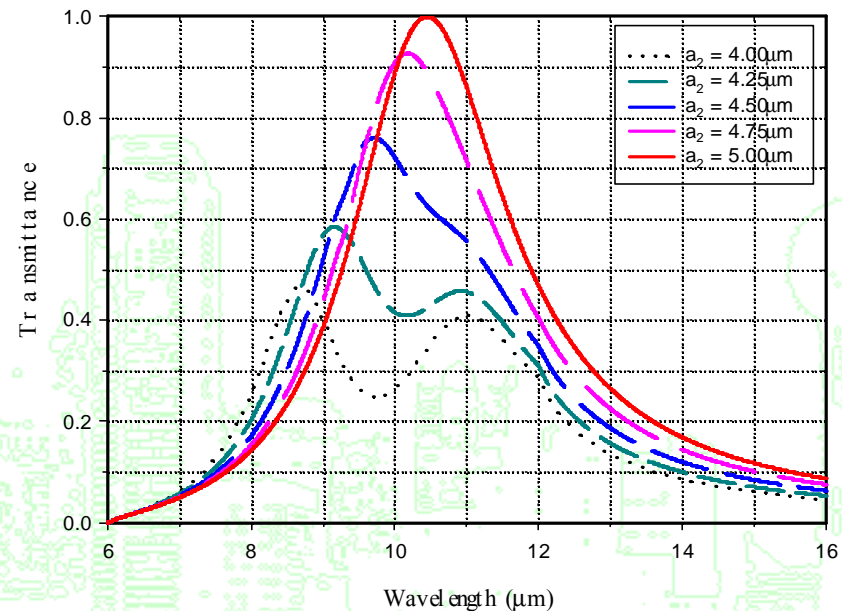
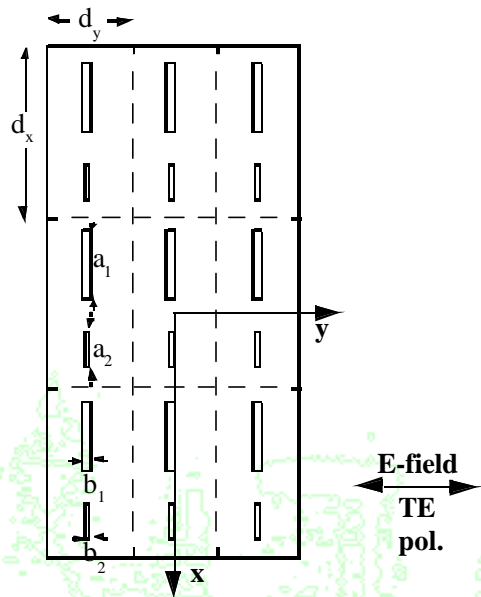
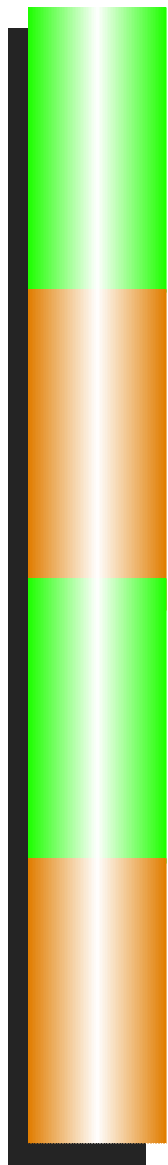
$$d_x = 6.0 \mu\text{m} \quad d_y = 12.0 \mu\text{m}$$

$$a_1 = 5.0 \mu\text{m} \quad b_1 = 0.5 \mu\text{m}$$

$$a_2 = \text{variable} \quad b_2 = 0.5 \mu\text{m}$$

Two Apertures per Periodic Cell

Varying Lengths of Alternating Rows of Apertures



Properties

no substrate

rectangular array

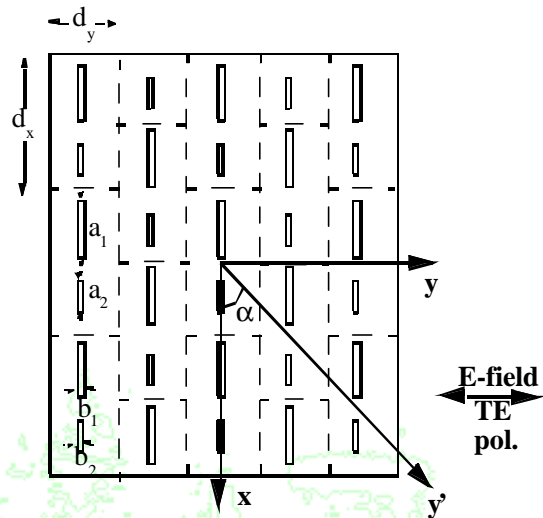
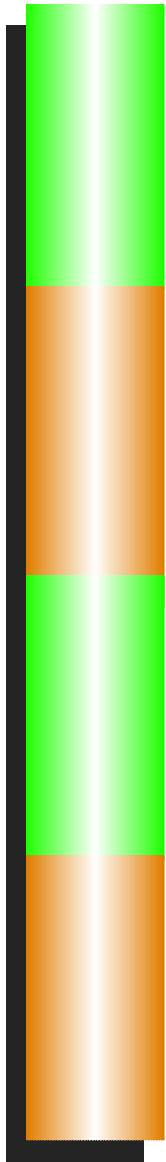
$d_x = 12.0 \mu\text{m}$ $d_y = 6.0 \mu\text{m}$

$a_1 = 5.0 \mu\text{m}$ $b_1 = 0.5 \mu\text{m}$

$a_2 = \text{variable}$ $b_2 = 0.5 \mu\text{m}$

Two Apertures per Periodic Cell

Varying Lengths of Alternating Apertures



Properties

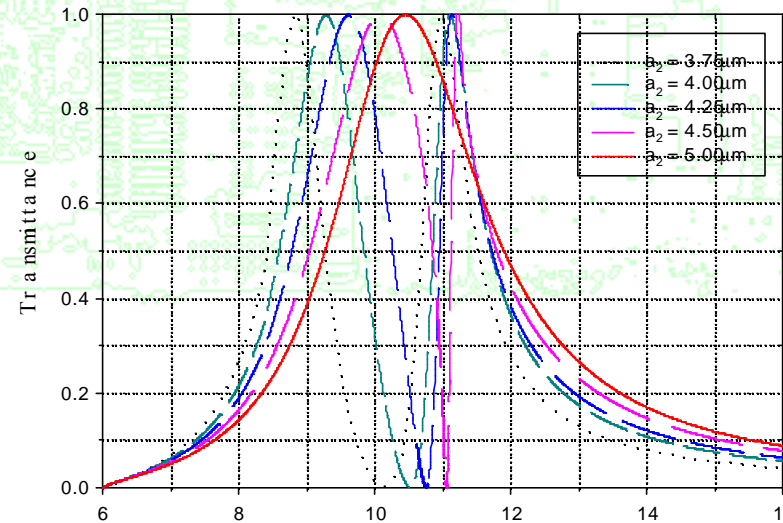
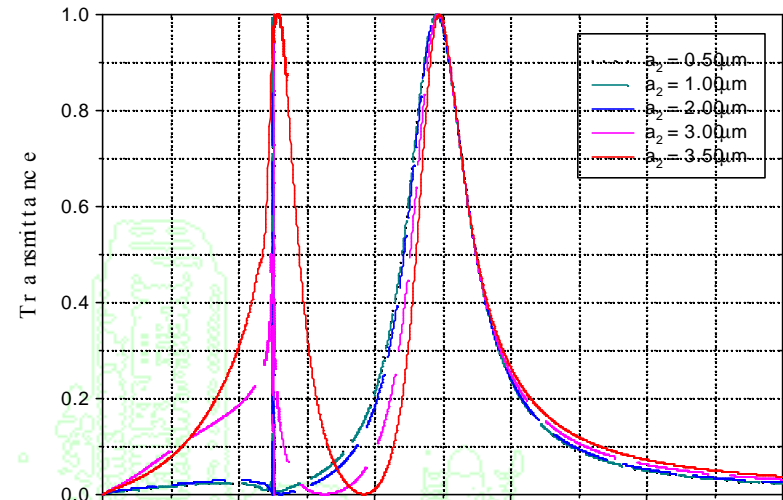
no substrate

triangular array, $\alpha = 45$ deg.

$d_x = 12.0 \mu\text{m}$ $d_y = 6.0 \mu\text{m}$

$a_1 = 5.0 \mu\text{m}$ $b_1 = 0.5 \mu\text{m}$

$a_2 = \text{variable}$ $b_2 = 0.5 \mu\text{m}$

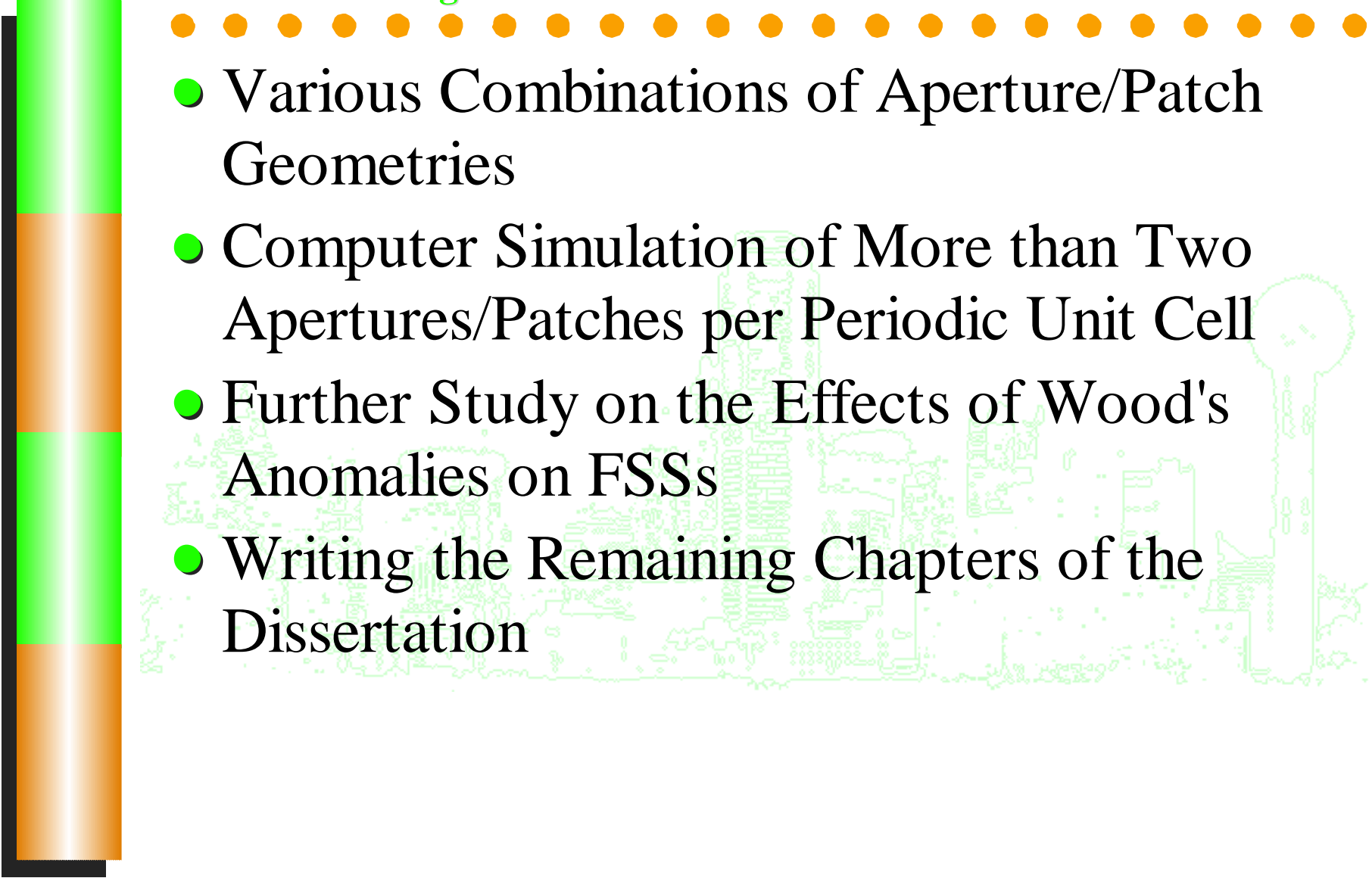


Wavelength (μm)



Results

Remaining Research

- 
- A vertical bar on the left side of the slide is divided into four segments: a green top segment, an orange second segment, a green third segment, and an orange bottom segment. A horizontal dotted line of orange dots runs across the slide, positioned above the list of remaining research items.
- Various Combinations of Aperture/Patch Geometries
 - Computer Simulation of More than Two Apertures/Patches per Periodic Unit Cell
 - Further Study on the Effects of Wood's Anomalies on FSSs
 - Writing the Remaining Chapters of the Dissertation